PROPOSAL for a Forward Silicon Vertex Tracker (FVTX) for the PHENIX Experiment

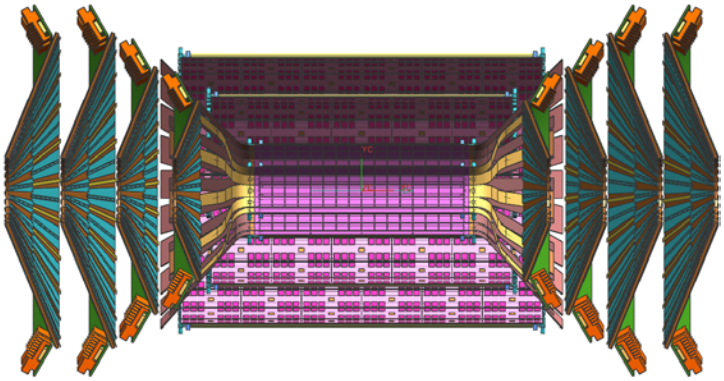

Brookhaven National Laboratory

Relativistic Heavy Ion Collider

March, 2006

Spokesperson:	William A. Zajc, *Columbia University*
Deputy Spokesperson:	Yasuyuki Akiba, *RIKEN*
Deputy Spokesperson:	Matthias Grosse-Perdekamp, *University of Illinois, Urbana-Champaign*
Operations Manager:	Edward J. O'Brien, *Brookhaven National Laboratory*
Upgrades Manager:	Axel Drees, *Stony Brook University*

PHENIX

Proposal for a Forward Silicon Vertex Tracker (FVTX) for the PHENIX Experiment

R. Pak
Brookhaven National Laboratory, Chemistry Dept., Upton NY USA

K.A. Drees
Brookhaven National Laboratory, Collider Accelerator Dept., Upton NY USA

M. Finger, M. Finger
Charles University, Prague, Czech Republic

J. Klaus
Czech Technical University, Prague, Czech Republic

P. Mikes, J. Popule, L. Tomasek, M. Tomasek, V. Vrba
Institute of Physics, Academy of Sciences, Prague, Czech Republic

B. Cole, E. Mannel, D. Winter, W. Zajc
Columbia University, NewYork, NY

J.C. Hill, J.G. Lajoie, C.A. Ogilvie, A. Lebedev, H. Pei, G.Skank,
A. Semenov, G. Sleege, F. Wei
Iowa State University, Ames, IA 56011, USA

N. Saito, M. Togawa, M. Wagner
Kyoto University, Kyoto 606, Japan

J.G. Boissevain, M.L. Brooks, S. Butsyk, C. M. Camacho, G. Grim, H.W. van Hecke, J. Kapustinsky, A. Klein, G.J. Kunde, D.M. Lee, M.J. Leitch, M.X. Liu, P.L. McGaughey, A.K. Purwar, W.E. Sondheim
Los Alamos National Laboratory, Los Alamos, NM 87545, USA

Hisham Albataineh, G. Kyle, H. Liu, S. Pate, X.R. Wang
New Mexico State University, Las Cruces, NM, USA

B. Bassalleck, D.E. Fields, M. Hoeferkamp, M. Malik, J. Turner
University of New Mexico, Albuquerque, NM, USA

Other Interested Institutions:

O. Drapier, A. Debrain, F. Gastaldi, M. Gonin, R. Cassagnac de Granier, F. Flueret, A. Karar
LLR, Ecole Polytechnique, Palaiseau, France

A.D. Frawley
Florida State University, Tallahassee, FL 32306, USA

B. Hong
Korea University, Seoul, Korea

J. Gosset, H. Pereira
CEA Saclay, Gif-sur-Yvette, France

J.H. Kang, D.J. Kim
Yonsei University, Seoul, Korea

List of Figures

List of Tables

1 Executive Summary

We propose the construction of two Forward Silicon Vertex Trackers (FVTX) for the PHENIX experiment at RHIC. These would extend the vertex capability of the PHENIX Silicon Vertex Tracker (VTX) to forward and backward rapidities with secondary vertex capability in front of the PHENIX muon arms.

The primary technical improvement provided by the FVTX (as well as the VTX) is to allow for the identification of secondary (also called "separated") vertices near the original event vertex. With an expected z-vertex resolution of better than 200 μm, we will see improvement in both tracking from the original vertex as well as through identifying the location of secondary vertices caused by the in-flight decay of particles.

The identification of secondary vertices opens up a wide variety of improvements in the understanding of primary physics processes. In heavy quark (charm and beauty) production, the lifetime of the heavy meson (combined with a significant boost) allows travel of a few millimeters before decaying into a lepton and/or other products. For example, this permits identification of beauty production through the channel $B \rightarrow J/\psi\ X$. We will see that this affects a number of areas of physics exploration. Also, numerous pions and kaons decay into muons and other products in the first few centimeters of their travel, and the event-by-event identification and rejection of this voluminous source of secondary muons will reduce the level of background in a variety of physics channels. Combining secondary vertex identification with the existing muon spectrometers provides a powerful improvement in the capabilities of the muon detector system and extends our physics reach in the large rapidity (η) and low momentum-fraction (x) regions; and with sufficient luminosity, to high transverse momentum.

As a result of this proposed upgrade, numerous areas of physics exploration will be made more accessible, as summarized here in three broad classes associated with the type of collision:

- A+A collisions and the Quark Gluon Plasma:
    - Study of energy loss and flow of heavy quarks into very forward and backward rapidity regions using robust charm and beauty measurements over a much broader x range than available with the barrel VTX detector alone and with much greater precision than is possible with the muon detectors alone. This allows the extension of studies of the geometrical and dynamical effects into the forward and backward rapidity regions of the hot-dense matter created in high-energy heavy-ion collisions.
    - More precise open charm and beauty measurements will provide a solid "denominator" for comparison with production of bound states of heavy

quarks (J/ψ and ϒ). These comparisons will allow for the isolation of common physics, e.g., initial-state effects such as those on the gluon structure function and physics that only affects the bound states, e.g., final-state absorption. These measurements will also provide strong constraints on production of J/ψs from recombination by determining a precise open-charm cross section over a broad rapidity range.

- Permit the direct measurement of ϒs at mid-rapidity by eliminating the large random backgrounds from light-meson decays. Will also improve the mass resolution and signal/background for J/ψ production and enable improved separation of the J/ψ from the ψ'.
- Allow for an unambiguous measurement of the Drell-Yan and heavy-flavor dimuon continuum with elimination of the backgrounds from light mesons.
- Provide a more accurate reaction plane for studies of many other signals, given the much larger rapidity coverage provided by the FVTX.

- p(d)+A collisions and small-x or gluon saturation physics:

  - Permit the study of the gluon structure function modification in nuclei at small *x* values, where gluon saturation or shadowing is thought to be important.
  - Determine the initial state for AA collisions and provide a robust baseline for cold-nuclear matter effects in studies of hot-dense matter in heavy-ion collisions.
  - Help untangle the intricate physics of J/ψ and ϒ production in cold nuclear matter by providing robust measurements of open-heavy quark production that can, by contrast, separate initial and final-state physics for these resonances.
  - Allow for a clean measurement of Drell-Yan which can further help untangle production issues for the J/ψ.

- Polarized p+p collisions, and the contribution of the gluon to the spin of the nucleon:

  - Provide a much larger x range (from $x = 10^{-2}$ down to 10^{-3}) over which the mostly unknown gluon polarization ($\Delta G/G$) can be determined. Without the FVTX the range covered is likely to not be sufficient to study the shape of any polarization or to determine its peak value.
  - Allow for a direct measurement of spin asymmetry in beauty production, which is expected to be different from open charm and light hadrons, thus providing the much-needed cross checks.
  - Enable a clean measurement of W/Z bosons by rejecting muons from light and heavy hadron decays at high p_T.

The main experimental benefits provided by the FVTX detector are in the following areas:

- Identification and rejection of muons from long-lived π and K meson decays
- Identification of charm and beauty decays via displaced vertices
- Explicit identification of beauty production through the channel $B \rightarrow J/\psi$
- Significant improvement of signal-over-background in all dimuon measurements by rejecting decay muons from pions and kaons combined with the rejection of punch-through hadrons
- Improvements in vector meson mass resolutions, e.g., the J/ψ, ψ' and Υ

With the present PHENIX detector, heavy-quark production in the forward and backward directions has been measured indirectly via the observation of single muons. These measurements are inherently limited in accuracy by systematic uncertainties resulting from the large contributions to the single muon spectra from prompt pion and kaon semi-leptonic decays and from pion and kaons which punch through the entire muon system and are mistakenly tagged as muons. In addition, the statistical nature of the analysis does not allow for a model-independent separation of the charm and beauty contributions. The FVTX detector will provide vertex tracking with a resolution better than 200 μm over a large coverage in rapidity ($1.2 < |\eta| < 2.2$) with full azimuthal coverage. This will allow for vertex cuts which separate prompt particles, decay particles from short-lived heavy quark mesons and decay particles from long-lived light mesons (pions and kaons). In addition, beauty measurements can be made directly via $B \rightarrow J/\psi+X$ by looking for a displaced J/ψ vertex, which will allow charm and beauty contributions to be separated in semi-inclusive single lepton measurements. Therefore, with this device significantly enhanced and qualitatively new data can be obtained. A more robust and accurate measurement of heavy-quark production over a wide kinematic range will be possible. This new reach to forward and backward rapidities complements that already planned for the central barrel vertex (VTX) silicon detector, which will cover $|\eta| < 1.2$.

The precision of the J/ψ and other dimuon measurements in AuAu collisions are currently limited by the large amount of combinatorial background that must be subtracted from under the signal. With added rejection power for muons from pion and kaon decays, the significance of all dimuon measurements will greatly improve. Further improvement in these measurements result from the improved mass resolution, which will be attained because of the more accurate determination of the opening angles of the dimuons. All together, these will result in greatly improved dimuon data as well as providing access to several new measurements: separation of ψ' from J/ψ, extraction of Drell-Yan from the dimuon continuum and measurement of upsilons at central rapidity.

The FVTX will be composed of two endcaps, with four silicon mini-strip planes each, covering angles (10 to 35 degrees) that match the two muon arms. Each silicon plane consists of wedges of mini-strips with 50 μm pitch in the radial direction and lengths in the phi direction varying from 1.9 mm at small angles to 13.5 mm at 35 degrees. A resolution

in z_{vertex} of 200 μm can be achieved at a maximum occupancy per strip in central Au-Au collisions of less than 1.5%.

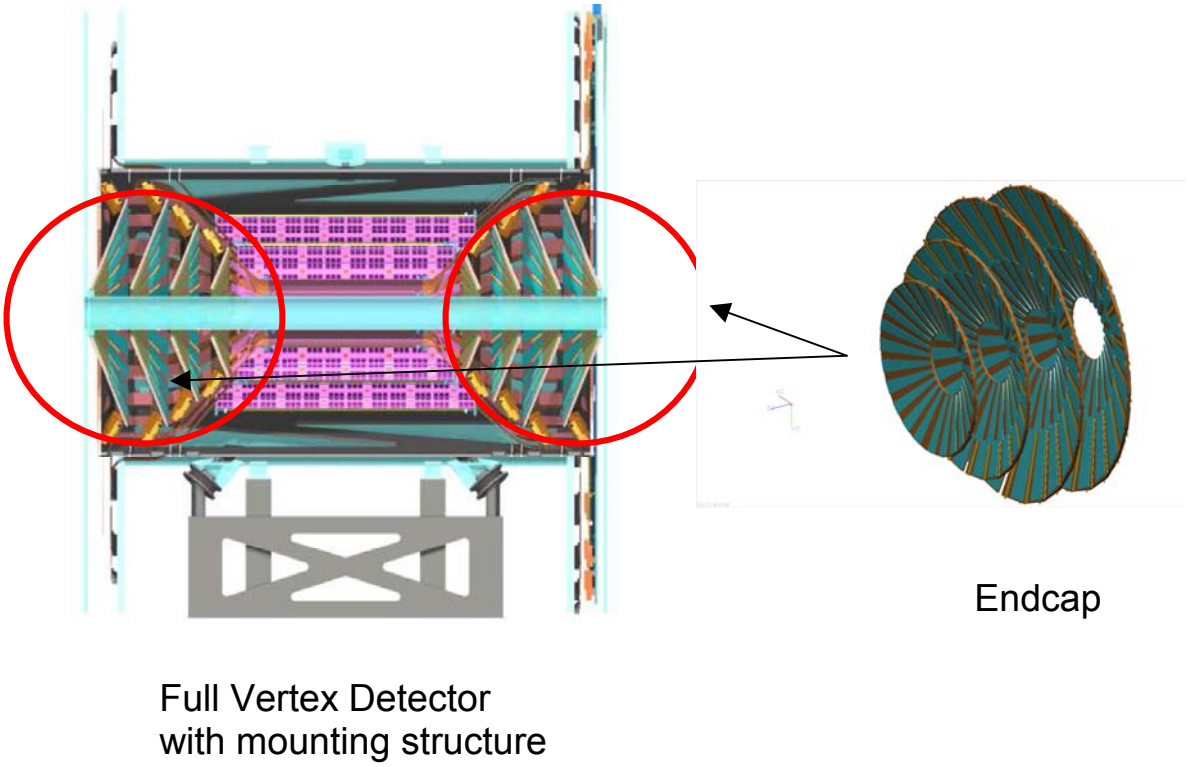

Figure 1 - Conceptual layout of the PHENIX FVTX showing the four lampshade silicon planes of each endcap in the red circles and separately on the right.

The FVTX will have about 1.8 million strips that will be read out with a Fermilab PHX chip, which is flip-chip assembled (bump-bonded) directly to the mini-strips. This chip will provide analog and digital processing with zero-suppression and produces a digital output which is "data-pushed" at 140-840 Mbps to an intelligent readout board containing FPGAs. There the data are prepared in a standard PHENIX format and, in parallel, a fast "level-1" trigger algorithm can be run to select interesting heavy-quark events.

The PHX chip is a slightly modified version of the Fermilab FPIX2.1 front end ASIC developed for BTEV. The silicon mini-strip sensor will be based on a similar wedge design developed for the CMS experiment. The FPIX chip and CMS sensors are both mature designs.

A collaboration of 8 institutions with approximately 40 physicists and engineers has been formed to carry out this project. The collaboration brings expertise in silicon vertex detectors from the FNAL E866, SSC, L3, and BTeV experiments together with general experience on construction and operation of large detector subsystems such as the PHENIX

muon arms. Members of the collaboration come with extensive experience in heavy-quark and J/ψ physics, small-x nuclear effects, gluon structure functions and polarization, various other physics with muons, and expertise in simulations and analysis to support those measurements.

With the help of an LDRD Exploratory Research (ER) grant from LANL during FY02-FY04 we were able to develop a conceptual design of the FVTX and to settle many of the R&D issues necessary to advance to a full proposal. A new LDRD Directed Research (DR) project at LANL (FY06-FY08) will produce a small prototype detector to be installed in the RHIC beam at the same time as the barrel pixel detector (FY08). As part of this effort LANL, Columbia and ISU will advance the R&D for the FVTX by fully designing the interface electronics that connects the PHX read-out chip to the PHENIX data collection modules (DCMs) so that it will seamlessly provide data to the existing PHENIX DAQ. In addition, the LDRD DR project will support the design of the mechanical ladder and support structure.

We anticipate that the full project will be funded by the DOE Office of Nuclear Physics at a total cost of $4.52M ($3.56M + 27% contingency). Construction of the full FVTX detector should proceed starting in early FY08 on a time scale that will allow it to be completed and begin commissioning by the end of FY10.

As a first step towards the full upgrade, we are in the process of designing and building a "prototype" endcap detector that would cover 1/8 of one endcap and is funded by a LANL LDRD-DR grant of $1.25M/year over three years (which also includes a theory component). This prototype will have the same digital backend as the full detector and so the scheme for readout and interface to the PHENIX DAQ will be developed in this effort. Other experience towards the full detector will be gained such as singles rates and other performance aspects. The LDRD prototype will be built during FY06-FY08 and operated for an initial semi-leptonic charm decay measurement by the end of that period. We will not describe further details of this effort here, but they are available on our LDRD-DR part of the FVTX web page[1] and in the proposal listed there.

A preliminary management plan of the FVTX detector project, which also discusses the roles and expected responsibilities of the participating institutions, is included in this document.

The proposal has the following structure:

- The physics motivation for the upgrade and the proposed measurements are documented in section 2.
- The feasibility of these measurements and the required detector performance are discussed in section 3.

- Section 4 gives a detailed description of the vertex tracker and the technical aspects of the proposed project.
- Section 5 discusses our R&D plan.
- A draft of our management plan, section 6, specifies deliverables and institutional responsibilities.
- Section 7 lays out the budget request and the proposed schedule.

2 Physics Goals of the FVTX Endcap Upgrade

The PHENIX Forward Vertex Detector (FVTX) endcaps complement the barrel vertex detector (VTX) already being built for PHENIX by providing much larger coverage in rapidity (two additional units of rapidity compared to about one), extending the sensitivity to gluon momentum fraction (x) down to $x \sim 10^{-3}$, and providing a broad reach in transverse momentum. Heavy-quark mesons and bound states of heavy-quarks (quarkonia) coming from beauty meson decay can be identified by their short detached vertices, and the light-meson yields that ordinarily comprise most of the backgrounds to these measurements can be largely eliminated according to their large detached vertices. Prompt muons and kaons which punch through the muon system can be eliminated by their lack of a displaced vertex.

We will now discuss the main physics goals by starting with those that are important in heavy-ion collisions, then those of interest in proton or deuteron nuclear collisions, and finally those that are related to polarized proton collisions.

2.1 Heavy-ion Collisions and the Quark Gluon Plasma

The main goal of the RHIC program is the identification and study of the hot high-density matter created in heavy-ion collisions, i.e. the Quark Gluon Plasma (QGP). The energy loss in this dense matter as seen by the suppression in the yields at high transverse momentum for light quarks, the large flow seen at small momenta indicative of early thermalization, and other signatures observed by the RHIC experiments point to large densities created in these collisions. But the composition of this high-density matter, whether or not it is deconfined, and what the degrees of freedom are, remain beyond the reach of present measurements. The FVTX detector coupled with the muon detector systems will allow for precision measurements of open charm and beauty versus rapidity, p_T and reaction plane, much improved measurements of vector mesons (J/ψ, ψ', Υ) as well as an unambiguous measurement of dimuons from Drell-Yan in heavy-ion collisions. These measurements will allow one to understand heavy quark energy loss and flow in heavy-ion collisions, contributions of prompt production and quark recombination to vector meson production, separation of initial-state and final-state modifications to charmonium production, and provide important reference measurements from Drell-Yan.

2.1.1 Energy Loss and Flow of Heavy Quarks

One of the most significant physics results in the first several years of RHIC operations was the strong suppression of high-p_T light particle production, shown in Figure 2, that is interpreted as energy loss in dense matter for the outgoing particles or jets[ii,iii,iv]. A large elliptical flow (asymmetry with respect to the reaction plane) is also seen for the light hadrons as shown in Figure 3.

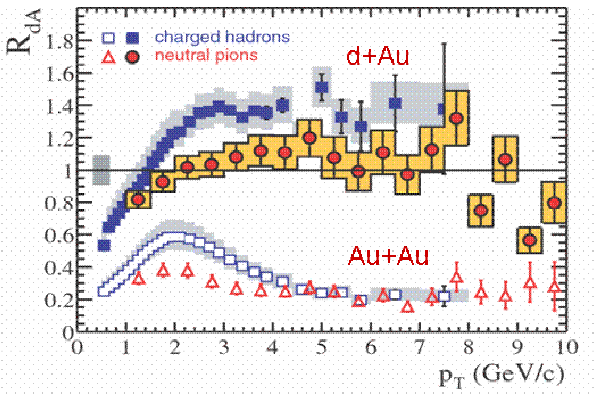

Figure 2 - Suppression of high-p_T hadrons and pions as seen in Au+Au vs d+Au collisions.

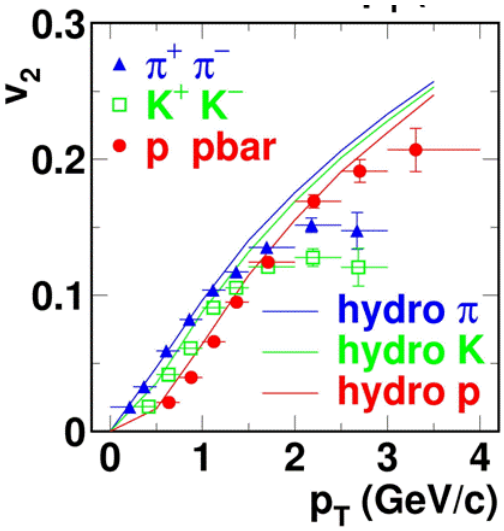

Figure 3 - Large elliptic flow for light hadrons in Au+Au collisions is near the hydrodynamic limit[v].

More recent measurements are beginning to give some evidence that even heavy quarks (charm and beauty) suffer substantial energy loss in the final state (see Figure 4) and even appear to flow, though the flow measurements at high p_T are rather imprecise and somewhat inconsistent between the PHENIX and STAR measurements (Figure 5). These results have primarily come from the central rapidity detectors although some early results from the muon spectrometers are beginning to emerge. But for all these measurements large backgrounds and the necessity to calculate non-heavy-quark contributions to the single lepton spectra and then statistically subtract these to isolate the heavy-quark component with low signal/background ratios give large systematic errors and limit the accuracy of these measurements. Also there is not a clean way to separate the charm and beauty components of the resulting subtracted spectra. The FVTX detector will address both of these issues with heavy flavor measurements.

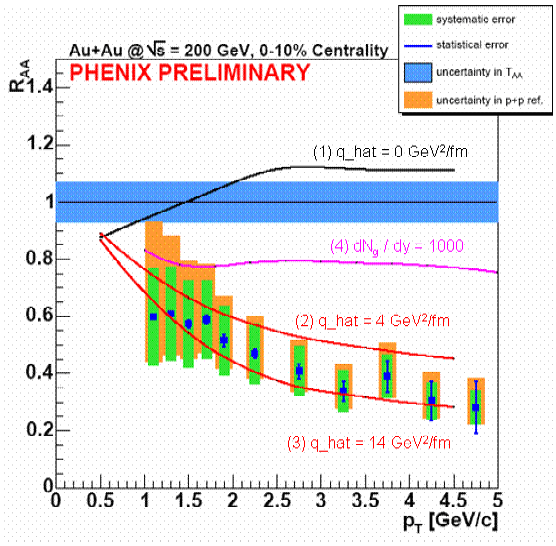

Figure 4 - In PHENIX preliminary results[vi] shown at QM05, even charm seems to suffer energy loss at mid-rapidity.

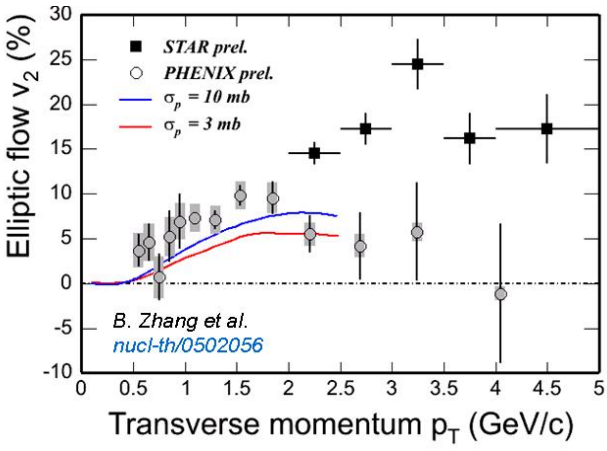

Figure 5 - Preliminary results for charm from single electrons in PHENIX[vii] and STAR[viii] shows flow for small p_T and conflicting results from PHENIX and STAR as to whether the flow returns to zero for larger p_T[ix].

One can pose several important classes of questions related to the interaction of heavy quarks with the hot-dense (QGP) matter created in central heavy-ion collisions that will be addressed by the FVTX upgrade:

- How does energy loss and flow differ between light and heavy quarks?
- What is the rapidity dependence of the suppression or energy loss of heavy quark production in heavy-ion collisions and how can one understand it taking into account the density and geometry of the hot-dense matter that is created? For example, given the additional boost of heavy quarks in the forward direction and differences of the time-dependence of the hot-dense region in the longitudinal versus transverse directions, the rapidity dependence should characterize these differences and help us understand the dynamics and properties of the dense medium.
- How will the flow at lower momentum or the asymmetry with respect to the reaction plane change as one goes more forward and how can this be understood theoretically? This should be sensitive to the density left behind from the collision or to stopping and its evolution, with differences between forward and central rapidity.

Predictions before the most recent data were that heavy quarks would not lose much energy in hot-dense matter due to the "dead-cone" effect[x], but this appears inconsistent with the emerging results. Recent studies suggest that the magnitude of the dead-cone[xi,xii,xiii] may be smaller than anticipated in reference x, which would lead to an energy-loss for heavy quarks closer to that for light quarks.

At the opposite extreme, Batsouli *et al* [xiv] have suggested that the first electron measurements at RHIC, which showed N_{Binary} scaling of heavy quark production in AuAu collisions, can be reproduced by assuming that charm particles flow hydro-dynamically, i.e. the charm particles interact with the medium with a large cross-section. To distinguish between these effects and to explore this physics will require precise measurements of the p_T spectra for open charm at high transverse momentum, out to several GeV/c. This point is illustrated in Figure 6. The figure, taken from reference xiv, illustrates that the p_T distribution of *D* mesons and single electrons from charm have little difference in the two extreme scenarios of pQCD with no heavy-quark energy loss (shown in dashed curves) and a hydrodynamic model with charm and beauty flow (shown as solid curves), within the p_T range accessible by the 2002 PHENIX setup. Obviously, a much more precise measurement at much higher p_T is required to distinguish the models. Such a measurement is not feasible without the FVTX and VTX upgrades due to the large backgrounds and ambiguity of charm and beauty contributions.

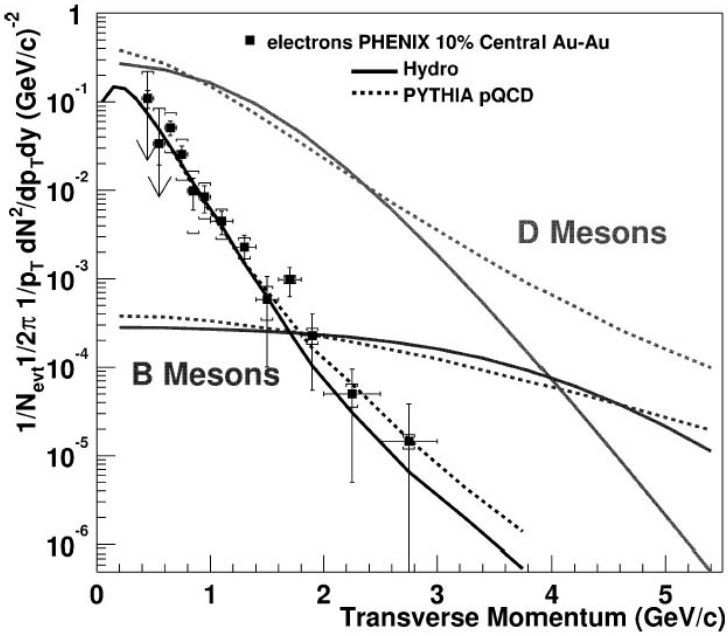

Figure 6 - Single electron data[xiv] of PHENIX compared with two extreme models of charm p_T distribution.

Other theoretical pictures [xv] suggest that heavy and light quarks will behave quite differently because the heavy quarks will fragment or hadronize within the dense matter, while the light quarks will fragment outside. So for heavy quarks the process is more complicated with both quark energy loss and fragmentation occurring in the medium. This behavior would presumably depend on the rapidity of the observed leading particles or jets. Thus the large coverage in rapidity provided by the FVTX will be quite important for the heavy-quarks as well as for the light quarks as discussed in 2.1.4.

Clearly the FVTX detector upgrade will be critical in helping to determine which of the above theoretical pictures are reflected by the real data as it will provide much more

precise heavy quark cross section and flow measurements, combined with the VTX will cover a very large rapidity range, will much improve the p_T coverage at forward rapidity, and will allow for separation of charm and beauty components to the heavy quark spectra.

2.1.2 Open Charm and Beauty Enhancement

It has been predicted that open charm production could be enhanced in high-energy nucleus-nucleus collisions relative to the expectation from elementary collisions[xvi,xvii,xviii]. Heavy quarks are produced in different stages of a heavy ion reaction. In the early stage charm and beauty are formed in collisions of the incoming partons. The yield of this component is proportional to the product of the parton density distributions in the incoming nuclei (binary scaling). If the gluon density is high enough a considerable amount of charm can be produced via fusion of energetic gluons in the pre-equilibrium stage before they are thermalized. Finally, if the initial temperature is above 500 MeV, thermal production of charm can be significant. The last two mechanisms (pre-equilibrium and thermal production) can enhance charm production relative to binary scaling of the initial parton-parton collisions. These are the same mechanisms originally proposed for strangeness enhancement, but in the case of charm may reveal more about the critical, early partonic-matter stage of the reaction since the rate of heavy-quark production is expected to be negligible later when the energy density has decreased. In comparison, strangeness production is expected to continue even in the final hadronic stages of the reaction.

At RHIC energies the anticipated enhancement is a small effect[xvii,xviii]. The contributions to charm production from various stages of a Au+Au collision are shown in Figure 7 (taken from reference xvii). From the left panel of the figure it is evident that for an initial energy density of 3.2 GeV/fm^3 the pre-thermal or pre-equilibrium production contribute about 10% of total charm production, while the thermal contribution is negligible. However, the yield is very sensitive to the initial density, and with 4 times the energy density the pre-equilibrium contribution can be as large as the initial fusion. This is illustrated in the right panel of the figure. Present single electron measurements of PHENIX indicate that within ~25% systematic uncertainty charm production approximately scales with the number of binary collisions. Thus, charm enhancement, if it exists, cannot be a large effect. A measurement of the charm yield with substantially higher accuracy and precision is therefore required to establish a potential charm enhancement.

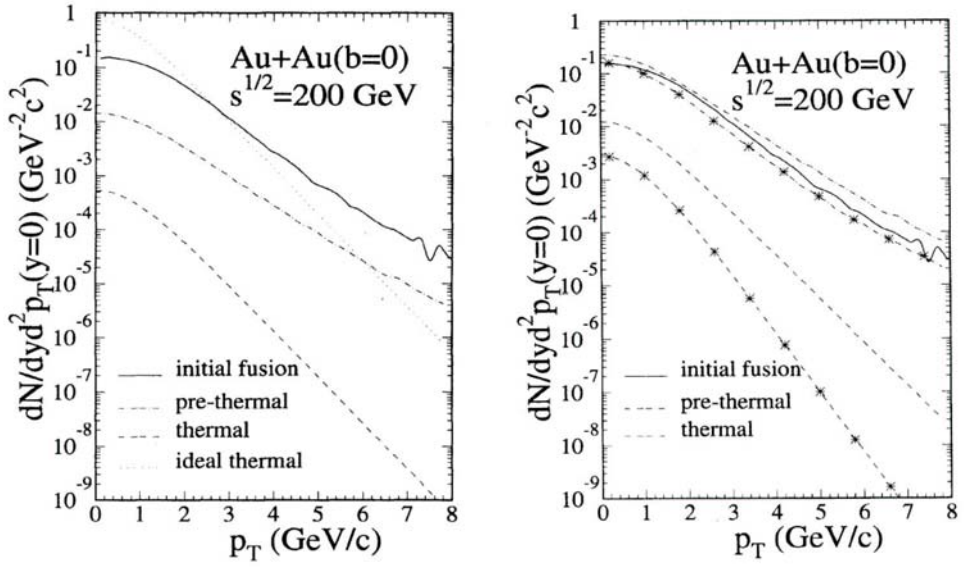

Figure 7 - Charm enhancement expected at RHIC from ref. xvii. In both panels, contribution from the initial gluon fusion (solid), pre-thermal production (dot-dashed), and thermal production (dashed, lowest) are shown. The left panel is the calculation with energy density of 3.2 GeV/fm^3, while the right panel shows the case with energy density 4 times higher. The barely visible dotted curve in the left panel figure is the thermal production assuming an intial fully equilibriated QGP. In the right panel the curves with stars are the same as the corresponding curves without stars except that the initial temperature is reduced to 0.4 GeV (compared to 0.55 GeV).

The FVTX combined with the muon spectrometers will allow measurements of charm and beauty over a much broader range in p_T. This will extend the single muon measurement to the p_T region near 0.5 GeV/c, which is essential for an accurate determination of the p_T integrated charm yield at forward and backward rapidities, since more than half of the yield from charm decays is in this p_T region. Approximately one third of the total charm cross section is expected to come from the rapidity range measured by the FVTX, as shown in Figure 8. Combined with the central rapidity ($|y|<1.2$) measurement from the VTX detector, this will allow an accurate measurement of the total charm cross section which then allows us to see a potential charm (or beauty) enhancement.

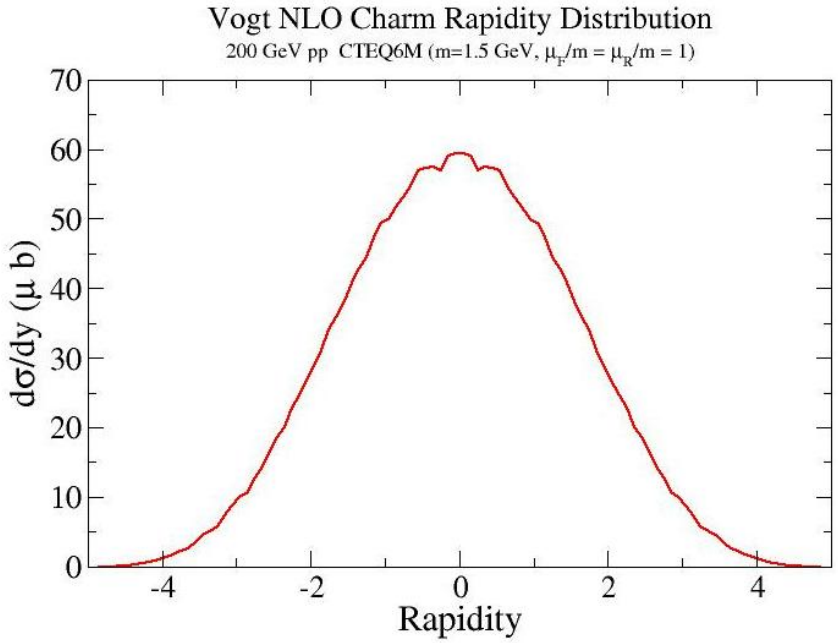

Figure 8 - Rapidity distribution from Vogt[xix] for charm in pp collisions at √s = 200 GeV. One third of the total cross section comes from the region of the FVTX coverage, |y|>1.2

2.1.3 J/ψ Suppression and Comparisons with Open charm, ψ' and Y

J/ψ production in heavy-ion collisions is a complicated process that can be both difficult to dissect but also allows the possibility to understand several features of heavy ion collisions at the same time, if the measurement is precise enough and it is used in conjunction with other relevant measurements, such as open charm production. J/ψ production can be modified in AuAu collisions with respect to pp collisions by modification of the gluon distribution functions in a nucleus, energy loss of the composite charm quarks in the medium, contributions to the production from both prompt production and recombination (if the charm density is high enough), as well as the historical prediction of suppression due to Debye screening in a plasma. To quantitatively understand this suppression/enhancement requires knowledge of the initial production of $c\bar{c}$ pairs and the effect of cold nuclear matter on production. The effectiveness of a deconfined medium in preventing the formation of J/ψ can be quantified using the ratio J/ψ/(open charm) ratio using open charm in the same acceptance as that for the J/ψ. The FVTX upgrade provides for the detection of open charm over about the same rapidity interval as for J/ψ decays to dimuons. In addition, the J/ψ measurement uncertainties in AuAu interactions are currently dominated by the amount of background that must be subtracted from the J/ψ peak, even with a limited detector acceptance chosen to reduce the backgrounds. The addition of the FVTX will greatly enhance the J/ψ measurement in the forward region by eliminating most of the combinatorial background that comes from pion and kaon decay muons and by improving the mass resolution (see Figure 9) which results from a more accurate measurement of the dimuon opening angle.

The measurement of the production of ψ' and ϒ will also greatly improve the understanding of J/ψ production as they have larger and smaller Debye screening lengths, respectively. The ϒ provides a comparison of beauty production to charm production, while the ψ' shares much of the same production issues as the J/ψ but does not suffer from feed-down from other states. These, combined with open charm measurements, should allow for separation of initial state and final state modifications to J/ψ production.

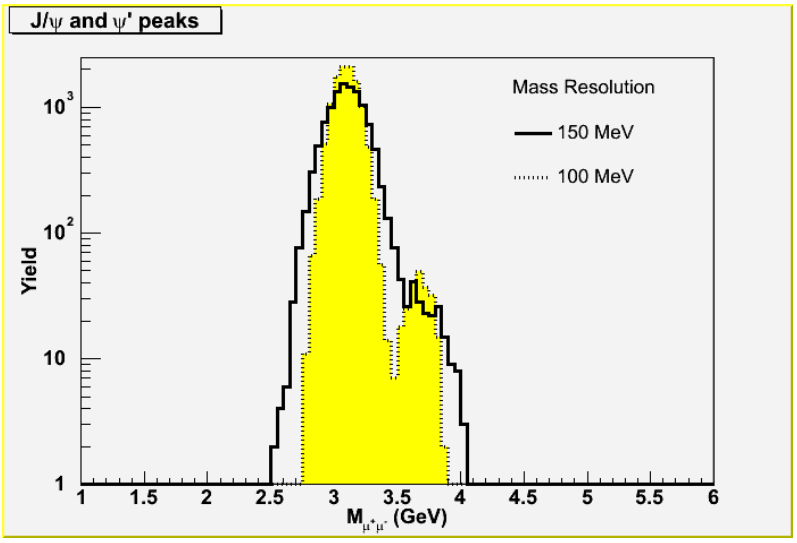

Figure 9 - Mass spectra for the J/ψ and ψ', showing the substantial improvement in separation expected with a vertex detector (yellow, 100 MeV resolution) compared to that without a vertex detector (black, 150 MeV resolution). The number of J/ψ and ψ' in this plot represents our expectation for a ~25 pb^{-1} p+p run.

2.1.4 Reaction Plane and Azimuthal Asymmetries

The large increase in the overall solid angle for observing charged particles provided by the FVTX (plus a more optimal rapidity coverage) will result in a substantial improvement in the reaction plane resolution, which will aid in the study of many signals in PHENIX versus reaction plane. Many physics measurements made by PHENIX with respect to the reaction plane are more limited by the reaction plane resolution than by other systematic or statistical errors, so this is a critical improvement to the PHENIX physics program.

2.1.4.1 Reaction Plane

The determination of the reaction plane for heavy ion collisions from charged particle asymmetries is very important for it allows the measurement of observables (e.g. charm R_{AA}) as a function of path length in the medium. It is generally agreed upon that in mid central collisions the path length in plane is much smaller than out of plane due to the almond shaped overlap zone. A binning of the reaction plane orientation into e.g. 3 bins

would therefore allow for path length dependency study of various physics signals with a 60 degree separation of in and out of plane bins (±30 degrees).

In order to avoid auto correlations, the reaction plane has to be determined in a region that does not overlap with the actual measurement, e.g. current central rapidity measurements with respect to the reaction plane use the BBC information at much higher rapidity to determine the reaction plane. Alas, Figure 10, which shows a measurement with the MVD pad detectors for minimum bias Au-Au collisions from run4, demonstrates that the elliptic flow at the magenta shaded rapidity region for the former MVD pad detectors and the currently proposed FVTX exhibits a stronger v2 signal than at BBC rapidity and should therefore provide a reaction plane measurement with better resolution.

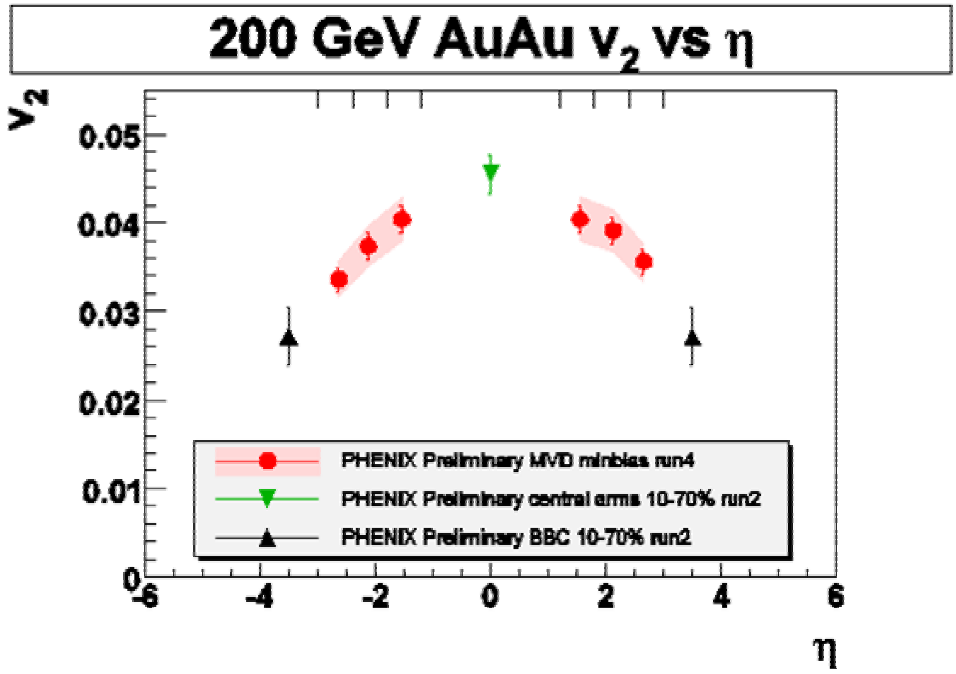

Figure 10 - Azimuthal asymmetry v2 as function of pseudo rapidity for minimum bias A-A collisions at 200 GeV. The measurement from run 4 with the MVD pad detectors is colored in magenta; the FVTX will cover the same range in pseudo rapidity.

A simulation has been performed to study to reaction plane resolution and confidence levels for providing 'reaction plane bins' and will be discussed in the following. The simulation has been validated with the MVD pad detector measurements from run4.

The typical way to measure or report a reaction plane resolution is quoting the square root of two times the mean cosine of the difference between reaction planes obtained from two subsets of tracks, in this case the north and south tracks. For this is a rather complex variable we choose to first represent it in Figure 11 and then translate it into a more intuitive variable in Figure 12 namely a confidence level of having made the right determination.

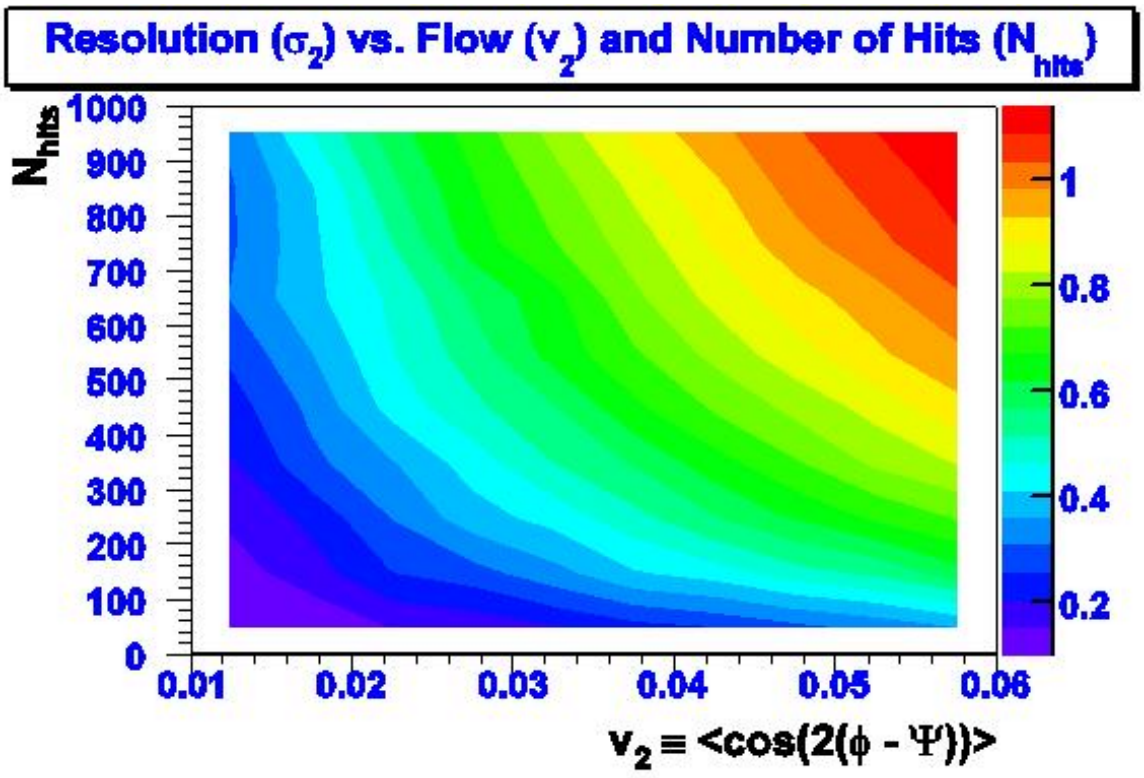

Figure 11 - The two dimensional color representation of the mean reaction plane resolution as function of the charge particle multiplicity Nhits and the elliptic flow signal v2 present in the rapidity interval of the detector. The total number of charge tracks expected for a mid central Au-Au collision at 200 GeV is simulated to be about 800 traversing the FVTX silicon detector, the previously measured elliptic flow signal v2 is on the order of 0.035, the resulting expected mean reaction plane resolution is approximately 0.75.

Figure 11 shows in color the square root of the mean cosine of the reaction plane difference between north and south detector as function of the track multiplicity (here called Nhit), i.e. the reaction plane resolution on the ordinate. The flow signal v2 present in the given rapidity interval of the detector is shown on the abscissa. The general trend visible is that the reaction plane resolution is increasing with the number of charged tracks and increasing with the strength of the elliptic flow signal v2. The red colored top right corner marks the area with yields the best resolution.

Studies from Hijing have shown that the mean number of charged tracks to be expected for the FVTX is on the order of 400 tracks per endcap, i.e. about 800 charged tracks total.

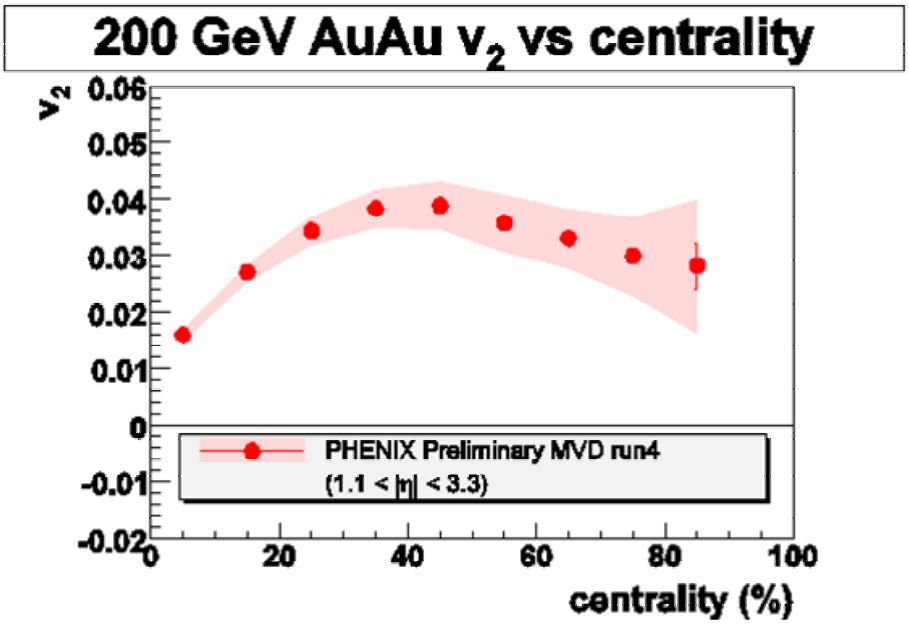

Figure 12 - Azimuthal asymmetry v2 (elliptic flow) as function of centrality for A-A collisions at 200 GeV. The measurement was obtained with the MVD pad detectors which covered in run 4 the same pseudo rapidity rage as the FVTX will in the future.

The elliptic flow measurement i.e. v2, shown in Figure 12 as a function of centrality for Au-Au collisions at 200 GeV, indicates that the expected value v2 is about 0.035 for mid central collisions. The expected reaction plane resolution we obtain via Figure 11 is therefore about 0.75.

Figure 13 shows in color the expected confidence levels (measured from 0 to 100 percent or as on the z-axis label from 0 to 1.) as function of the reaction plane bin size (see above), i.e. delta phi on the ordinate and the reaction plane resolution on the abscissa. For a given bin size in delta phi one can see that the confidence level that the actual reaction plane lies in the measured reaction plane bin increases with the reaction plane resolution. It also shows that a 2 sigma confidence level can only be reached in the limit of two broad bins - in and out of plane - with a nearly perfect detector.

If we interpret Figure 13 with the number for the reaction plane resolution obtained above (0.75) and assume that we want to have 3 bins in reaction plane as mentioned earlier (i.e. ±30 degrees around the major axis plus a 60 degree gap), then obtain a confidence level of about 65 percent; two broad bins - in vs. out - will have a confidence level of 85 percent, a very good measurement.

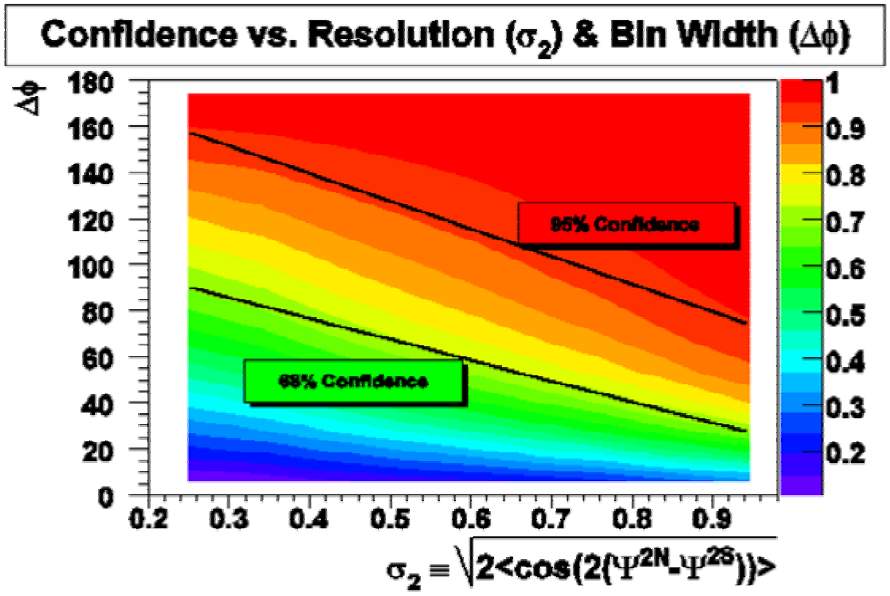

Figure 13 - Three dimensional representation of confidence level (0 to 1 corresponds to 0 to 100 percent) of a given delta phi bin as function of the mean reaction plane resolution. The reaction plane resolution of 0.75 estimated in figure 4 would result is a 65 percent confidence level if binning the reaction plane into 3 bins. Two bins (delta phi = 90 degrees) will give a confidence level of 85 percent for the 'true reaction plane' being in the measured bin.

2.1.4.2 Flow Measurements

In addition to providing a reaction plane for the central detector measurements the FVTX can obviously measure the actual elliptic and directed flow signal, being of increase importance for PHOBOS will be decommissioned. In the following we discuss the measurements obtained with the MVD pad detectors in run4 which covered about the same rapidity range and were already shown above in the context of the reaction plane measurements.

Figure 10 shows the measurements of the azimuthal asymmetry v2 as function of the pseudo rapidity with three sets of PHENIX detectors. The measurement obtained with the MVD is colored in magenta, it shows a sizeable v2 which translates into a good reaction plane measurement. In the future running of RHIC, PHOBOS, which provided valuable flow measurements in the past, will no longer be taking data so it is important that asymmetry measurement in the intermediate rapidity range will be provided by PHENX. The FVTX has an improved granularity and the same rapidity coverage as the former MVD pad detectors. In addition the measurement of asymmetries and reaction plane will be improved by using tracklets in the four FVTX planes rather than just hits as was done in the MVD analysis.

Figure 12 and Figure 14 show elliptic and directed flow measurements with the MVD pad detectors as function of centrality for Au-Au collisions. The proposed FVTX will provide for the same measurements, alas with better statistical and systematic error bars. Simulations on the FVTX performance have begun.

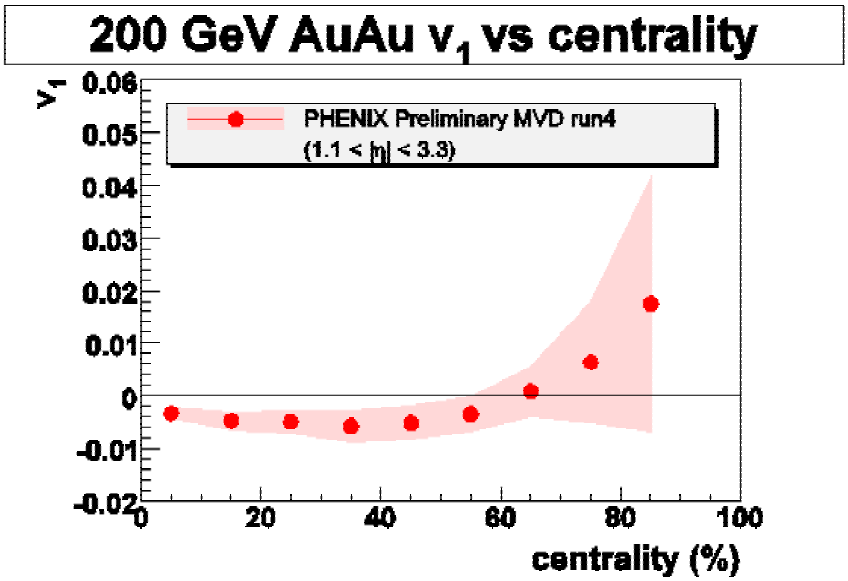

Figure 14 - Azimuthal asymmetry v1 (directed flow) as function of centrality for A-A collisions at 200 GeV. The measurement was obtained with the MVD pad detectors which covered the same pseudo rapidity rage as the FVTX will.

2.2 Proton(Deuteron)+Nucleus Collisions and Nuclear effects on Gluons in Nuclei

Proton-nucleus collisions not only provide important baseline information for the study of QCD at high temperatures, they also address fundamental issues of the parton structure of nuclei. Since the discovery of the EMC effect in the 1980s, it is clear that the parton-level processes and the structure of a nucleon are modified when embedded in nuclear matter[xx]. These modifications reflect fundamental issues in the QCD description of parton distributions, their modifications by the crowded nuclear environment of nucleons, gluons and quarks, and the effect of these constituents of the nucleus on the propagation and reactions of energetic partons that pass through them.

2.2.1 Shadowing or Gluon Saturation via Heavy-quarks Measurements

Of particular interest is the depletion of low momentum partons (gluons or quarks) in nuclei, called shadowing, which results from the large density of low momentum partons. For gluons at very low momentum fraction, $x < 10^{-2}$, one can associate with them, following the uncertainty principle, a large distance scale. These gluons will then interact strongly with many of their neighbors and by gluon recombination or fusion are thought to promote themselves to larger momentum fraction, thus depleting small values of x. In most models the overall momentum is conserved in this process, so that the small x gluon region is depleted while the moderate x region above that is enhanced. In recent years a model for gluon saturation at small x has been discussed extensively by McLerran and

collaborators[xxi]. Gluon saturation affects both the asymptotic behavior of the nucleon's gluon distribution as *x* approaches zero and causes shadowing.

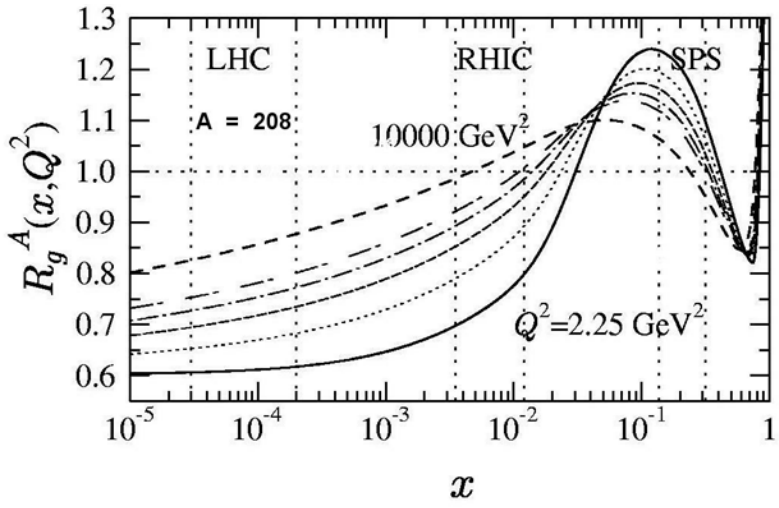

Figure 15 - Gluon shadowing from Eskola[xxii] as a function of x for different Q^2 values: 2.25 GeV^2 (solid), 5.39 GeV^2 (dotted), 14.7 GeV^2 (dashed), 39.9 GeV^2 (dotted-dashed), 108 GeV^2 (double-dashed) and 10000 GeV^2 (dashed). The regions between the vertical dashed lines show the dominant values of x_2 probed by muon pair production from charm pairs at SPS, RHIC and LHC energies.

At RHIC energies many of the observables are affected by gluon distributions at small *x* where nuclear shadowing is thought to be quite strong. However, theoretical predictions of the amount of shadowing differ by factors as large as three. For example, in the production of J/ψ in the large rapidity region covered by the PHENIX muon arms, models from Eskola et al (EKS)[xxii] (Figure 15) predict only a 30% reduction due to gluon shadowing, while those of Frankfurt & Strikman[xxiii] (Figure 16) or Kopeliovich[xxiv] predict up to a factor of three reduction.

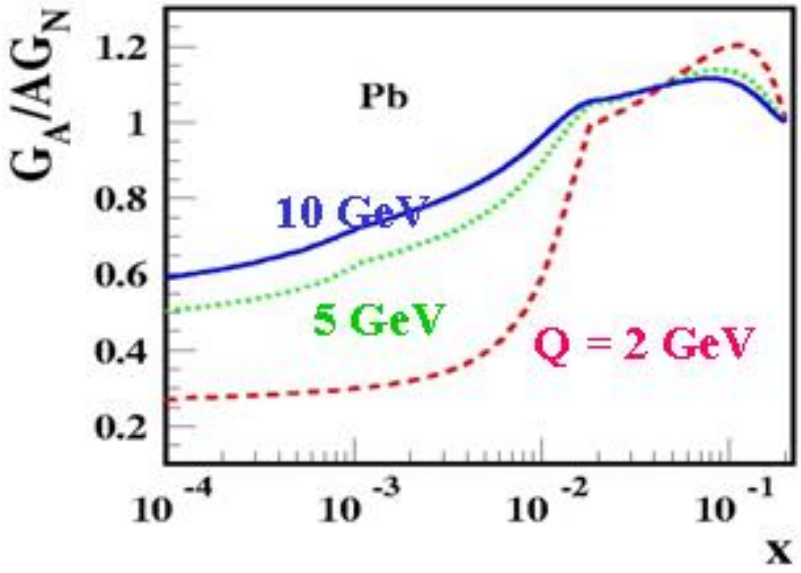

Figure 16 - Gluon shadowing prediction from Frankfurt and Strikman[xxiii], which shows substantially larger gluon shadowing than that of EKS[xxii].

The coverage in *x* for the FVTX is indicated in Figure 17, superimposed on calculations of the ratio of nuclear to nucleon gluon structure functions. The red bars indicate the additional coverage provided by the FVTX upgrade compared to the baseline of PHENIX. The FVTX extends the *x*-range from the anti-shadowing region into the shadowing domain, which means we will be able to establish the shape of the gluon structure function in nuclei. The shadowing region is not accessible with the VTX barrel-only upgrade. While the *x*-range for J/ψ production also extends into the shadowing range, final state effects, such as dissociation, complicate the extraction of the gluon structure function. Open charm and beauty measurements are unaffected by these final state effects.

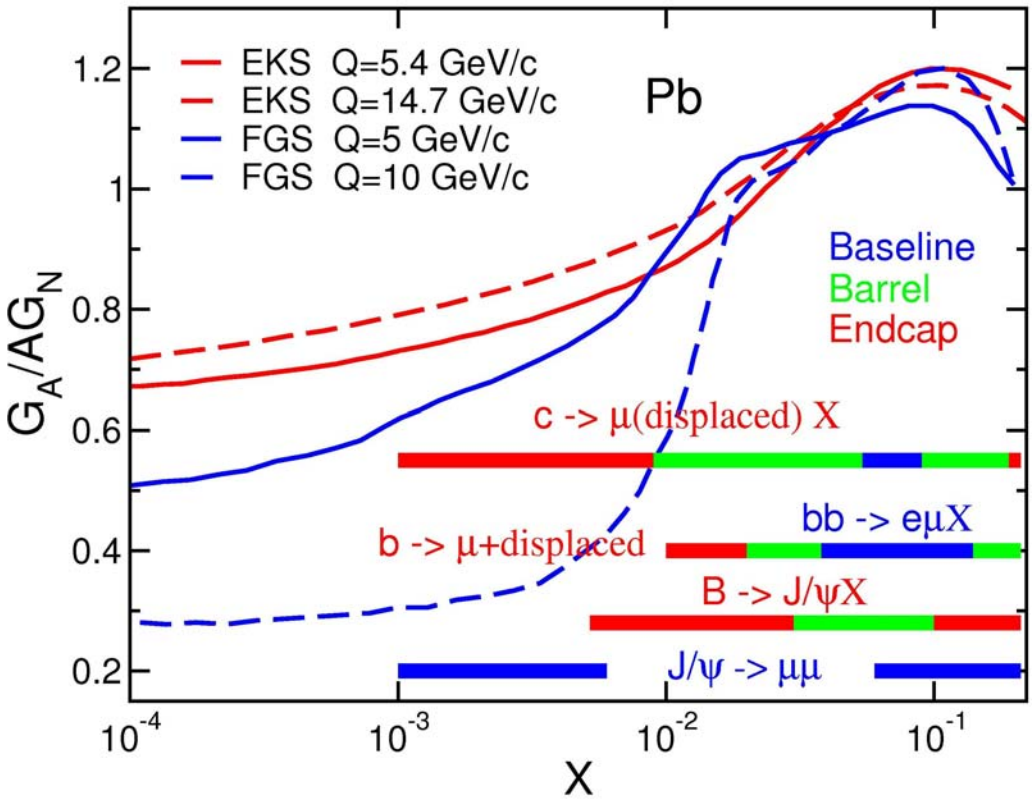

Figure 17 - Gluon shadowing predictions along with PHENIX coverage. The red bars indicate the additional range provided by the FVTX upgrade, green bars are for the barrel (VTX) upgrade, while the blue bars cover the PHENIX baseline. The red and blue curves are the theoretical predictions for gluon shadowing from EKS[xxii] and FGS[xxiii] for different Q values.

It should also be noted that alternative models, such as those involving higher-twist (power corrections) effects from Qui and Vitev[xxv], can also give reductions in the gluons at forward rapidity. These effects arise from the final state rather than the initial state. Similarly, Kopeliovich has argued that suppression at large rapidity may be caused by Sudakov suppression[xxvi].

2.2.2 Disentangling the Physics of J/ψ and Quarkonium Production in Nuclei

Recent measurements by PHENIX of the J/ψ nuclear dependence for d+Au collisions[xxvii] are shown in Figure 18 and indicate weaker absorption and shadowing than expected. The large rapidity region corresponds to small momentum fraction in Au, the region where shadowing is thought to be important. Extraction of gluon densities from these measurements is not only hampered by the poor statistical precision of the present d+Au data, but also by theoretical issues including the possibility that much of the suppression at large rapidity might come from either initial-state energy loss of the gluon from the projectile[xxviii] or from Sudakov suppression effects on the final-state $c\bar{c}$ [xxvi]. Increased statistics from higher luminosity runs and more definitive measurements via observables that are sensitive to gluon structure functions in several different channels will be

necessary to test the theory with sufficient power to constrain the underlying QCD processes.

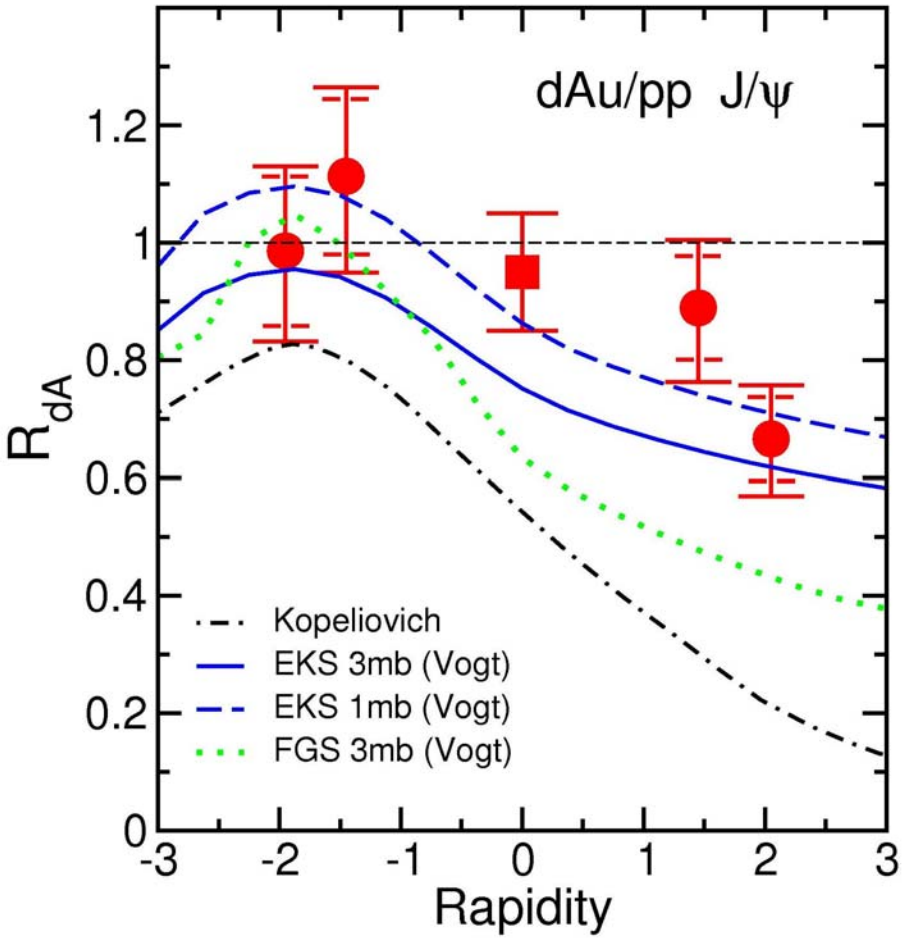

Figure 18 - J/ψ nuclear dependence versus rapidity compared to theoretical predictions with several types of gluon shadowing[xxvii].

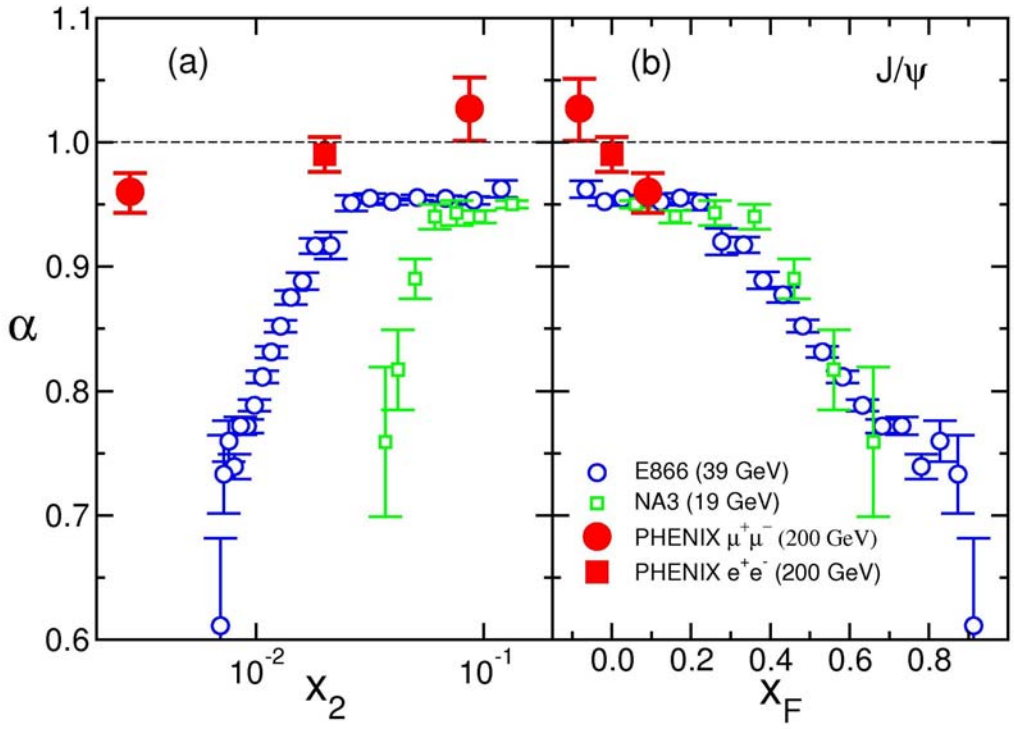

Figure 19 - Alpha versus x_2 and x_F from measurements at three different energies shows that the suppression does not scale with x_2 but does exhibit approximate scaling with x_F. Alpha is defined as $\sigma_A = \sigma_p A^\alpha$, where σ_p (σ_A) is the nucleon (heavy nucleus, A) cross section. Data is from PHENIX (√s = 200 GeV)[xxvii], E866/NuSea (√s = 39 GeV)[xxix] and NA3 (√s = 19 GeV)[xxx].

Earlier data from lower-energy fixed-target p+A measurements at Fermilab (E866) are shown in Figure 19, compared to data from PHENIX and NA3. They show much stronger suppression at large x_F (or small x_2), where x_2 is the momentum fraction of the gluon in the nucleus and $x_F = x_1 - x_2$ (x_1 being the momentum fraction of the gluon from the proton projectile). A stronger absorption at mid-rapidity is seen in the lower energy experiments than with the PHENIX experiment. The lack of scaling versus x_2 for the three experiments indicates that the observed suppression is not dominated by shadowing, and suggests that energy loss and other nuclear effects are playing important roles in modifying J/ψ production, at least at lower energies.

It is clear that precise knowledge of the shadowed gluon structure functions in nuclei is essential towards understanding several of the important signatures for QGP in heavy-ion collisions at RHIC, including modification of open and closed heavy-quark production with respect to p-p collisions. Recombination models for J/ψ production, which might cause an enhancement of that production in heavy-ion collisions due to the large density of charm quarks created in a collision, must be constrained by an accurate measurement of the amount of charm produced, given the shadowing of the gluon densities in the colliding nuclei.

In the J/ψ studies done at CERN by NA38/50[xxxi] the J/ψ yields were usually divided by the Drell-Yan dimuon yields, since the latter should have little nuclear dependence. But this is actually an unnatural procedure since the Drell-Yan process involves quarks (q-qbar annihilation) while J/ψ production involves gluons (gluon fusion). The nuclear effects on the initial parton distributions for quarks and gluons and their energy loss in the initial state before the hard interaction are both also likely different. Additionally the yields of Drell-Yan dimuon pairs were quite small at CERN and dominated the statistical uncertainties in this ratio. The relative rates for Drell-Yan at PHENIX are even smaller and such a ratio makes even less sense here. It is much more natural to compare J/ψ production to open-charm production, where the initial-state effects are probably the same. Therefore a robust measurement of open-charm is quite important for the physics of the J/ψ. Of course, it has also been suggested by some theoretical groups[xxxii] that the effective gluon distributions are process dependent, and different for open- versus closed-charm production. These models suggest that such a difference, if seen by comparisons of open and closed charm, would indicate that higher-twist contributions to closed charm production are substantial.

Another area of importance, especially to the J/ψ measurements, is the production of beauty quarks. The decay of B-mesons will produce J/ψs (BR ~ 1.14%) that tend to have somewhat higher p_T than for prompt J/ψ. In a scenario where color-screening in a QGP created in heavy-ion collisions destroys most of the J/ψs, it is conceivable that, particularly at higher p_T, the remaining J/ψs are dominated by those that come from B decays. An estimate of this from Lourenco[xxxiii] several years ago indicated that for central collisions the fraction of J/ψs from B decays might be as large as 20% overall, with even larger fractions at high p_T. Clearly one would like to measure the B cross sections at RHIC energies so that a more reliable estimate of their contribution to J/ψ production can be made, an issue which would be particularly important should a large suppression of J/ψs be seen in central Au-Au collisions at RHIC. How much suppression is actually occurring in the plasma would be difficult to determine without establishing what fraction of the remaining J/ψs do come from B decays.

In addition, given sufficient RHIC luminosity, it would be quite instructive to measure for beauty the same observables already discussed for charm, and to compare these results. As the RHIC luminosity increases we will also be able to measure the ϒ, a $b\bar{b}$ bound state; and for it, a comparison with open-beauty will obviously be important.

The FVTX can also enable measurements of ϒ at mid-rapidity for decays that give one muon in each of the two muon arms. The study of ϒs provides an important comparison to J/ψs for a system composed of beauty instead of charm quarks that is smaller and more tightly bound. Previous measurements at lower energies showed weaker absorption in the final-state than that observed for the J/ψ. A solid baseline for ϒ production is also, of course, critical for comparisons with the J/ψ in nucleus-nucleus collisions where the heavier ϒ should not be screened by the QGP and also should not have large contributions to its production from recombination of beauty quarks, since their production (at RHIC) is too small to give substantial recombination.

While PHENIX has recently observed an ϒ signal for decays with both muons detected in a single arm, the ϒs with one muon in each arm are swamped by copious background from random pairs of muons. This background (shown for dAu collisions in Figure 20) turns on at pair masses of about 5 GeV, corresponding to the sum of the single muon momentum thresholds in the two muon arms, and makes it impossible to see the small signals from mid-rapidity ϒs and Drell-Yan. With the FVTX we can remove, on an event-by-event basis, the light hadron decays which cause most of these random pairs and should be able to observe a clean Upsilon and high-mass Drell-Yan signal at mid-rapidity.

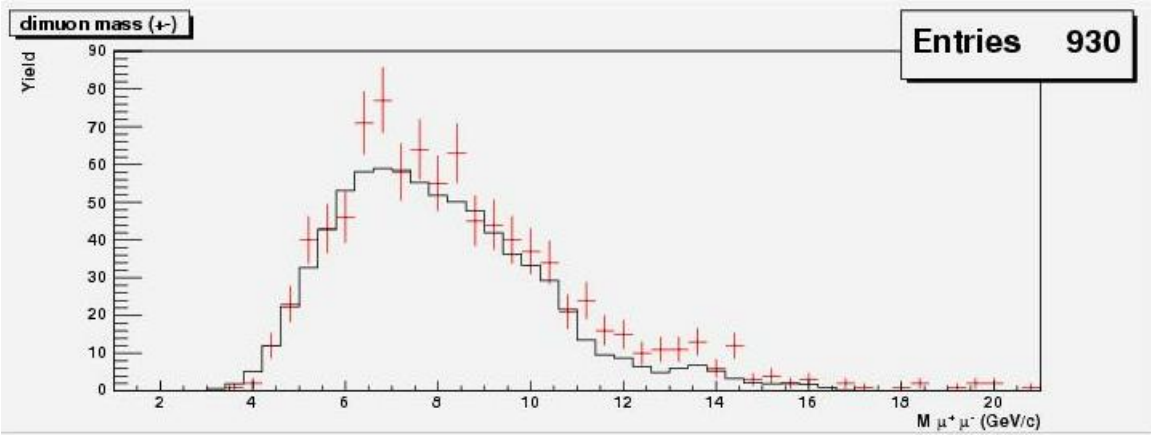

Figure 20 - Dimuon mass spectrum in dAu collisions for one muon at positive and one muon at negative rapidity, showing the large combinatoric background from random muon pairs (black) that dominates the $\mu^+\mu^-$ spectrum (red points with error bars) starting a little below 5 GeV in mass. The ϒ (unobserved) would appear as a peak at 9.46 GeV.

Finally, the ψ' is also an important signal in dAu collisions. Although it has a smaller yield (~few %) compared with the J/ψ and is therefore harder to measure, its physics is cleaner since it does not suffer from the large feed-down from higher mass resonance decays that the J/ψ does (~40% of J/ψ s come from decays of higher mass resonances). Its physics should also be different from the J/ψ since it is a larger and more weakly bound object, and so should see larger absorption, at least after it has hadronized.

In current measurements of the dimuon mass spectra, the large combinatoric backgrounds from hadron decays also make it very difficult to identify and extract the ψ' yield, as shown in Figure 21. Here again, the elimination of these muons from hadron decay can reduce the background and the improved J/ψ and ψ' mass resolutions should make it much easier to extract a clear ψ' signal.

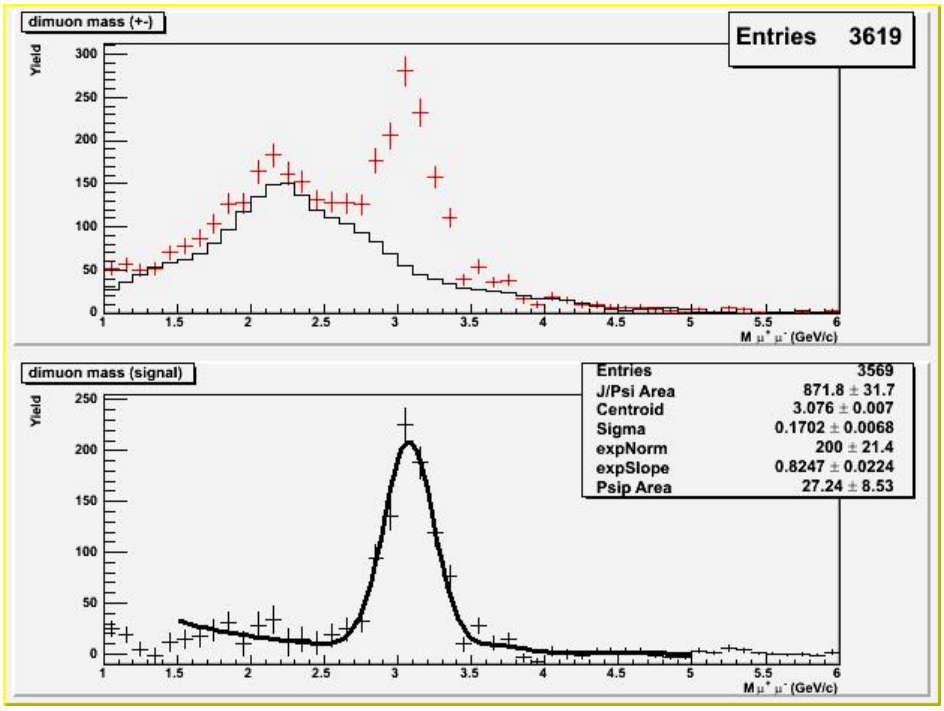

Figure 21 - The PHENIX 2003 dAu dimuon mass spectrum (top panel) with the combinatoric background shown in black and the total $\mu^+\mu^-$ pairs in red; and (bottom panel) the spectrum with the background subtracted where a hint of the ψ' peak (at 3.7 GeV) has been fit. The ψ' is not well determined, due to the statistical uncertainty contributed by the subtraction and the poor mass resolution (~170 MeV).

2.2.3 Heavy-quarks: Charm and Beauty Mesons

The most compelling physics issues that can be studied using single heavy quarks are:

- Gluon shadowing or saturation effects for single heavy quarks. To be contrasted with similar studies of quarkonia where initial state effects are the same but final state effects are different and more important.
- Energy loss of heavy versus light quarks in cold nuclear matter and multiple scattering (Cronin effect), the latter especially at backward rapidity where the heavy quarks are nearer the nucleus in rapidity.
- Accurate heavy-quark cross sections over large rapidity and p_T ranges in order to constrain recombination models for quarkonia ($c\bar{c}$ or $b\bar{b}$ bound states).

As already discussed above, measurements of single heavy quarks (charm and beauty) are sensitive to the gluon distributions and their modification (shadowing) in nuclei. They provide a complementary view to that provided by studies of quarkonia as they involve the same initial-state gluon distributions but have quite different, and probably simpler, final-state effects than those of the J/ψ. For example both quarkonia and single heavy quarks can experience energy loss and multiple scattering in the final state, while

quarkonia also have large effects from absorption (i.e. disassociation of the two heavy quarks that would otherwise form the heavy quark-antiquark bound state).

Energy loss of partons in the initial state is thought to have a small effect at RHIC, since the energy loss per unit length (fm) in most models is thought to be approximately constant and small compared to the initial-state parton momenta at RHIC. On the other hand, partons in the final state could show some effects of energy loss since their momentum are lower, while heavy-quarks are expected to lose less energy than light quarks due to the dead-cone effect[xxxiv]. These issues are very important in the high-density regions created in heavy-ion collisions, but we also need a baseline for normal nuclear densities from proton-nucleus collisions.

Another general feature of most produced particles comes from the multiple scattering of initial-state partons, which causes a broadening of the transverse momentum (Cronin effect) of the produced particles. Final-state multiple scattering can further broaden the transverse momenta.

A recent result for the p_T dependence of the nuclear modification factor for prompt muons is shown in Figure 22 from PHENIX[xxxv]. Data for prompt muons at forward ("North") and backward ("South") rapidities in dAu collisions show a suppression at forward rapidities (small *x* values) in Au where one would expect shadowing effects. At backward rapidities an enhancement that increases with p_T is observed which could be due to initial-state multiple scattering effects, but this data is in the anti-shadowing region where an enhancement that balances the depletion of the gluons at smaller x could occur.

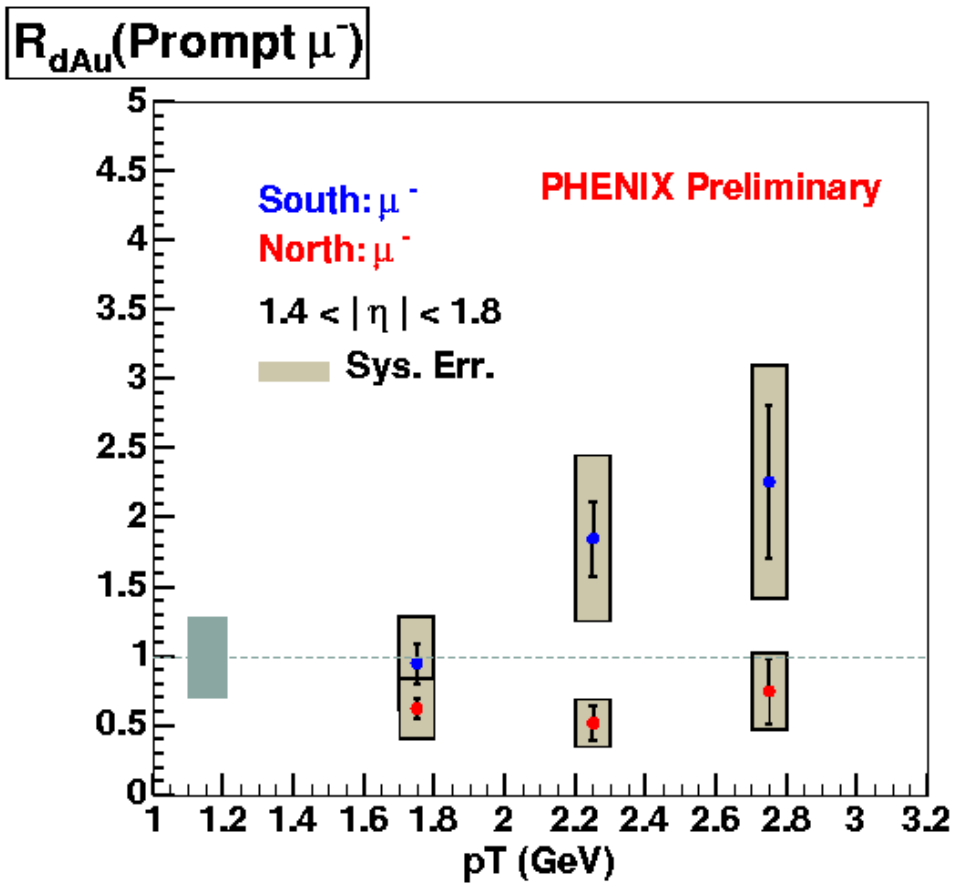

Figure 22 - Nuclear modification factor in dAu collisions, R_{dAu}, for prompt muons in the forward and backward rapdity regions versus p_T. The prompt muons are primarily from the decays of charm and beauty mesons although perhaps 10% are from other processes such as light meson decays.

These results are obtained through a statistical method where the vertex distribution for the events contributing to the single muons is studied and a component that matches the raw vertex distribution is determined after subtracting another component that follows the decay distribution expected for light meson decays. For example, the light mesons which originate from a vertex that is farther from the spectrometer in z will have more probability of decay and therefore will be more numerous. This statistical method suffers from substantial systematic effects that are probably more than 20-30% even at much larger integrated luminosity. With the FVTX upgrade these events can be separated on an event-by-event basis and a much more robust and accurate heavy-quark semi-leptonic decay spectrum can be obtained. This will also allow measurements at smaller p_T values by substantially reducing the low-mass meson decay backgrounds.

In contrast to the conventional expectation, Vitev et al. have shown in their theoretical approach[xxxvi] that gluon fusion is not the dominant process for production of open charm. In his model "flavor creation" diagrams, $cg \rightarrow cg$ and $cq \rightarrow cq$, dominate the production,

rather than gluon fusion, $gg \to c\bar{c}$. The relative contribution of these different processes is shown in Figure 23 vs transverse momentum at several different rapidities.

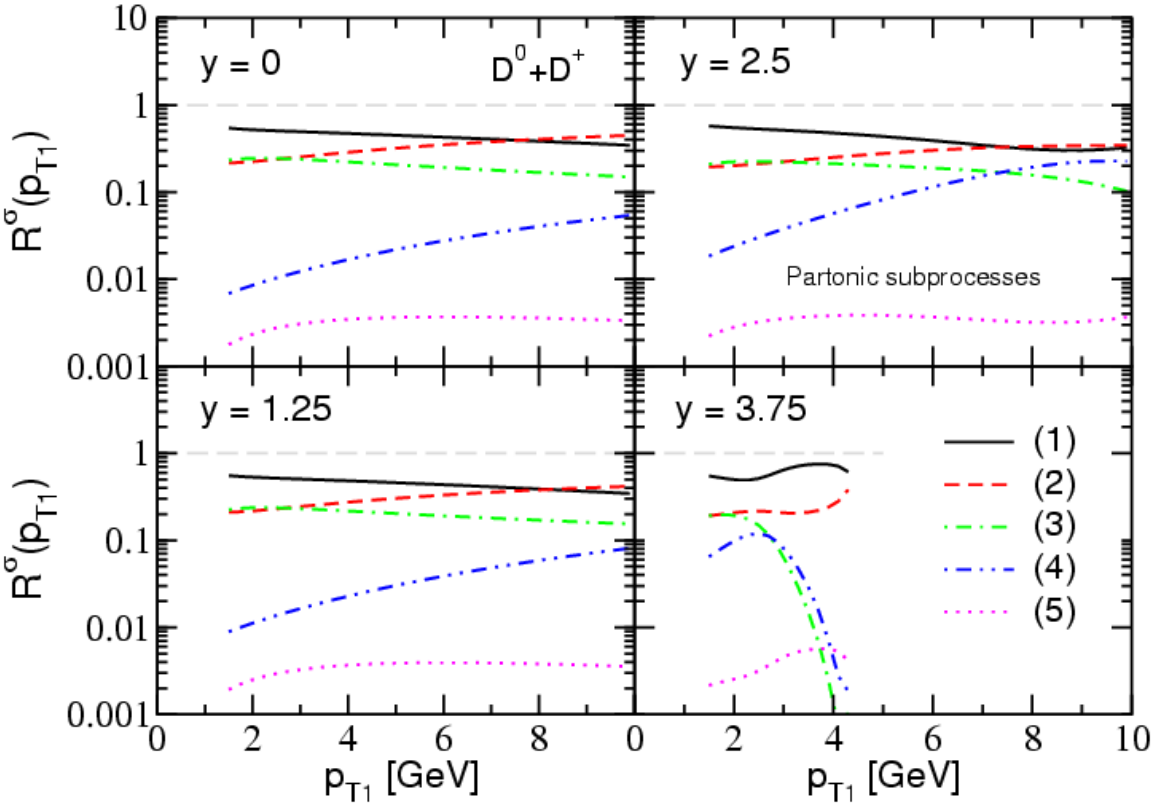

Figure 23 – Vitev's calculations[xxxvi] show that gluon fusion is not the dominant process in open charm production at RHIC energies. Here he shows the fraction of the total cross section contributed by each process vs p_T for different rapidity values for the processes (1) $cg \to cg$, (2) $cq \to cq$ (where q is a light quark or anti-quark), (3) $gg \to c\bar{c}$, (4) $q\bar{q} \to c\bar{c}$ and (5) $c\bar{c} \to c\bar{c}$ (intrinsic charm).

2.2.4 Hadrons at Forward and Backward Rapidity

Light hadrons (π and K) can also be measured at forward and backward angles by the PHENIX muon arms using their decays into muons or by identifying those hadrons that "punch through" all layers of the muon identifier at the rear of the muon arms. These punch-through hadrons contribute roughly 10% of the 2 GeV particles that are seen several layers deep in the muon identifier. Using the same statistical techniques described previously in section 2.2.3, the yield of decay muons is determined. Nuclear modification factors for light mesons (via their decay to muons) for dAu collisions from PHENIX are shown for positive and negative rapidity in Figure 24. Similar to the prompt results shown earlier, these particles also exhibit suppression at forward rapidities and enhancement at backward rapidities.

Hadron production at forward rapidity, like the heavy-quarks discussed earlier, is also sensitive to the gluon structure function and its modification in nuclei, e.g. shadowing.

However, whether these hadron measurements actually probe small momentum fractions that lie well within the shadowing region is unclear, as some theoretical calculations indicate that unless one measures two hadrons in the forward direction one does not actually sample small enough x values to see shadowing[xxxvii]. In any case, the clean measurements possible with the FVTX will help resolve this question.

It is also important to study the modification of jets in the forward and backward directions for dAu, both to understand the fragmentation and how it is modified in cold nuclear matter. Jet data will also provide a baseline for similar studies in nucleus-nucleus collisions where jets are one of our most important tools for studying the properties of the hot-dense matter (QGP) created in those collisions.

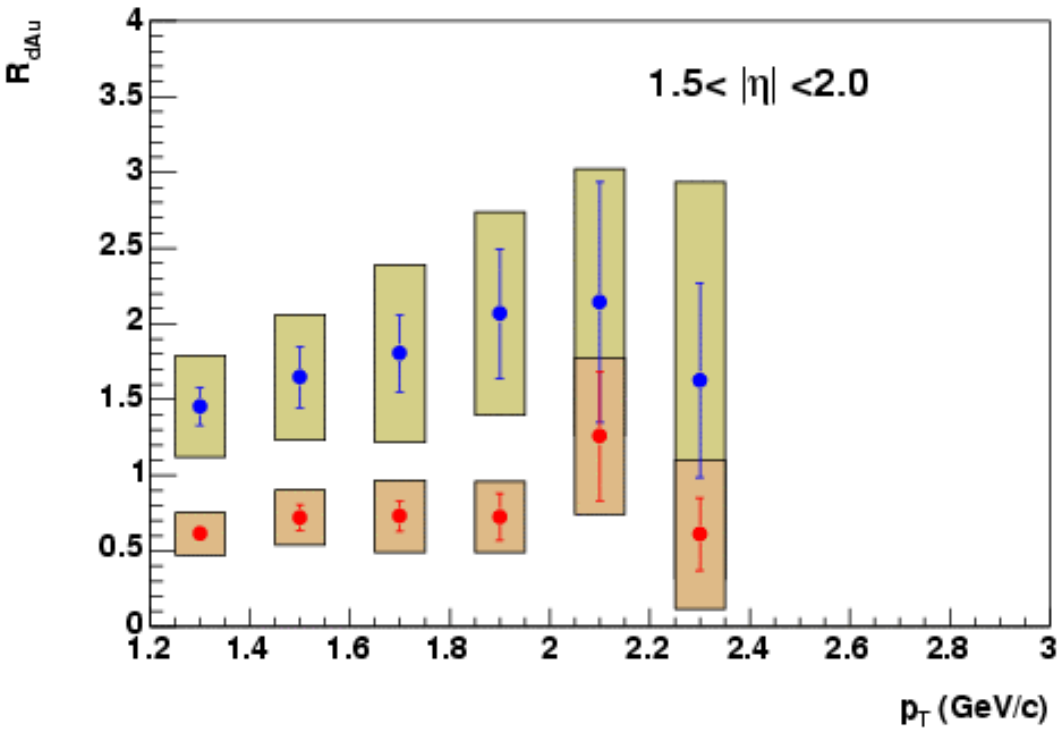

Figure 24 - Nuclear modification factor in dAu collisions (RdAu) for hadrons decaying into muons in the forward (red) and backward (blue) rapidity directions (PHENIX Preliminary).

Like the prompt muons discussed earlier, this method of measuring hadrons suffers from large systematic errors due to the statistical method used to separate prompt particles from light hadron decays. With the FVTX we will be able to cleanly separate the prompt component from that due to the decaying hadrons. This will allow direct identification of the light hadrons, especially at larger p_T where the heavy-quark decays would normally start to dominate, and produce a cleaner result with much smaller systematics. In addition, the FVTX can provide an independent sample of punch-through hadrons that can also be used to measure the forward and backward hadron spectra.

The ratio of yields in central versus peripheral dAu collisions is shown versus rapidity in Figure 25. Data for light hadrons and for the J/ψ show a surprisingly similar trend, with suppression at forward rapidity and enhancement at backward rapidity. The FVTX will provide reduced systematic errors for all of the measurements at |y|>0.

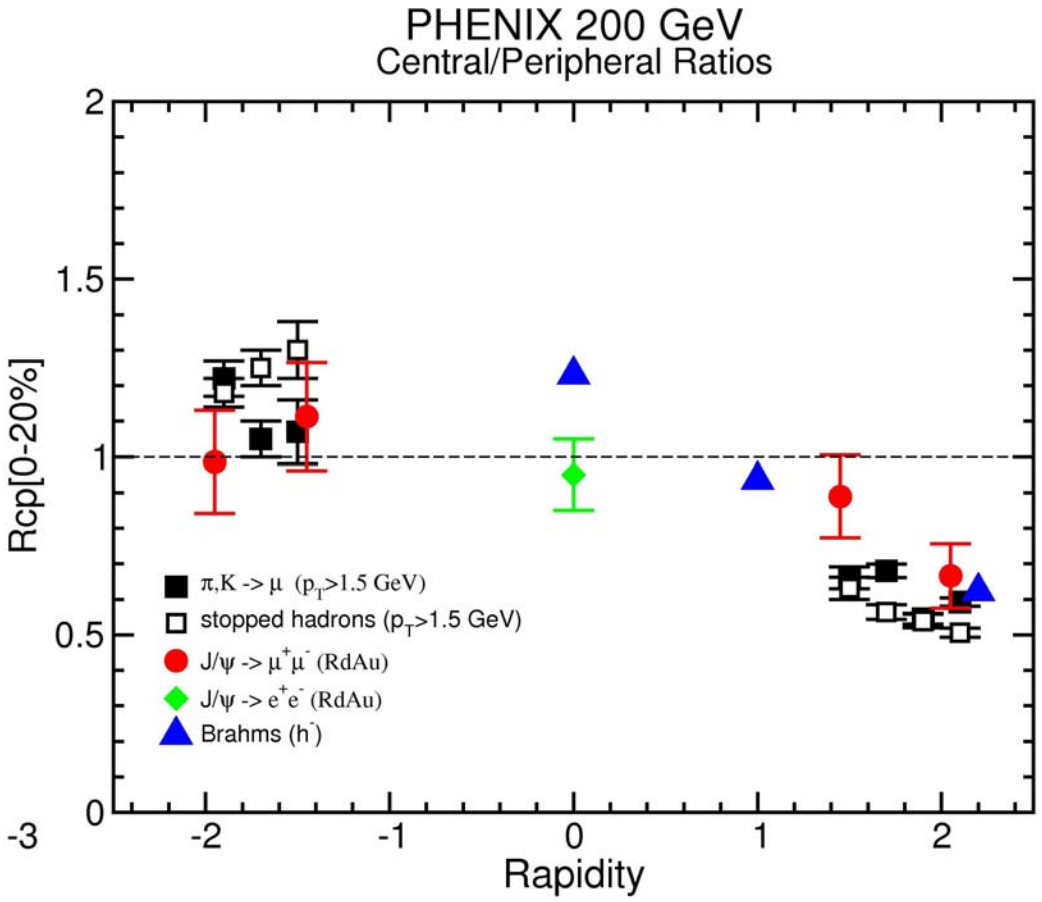

Figure 25 – Nuclear modification in dAu collisions in terms of the ratio between central and peripheral collision yields, Rcp, for light hadrons that decay into muons from PHENIX, compared to similar results from Brahms and to PHENIX data for the J/ψ.

Again, a different picture is provided by Vitev et al.[xxxvi], where the most important effect in the increasing suppression at large rapidity comes from energy loss in the initial state. In these calculations as shown in Figure 26, a rapidity shift of Δy=0.25 provides a phenomenological energy loss, and gives suppressions very similar to both the hadron and charm data. These calculations do not include initial-state p_T broadening (Cronin effect) which would alter the comparison of the calculation to the data somewhat, but probably not change it too much.

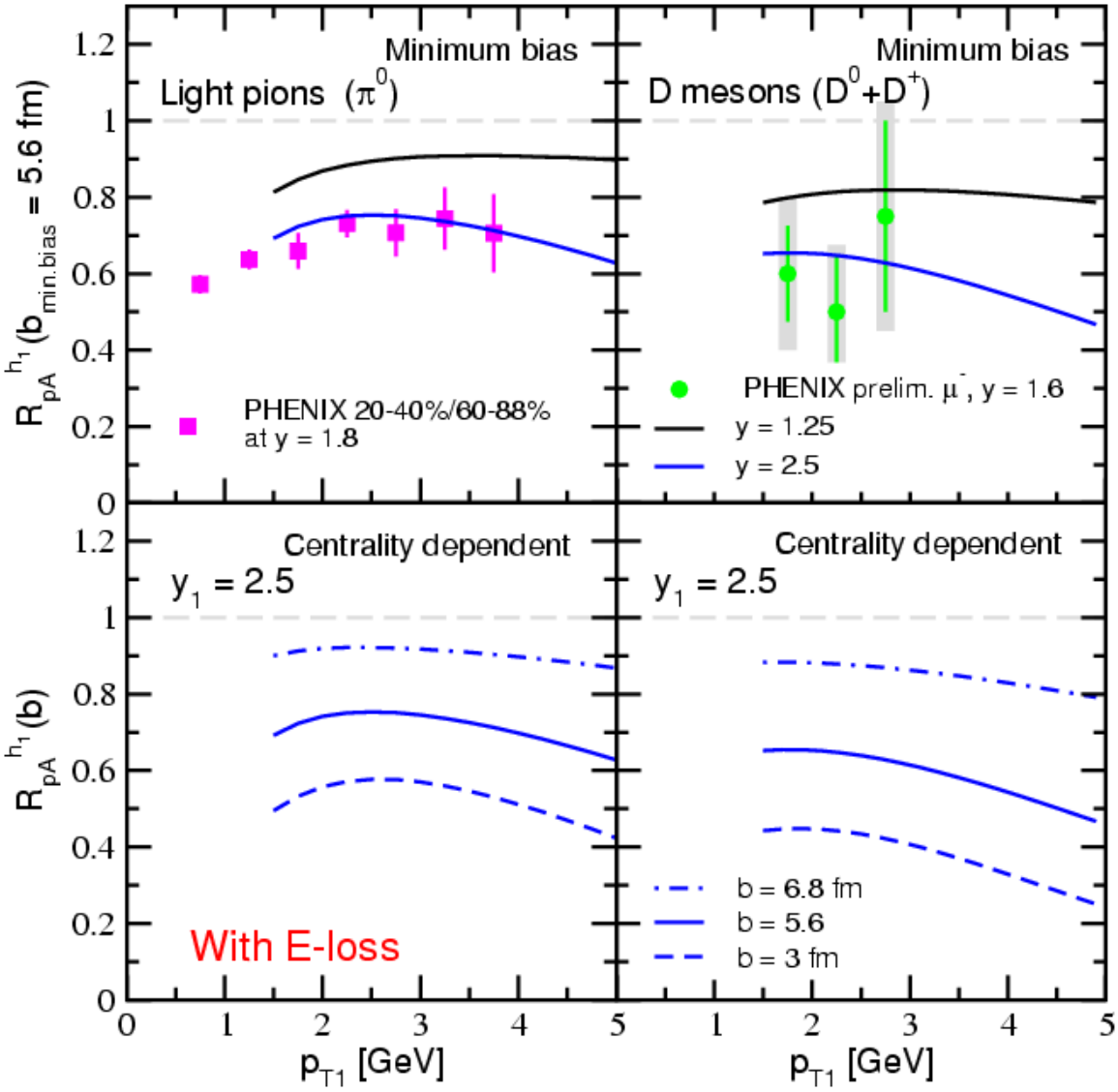

Figure 26 – Calculations from Vitev[xxxvi] showing top: Suppression of the single inclusive hadron production rates in d+Au collisions versus p_T for rapidities y_1 = 1.25 and 2.5. Bottom: Impact parameter dependence of the calculated nuclear modification for central, b=3 fm, minimum bias, $b_{min\ bias}$ = 5.6 fm and peripheral, b=6.9 fm, collisions.

One should also note that the model of Kopeliovich[xxvi], which includes Sudakov suppression, provides a somewhat universal explanation for increasing suppressions at forward rapidity as well. As an example we show these calculations compared to the Brahms forward π^- suppression ratios in Figure 27.

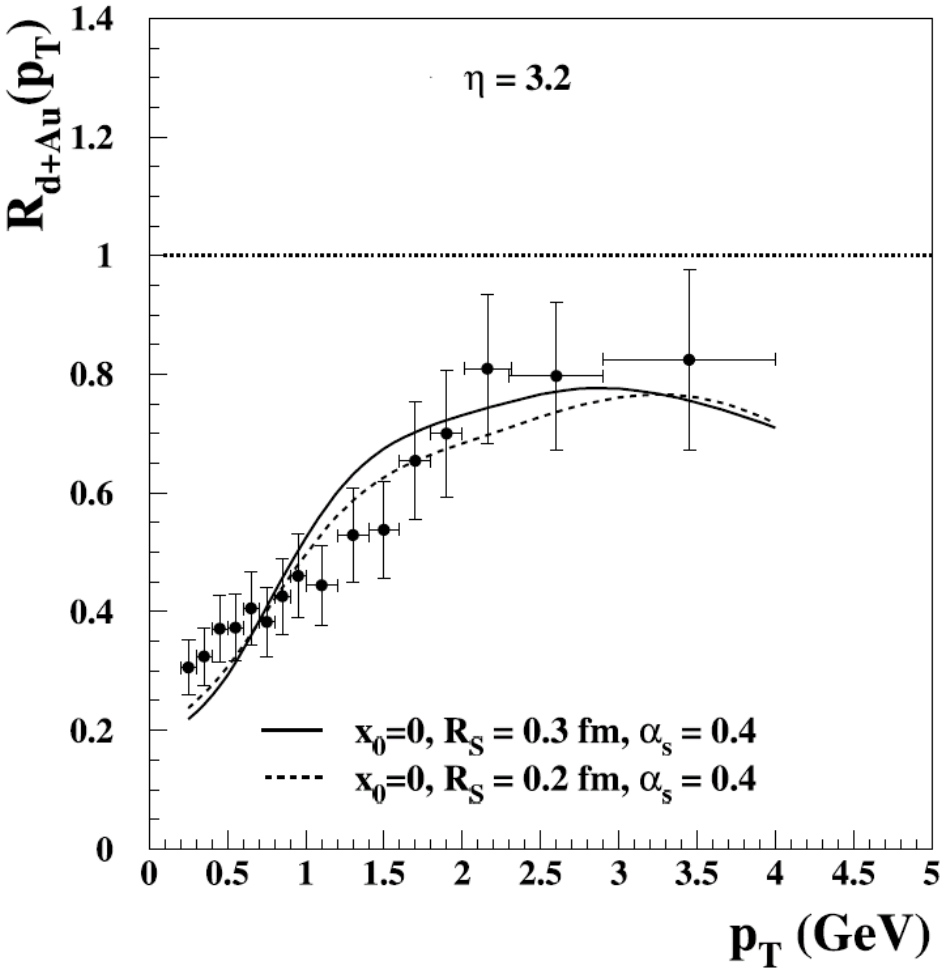

Figure 27 – Calculations from Kopeliovich[xxvi]. Ratio of negative particle production rates in d+Au and pp collisions as a function of p_T. Data are from Ref. [xxxviii], solid and dashed curves correspond to calculations with the diquark size 0.3 fm and 0.4 fm respectively.

2.2.5 Drell-Yan Measurements

Drell-Yan events, which provide a direct measure of the anti-quark distributions in nucleons or nuclei, have always been limited in the past in their reach to low *x* by the inability to separate the Drell-Yan muon pairs below the J/ψ mass from copious pairs due to open-charm decays. For example, as shown in Figure 28, the FNAL E866 Drell-Yan data was limited to masses above 4 GeV, due to a large contribution of randoms (charm decays) at lower masses.

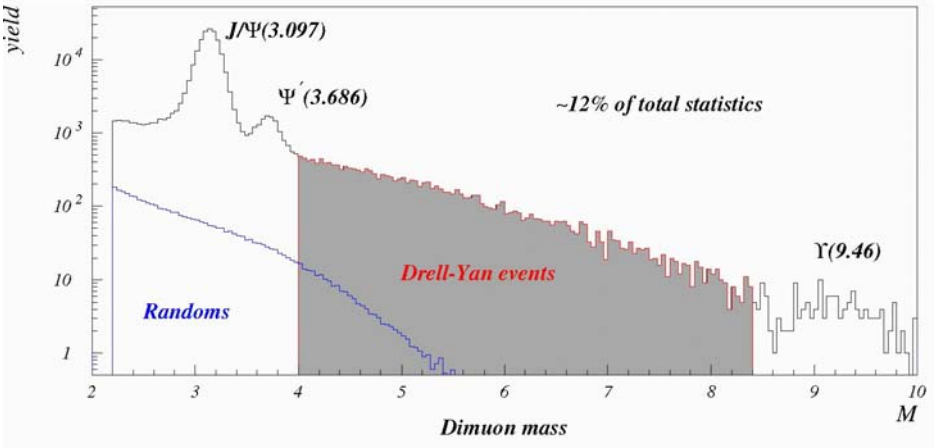

Figure 28 - Dimuon mass spectrum from E866/NuSea, showing the Drell-Yan mass region used in their analysis, which excluded masses below 4 GeV. Lower masses were excluded because of the large backgrounds from open charm decays (labeled Randoms) in that region.

On the other hand, PHENIX, with the addition of the FVTX, should be able to identify and quantify the portion of the low mass dimuon continuum from charm decays and also remove the large numbers of random pairs from light hadron decays which are present at RHIC energies. This should allow Drell-Yan measurements over a broad mass range including values below the J/ψ, therefore spanning a large range of x with values well into the shadowing region. Since the relative Drell-Yan rates at RHIC are small, such measurements will still be a challenge, but with RHIC-II luminosities such measurements have the potential to provide information on the anti-quark distributions at much smaller values of *x* than are currently accessible. At the same time, one would also learn more about charm production and the correlation of the charm pairs through the decay pairs found in the continuum.

2.2.6 Summary of Physics Addressed by the FVTX in d(p)-A Collisions

In summary, the silicon forward vertex micro-vertex detector, which covers the PHENIX central arm mid-rapidity range ($1.2 < |y| < 2.2$), addresses the following physics in dA reactions:

- Probing the small-x shadowing or gluon saturation region in nuclei through the production of single heavy quarks (c and b) and of bound states of heavy quarks (J/ψ, ψ' and Υ), and providing a gluon structure function measurement in the small-x region for cold nuclear matter.
- Disentangling various nuclear effects on J/ψ production by contrasting it with open charm production at large positive and negative rapidity. These should share the

same initial-state effects and have similar production mechanisms; but will have different final-state effects.

- Comparison of light and heavy-quark p_T distribution to determine differences in energy loss and Cronin effects.
- Measurements of light hadrons via their decays to muons or when they punch through the muon absorbers, in contrast with heavy quarks in the same kinematical regions.
- Beauty cross sections as a constraint on the contributions of $B \to J/\psi$ to J/ψ production.
- Robust measurements of the energy loss and flow of charm (and beauty) quarks in cold nuclear matter using high-p_T single muons.
- Accurate measurement of the nuclear dependence of the charm cross section to provide a solid cold nuclear matter baseline for recombination effects in J/ψ production from nucleus-nucleus collisions.
- Improved separation of the ψ' from the J/ψ, leading to the first ψ' data from RHIC.
- Low-mass muon pairs and Drell-Yan measurements of anti-quark shadowing at small *x* values.
- ϒ and Drell-Yan measurements at mid-rapidity using one muon in each arm after removing the copious random pair backgrounds from light hadron decays.

2.3 Polarized Proton Collisions, and the Gluon and Sea Quark Spin Structure of the Nucleon

Understanding the substructure of the nucleon (protons and neutrons) is of fundamental interest in nuclear and particle physics. The strong nuclear interaction observed between nucleons inside a nucleus is a residual "van-der-Waals" force arising from a more fundamental interaction, Quantum Chromodynamics, between the nucleon's partonic constituents, namely the quarks and gluons. Studying the partonic distributions inside the nucleon can shed light on why and how quarks and gluons are confined inside hadrons.

The striking results, first from the EMC experiment at CERN and then from subsequent experiments at SLAC, DESY, and Jefferson Lab, showed that the total spin of the quarks does not account for the total spin of the proton. These deep-inelastic scattering (DIS) experiments have established that only 10-30% of the proton spin is carried by the quarks and anti-quarks. The rest of the spin must come from the gluon spin and the parton orbital angular momentum. Figure 29 shows the AAC collaboration analysis of the polarized parton distributions for quarks and gluons. SU(3) flavor symmetry is assumed in the analysis, and for sea quarks it is assumed that $\Delta\bar{u} = \Delta\bar{d} = \Delta\bar{s}$. The sea quark polarization is poorly constrained and gluon polarization is virtually unknown, with the present set of data.

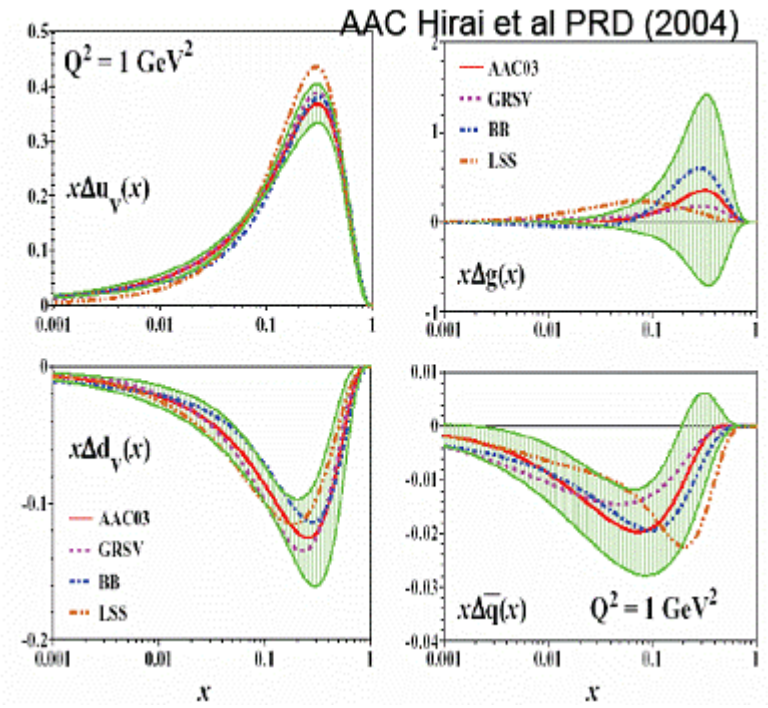

Figure 29 - Global polarized quark and gluon distributions from AAC collaboration. The red line is the result of their fit, and the green band is the total uncertainty with respect to the red line. The other colored lines are alternative parameterizations of these distributions.

The PHENIX spin program aims to measure the gluon spin structure function in the proton. The existing PHENIX capability to do so is shown in Figure 30 as the blue bars. However, precision measurements for heavy quarks with the separation of charm and beauty are only possible with the addition of a precision vertex tracking detector. The green bars in Figure 30 display the additional capability supplied by the barrel VTX detector. However, there are significant gaps in this x-range that will make it difficult to fully address the spin issue. The Si Endcap Vertex Detector (FVTX) proposed here extends the coverage (red bars in Figure 30) to the lowest and highest x-values, $0.001 < x < 0.3$, as well as providing significant regions where multiple channels overlap. These overlaps will provide vital cross-checks that will improve the reliability of global fits to the spin structure functions.

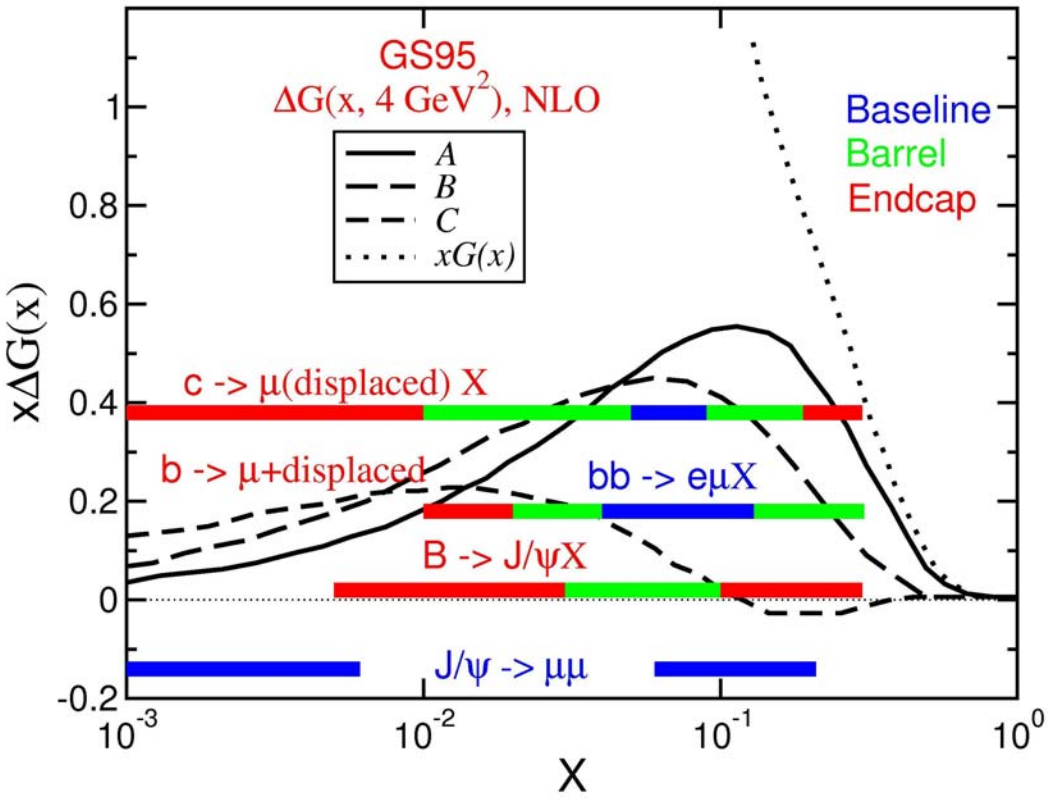

Figure 30 - Expected *x*-range for different channels used to extract the gluon spin structure function. The blue bars indicate PHENIX's existing capability, green bars are for the Barrel upgrade, while the red bars indicate the additional coverage provided by the proposed Endcap vertex upgrade. The curves show various estimates of the expected gluon polarization[xxxix].

2.3.1 The Role of the Silicon Vertex Detector

The Endcap Vertex Detector provides tremendous improvements in *x*-range over a Barrel-only detector, as shown in Figure 30. It also provides a model independent clean separation of light hadron, charm and beauty production. The following detailed list of improvements has been produced by simulating *pp* collisions with PYTHIA and requiring sufficient counts in each exit channel to be able to make a reasonable measurement.

- $c\bar{c}$ production via gluon fusion. The *x*-range is extended considerably down to $x = 0.001$, using $D \to \mu X$, with a displaced muon from charm decay.
- $b\bar{b}$ production via gluon fusion. With the upgrade we can identify displaced J/ψ from $B \to J/\psi$ decay. This provides coverage for $0.005 < x < 0.3$. The selection of semi-leptonic decays $b\bar{b} \to e\mu X$ at high momentum is improved using displaced vertices. This extends the x_{gluon} coverage for these

semi-leptonic decays to 0.01–0.3. Measurement of $B \rightarrow \mu X$ is also possible by placing a cut on the p_T of the muon.

- Background suppression for W physics events. The main background for a W measurement with single muons is muons from heavy flavor decay and light hadron decay and/or punch-through. The heavy flavor background can be identified and rejected based on displaced vertices. The light hadron background can be suppressed with an isolation cut; in general, a muon from a W decay is isolated from jet activity, while a light hadron normally has associated jet particles around it. This could also extend W physics to a broader kinematic coverage by measuring low p_T muons from W decays.

2.3.2 Polarized Gluon Distribution and Heavy Quark Production

Most of our current knowledge of the nucleon spin comes from Deep Inelastic Scattering (DIS) experiments. To first order in DIS, however, an incoming lepton only couples to the charged quarks or anti-quarks, and not to the neutral gluons. To get around this difficulty, one may use measured (polarized) quark and anti-quark distributions to derive the (polarized) gluon distribution via QCD-evolution equations over a sufficiently large range of x and Q^2 – but these data are not available. On the experimental side, semi-inclusive DIS experiments (SMC, HERMES, COMPASS) explore higher order processes, such as di-hadron production, to measure the polarized gluon distributions, as is illustrated in Figure 31. However, current results are limited by statistics and theoretical uncertainties.

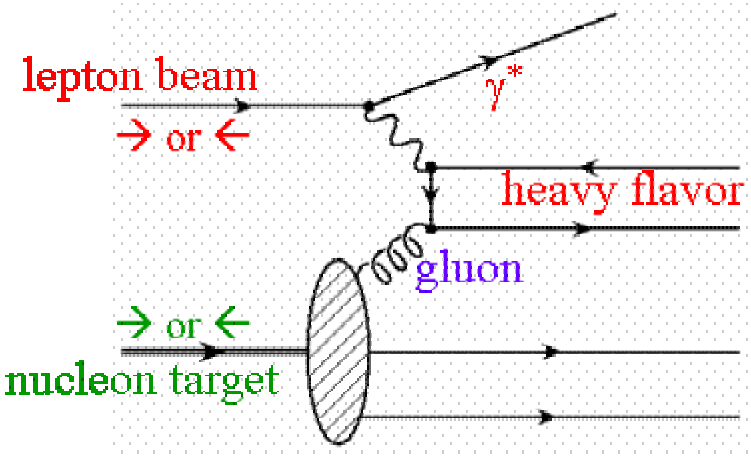

Figure 31 - Higher order semi-inclusive DIS is used to explore gluon distribution.

The RHIC-SPIN program provides a new tool to directly collide (polarized) quarks and gluons at leading order at high energy (see Figure 32) and as such PHENIX has a major goal of measuring the gluon spin-structure function in protons. In the PHENIX experiment,

we will measure the polarized gluon distribution $\frac{\Delta G(x)}{G(x)}$ using many different processes. Experimentally we measure the double spin asymmetry:

$$A_{LL}^{H} = \frac{\sigma^{++} - \sigma^{+-}}{\sigma^{++} + \sigma^{+-}} \sim \frac{\Delta f(x_1)}{f(x_1)} \otimes \frac{\Delta f(x_2)}{f(x_2)} a_{LL}(x_1 + x_2 \to H + X)$$

where $\frac{\Delta f(x_1)}{f(x_1)}$ and $\frac{\Delta f(x_2)}{f(x_2)}$ are the polarized parton distributions for parton (x_1) and (x_2), and H is the final state particle detected by the PHENIX detector. The polarized parton distributions can be derived from the experimentally measured asymmetry once we know the partonic asymmetry $a_{LL}(x_1 + x_2 \to H + X)$ which is normally calculated within the framework of pQCD.

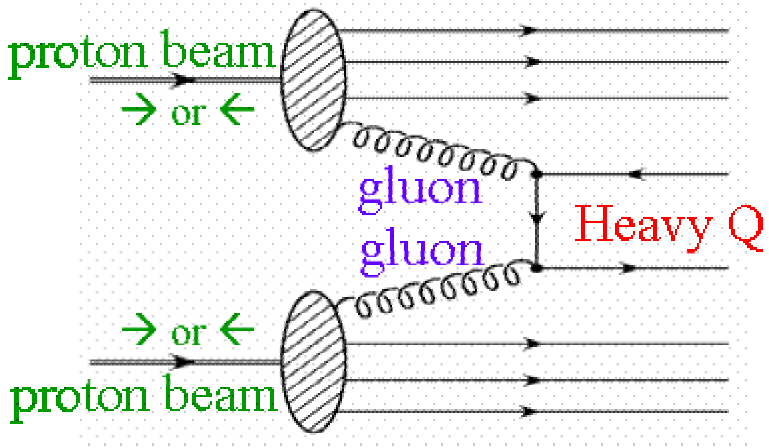

Figure 32 - At RHIC-SPIN, quarks and gluons interact directly at leading order.

A partial list of basic partonic processes relevant to this proposal:

1. Inclusive open charm and open beauty production (into heavy mesons "*Q*") followed by decay to single muons;

$$gg, gq, qq \to Q + X$$
$$\downarrow$$
$$Q \to \mu^{+/-} + X$$

2. Open beauty production (into heavy mesons, usually *B*) followed by decay to *J*/ψ, resulting in a displaced muon pair from *J*/ψ decay;

$$gg,gq,qq \rightarrow B + X$$
$$\downarrow$$
$$B \rightarrow J/\psi + X$$
$$\downarrow$$
$$J/\psi \rightarrow \mu^+\mu^-$$

3. Inclusive light hadron production (pions and kaons) followed by a continuous distribution of in-flight decay, resulting in either displaced single muons (one extreme) or hadron punch-through to the muon identifier (the other extreme);

$$gg,gq,qq \rightarrow \pi^{+/-}/K^{+/-} + X$$
$$\downarrow$$
$$\pi^{+/-}/K^{+/-} \rightarrow \mu^{+/-} + X \quad \text{(maybe)}$$

4. Heavy quarkonium production, producing muon pairs at the original event vertex.

$$gg,qq \rightarrow J/\psi + X$$
$$\downarrow$$
$$J/\psi \rightarrow \mu^+\mu^-$$

It is important to note that at RHIC energy, heavy flavor production is dominated by gluon-gluon interactions, thus we have,

$$A_{LL}^{Q\overline{Q}} = \frac{\sigma^{++} - \sigma^{+-}}{\sigma^{++} + \sigma^{+-}} \sim \frac{\Delta G(x_1)}{G(x_1)} \otimes \frac{\Delta G(x_2)}{G(x_2)} a_{LL}(x_1 + x_2 \rightarrow Q\overline{Q} + X)$$

However, in reality, one always faces various backgrounds in the measurement, so the measured signal asymmetry is diluted,

$$A_{LL}^{Q\overline{Q}} = \frac{A_{LL}^{incl} - r \cdot A_{LL}^{BG}}{1 - r}$$
$$\delta A_{LL}^{Q\overline{Q}} = \frac{\sqrt{(\delta A_{LL}^{incl})^2 + r^2 \cdot (\delta A_{LL}^{BG})^2}}{1 - r}$$

where $r = \frac{N^{BG}}{N^{Q\overline{Q}} + N^{BG}}$ is the background fraction, A_{LL}^{incl} and A_{LL}^{BG} are the asymmetries of the inclusive signal and background, respectively. Normally the background asymmetry itself is not well known, so it is very important to minimize the background fraction. The proposed Forward Silicon Vertex detector will significantly improve the purity of the

signals both for the light hadron and heavy quark measurements by permitting an additional cut on displaced vertex information.

2.3.2.1 Measurements of Open Heavy Quark Production

Figure 33 shows the preliminary result of open heavy flavor production with muons from 2002 *pp* data at RHIC. The prompt muons are mostly from open charm decay in the measured p_T range. It is clear from Figure 33 that non-prompt muon backgrounds dominate at most of the low p_T region where we have the maximum statistics in the experiment. Without the proposed vertex detector, it is very hard to do precision measurements of asymmetries with prompt muons from open heavy quark (charm and beauty) decay.

As discussed above, we plan to observe open charm production though semi-leptonic decay to muons. The proposed FVTX will allow us to reject muons from light hadron decays as well as misidentified prompt punch-through hadrons based on the secondary vertex distributions. However, at high p_T, the open charm production measurement is limited by beauty production contamination.

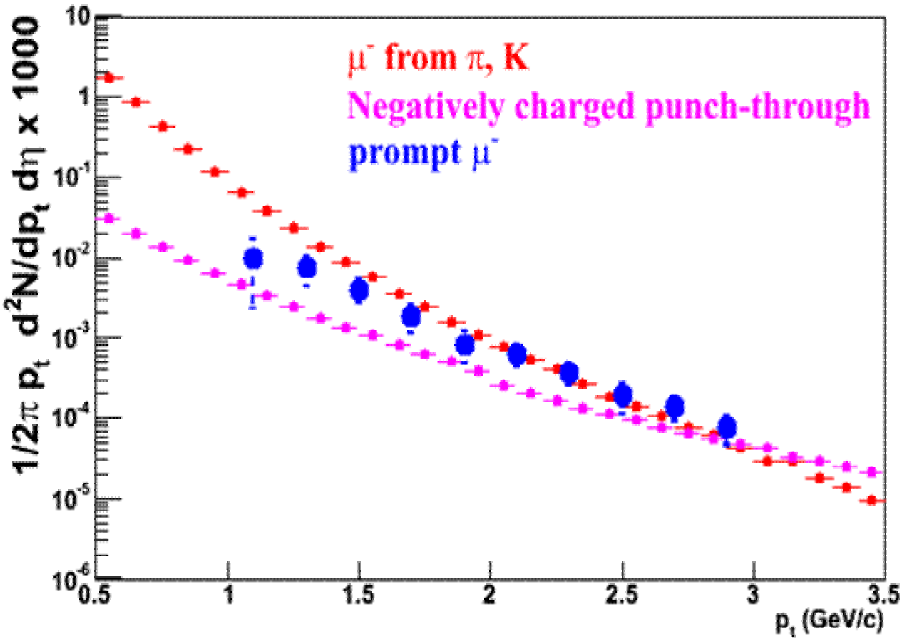

Figure 33 - PHENIX preliminary results (blue points) for prompt single muons (mostly from open charm decay) measurement from run2 pp data. Two sources of background are shown.

Measurements of beauty production can be performed in the present PHENIX detector using electron-muon coincidence with central and forward spectrometers. However, such measurements are limited to a narrow kinematics range. This limitation can be overcome by

direct measurements of open beauty production with the vertex detectors. As discussed in an earlier chapter (2.2.2), by identifying displaced J/ψ dimuons from open beauty decay, we can achieve a very pure open beauty event sample with a good acceptance. This will provide a very important cross check for the gluon polarization measurement with open charm.

Another important physics topic is to study the beauty production mechanism. Beauty production was measured at the Tevatron at 1.8 TeV, and the next-to-leading order pQCD calculation underestimated the data by a factor of 2 or greater. The discrepancy between the experimental data and the theory has sparked much debate and excitement recently, including possible hints of new physics beyond the standard model. New data from polarized *pp* collisions at RHIC will provide crucial information on the beauty production mechanism, and also possibly point to new physics.

Figure 34 shows projected experimental sensitivities of double spin asymmetry measurements if we can identify prompt muons from open charm and open beauty decay.

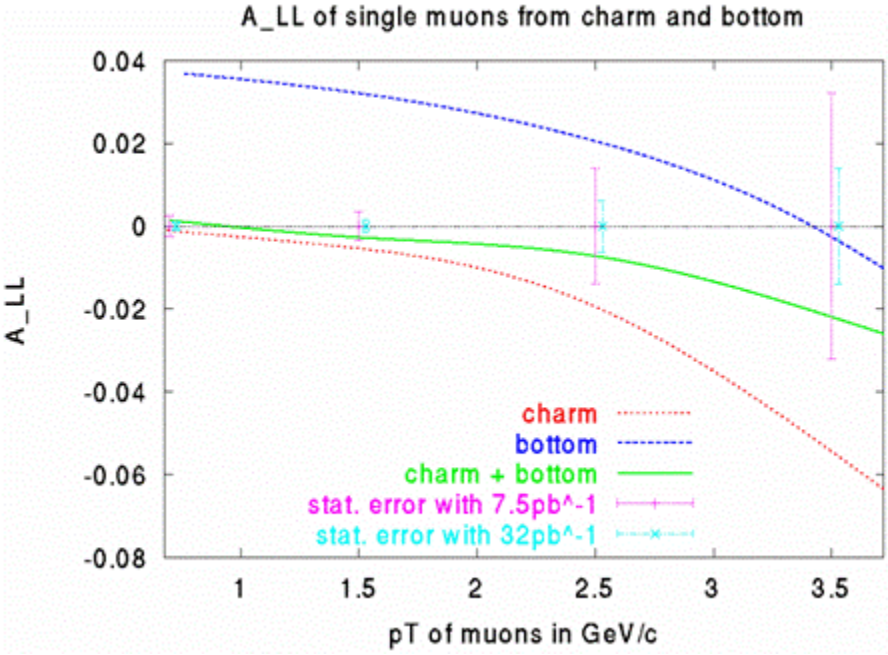

Figure 34 – Expected size of double-spin asymmetries (lines) in the observation of single muons from open charm and bottom production. The projected uncertainties (points with error bars) are shown for a few values of p_T.

2.3.2.2 Measurement of Light Hadron Production with the Muon Spectrometers

There is copious production of light hadrons at RHIC. Figure 35 shows the muon p_T spectra with different origins in 200 GeV *pp* collisions, where it is seen that muons from light

charged hadron decay dominate at low p_T < 3 GeV. Using recently developed analysis techniques, we can measure inclusive light hadron production with the muon spectrometer, using event vertex and muon penetration depth analysis to statistically establish the hadron and muon event rates. This method was used in the dAu analysis and is being used now for the 2005 *pp* data analysis of spin asymmetries. The proposed forward silicon vertex detector will enable us to identify muons from light hadron decay on an event-by-event basis, as they tend to have large vertex separations of order of few mm or greater. Furthermore, these light hadrons are dominantly produced through *gg* and *gq* scattering at low p_T, see Figure 36. Such samples can be used to explore gluon polarization since they have good statistics and also cover a wide range of momentum fraction *x*. Figure 37 shows the double spin asymmetry with charged pions in the PHENIX muon spectrometer acceptance.

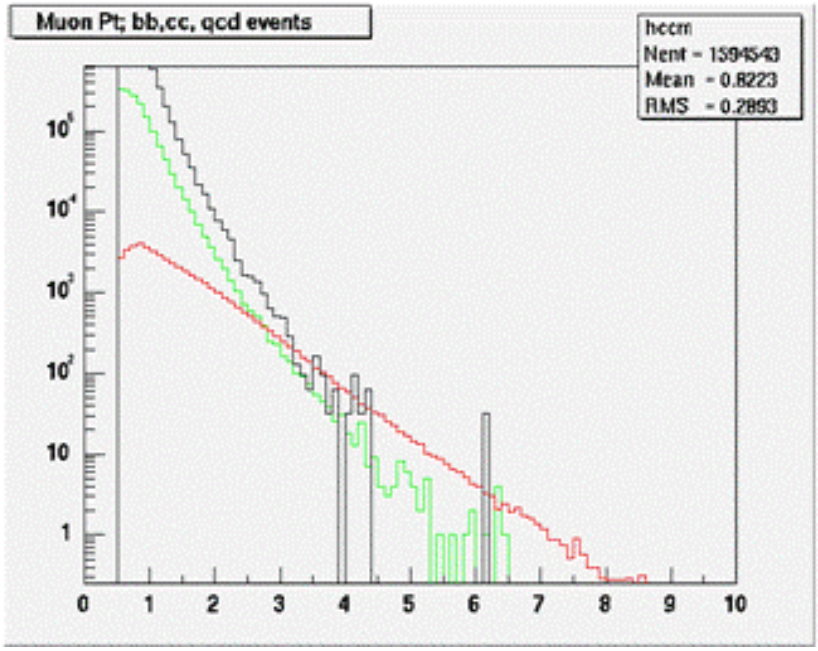

Figure 35 - Muon p_T spectra with different origins from Pythia simulation, as a function of p_T [GeV]. Muons from light charged hadron decays (black); from open charm (green); from open beauty (red).

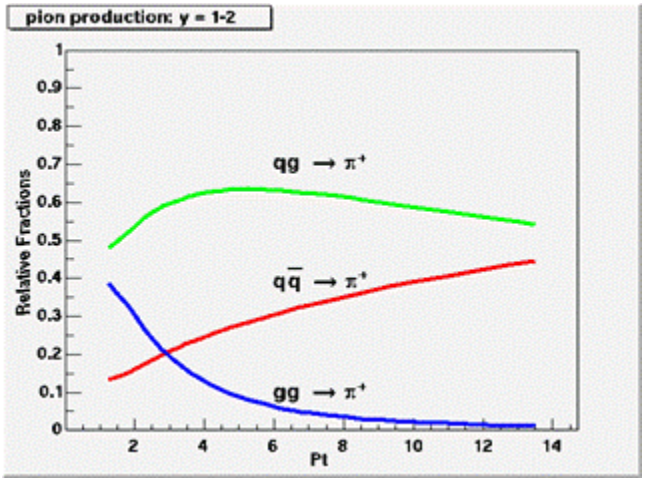

Figure 36 - Partonic origin of charged pions produced within the acceptance of muon spectrometer in pp collisions at $\sqrt{s}$ = 200 GeV.

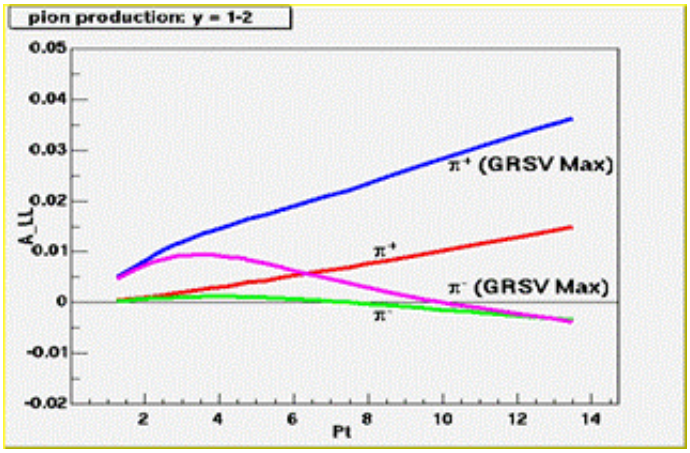

Figure 37 - Model calculation of double spin asymmetry for charged pions within the muon spectrometer acceptance.

2.3.2.3 Measurements of Heavy Quarkonium Production

Presently the most accurate way to measure the polarized gluon distribution in the nucleon is to study those processes which can be calculated in the framework of perturbative QCD, i.e., those for which the involved production cross section and subprocess asymmetry can be predicted. Heavy quarkonium has been a useful laboratory for quantitative tests of QCD and, in particular, of the interplay of perturbative and non-perturbative phenomena, as the heavy quark pair production processes can be controlled perturbatively, due to the large mass of heavy quarks. The factorization formalism of non-relativistic QCD provides a rigorous theoretical framework for the description of heavy quarkonium production and decay. It successfully describes the inclusive cross section of charmonium production at Tevatron and RHIC. In *pp* collisions, heavy quark pairs are mainly produced in gluon

fusion processes, and therefore, asymmetries are expected to be sensitive to the polarized gluon distribution function in the proton. Another advantage of heavy quarkonium is that it provides a very good event-by-event measurement of gluon "*x*" values since we can almost fully reconstruct the parton collision kinematics.

During the RHIC run in 2005, PHENIX accumulated 3.8 pb^{-1} of integrated luminosity with an average beam polarization of 47%. This provides the first opportunity to explore the gluon polarization with heavy quarks at RHIC. Figure 38 shows the opposite charge dimuon pair mass spectrum from run5 *pp* data. The J/ψ signal clearly stands out from the background. There were about 7300 J/ψ candidates from which the double spin asymmetry was measured, see Figure 39.

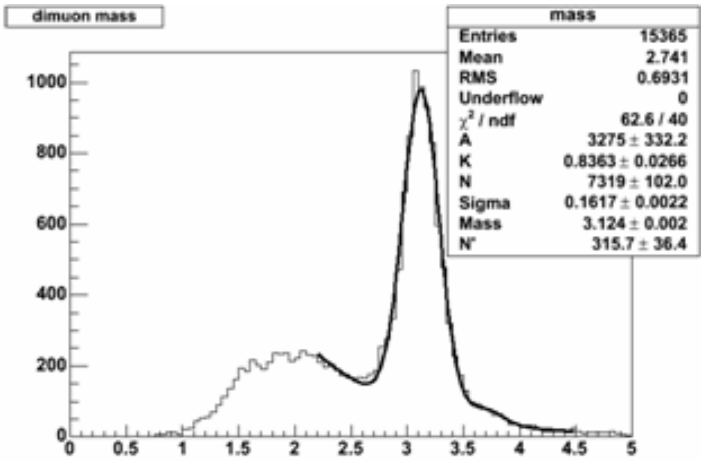

Figure 38 - J/ψ measurement from run5 pp run. The J/ψ peak clearly stands out from the background. The background fraction is about 25% under the J/ψ mass peak.

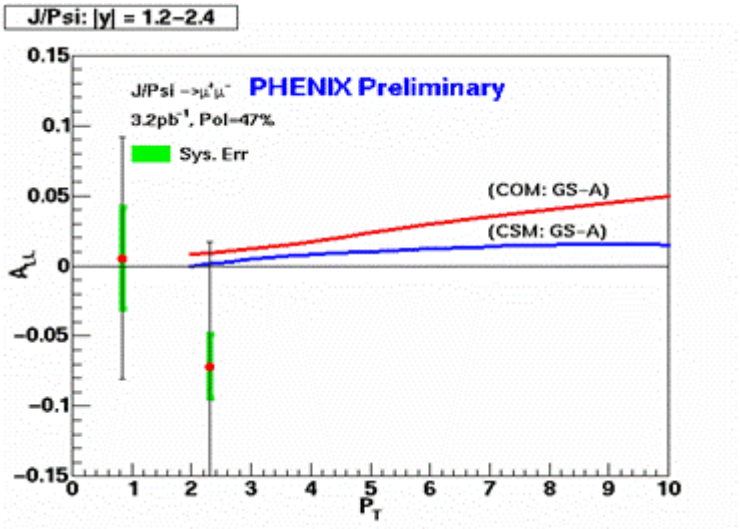

Figure 39 - The first measurement of double spin asymmetry from polarized *pp* collisions at RHIC.

The majority of the background under the J/ψ mass peak is from muons produced by open charm and light hadron decay. As in the case of single muons, at high p_T it is expected that the J/ψ sample will be contaminated by J/ψ's from *B* decay. The proposed forward silicon vertex detector will help us to improve the prompt J/ψ signal purity by rejecting background muon pairs through a cut on displaced vertices since muons from prompt J/ψ decay point back to the original collision vertex. Figure 40 shows the expected asymmetry measurements for prompt J/ψ (not from *B* decay) with projected luminosities at RHIC.

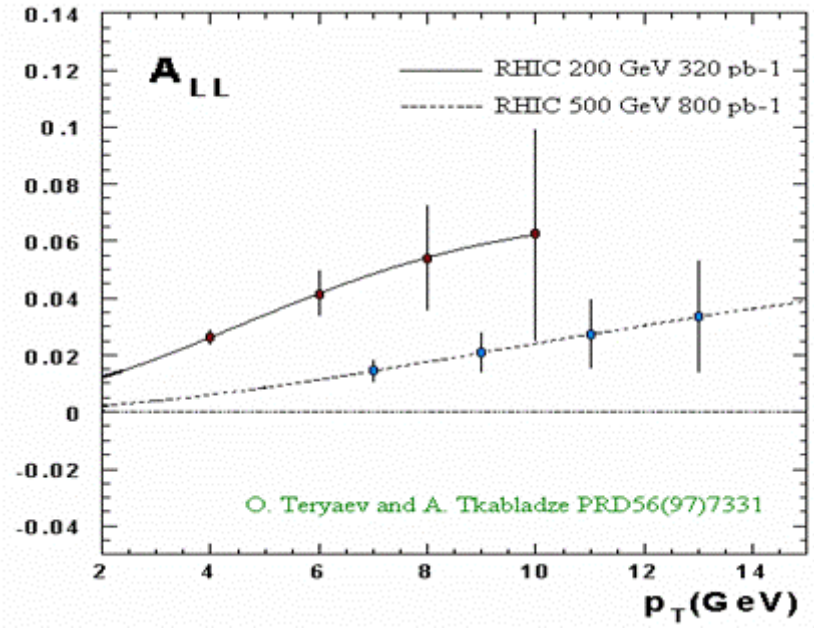

Figure 40 - Expected experimental sensitivities of double spin asymmetry measurements with prompt J/ψ (not from *B* decay).

2.3.3 Polarized Sea Quark Distributions and *W/Z* Production

W production at PHENIX presents a unique opportunity to study the flavor dependence of (polarized) quark and anti-quark distributions inside the proton. The W^+ is produced by collisions of up and anti-down quarks and identified experimentally through a decay muon (Figure 41):

$$u + \bar{d} \rightarrow W^+ \rightarrow \mu^+ + \nu$$

Similarly, for W^-, the process is:

$$d + \bar{u} \rightarrow W^- \rightarrow \mu^- + \bar{\nu}$$

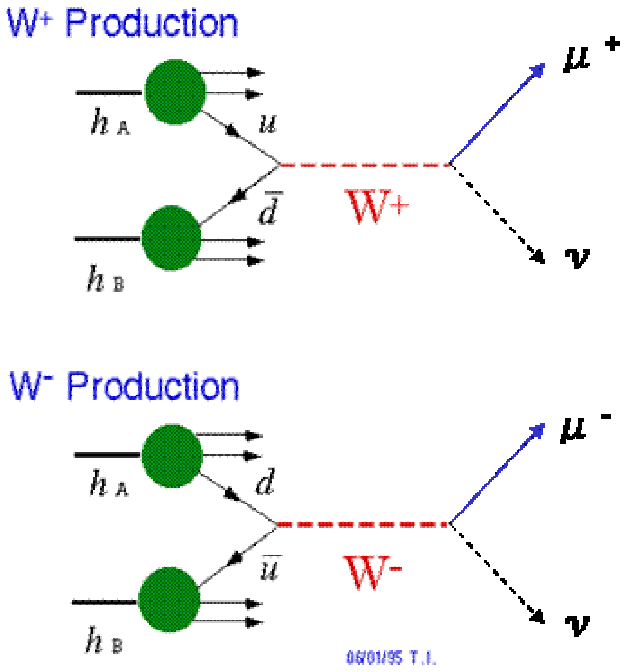

Figure 41 – W production and decay to a muon plus a neutrino.

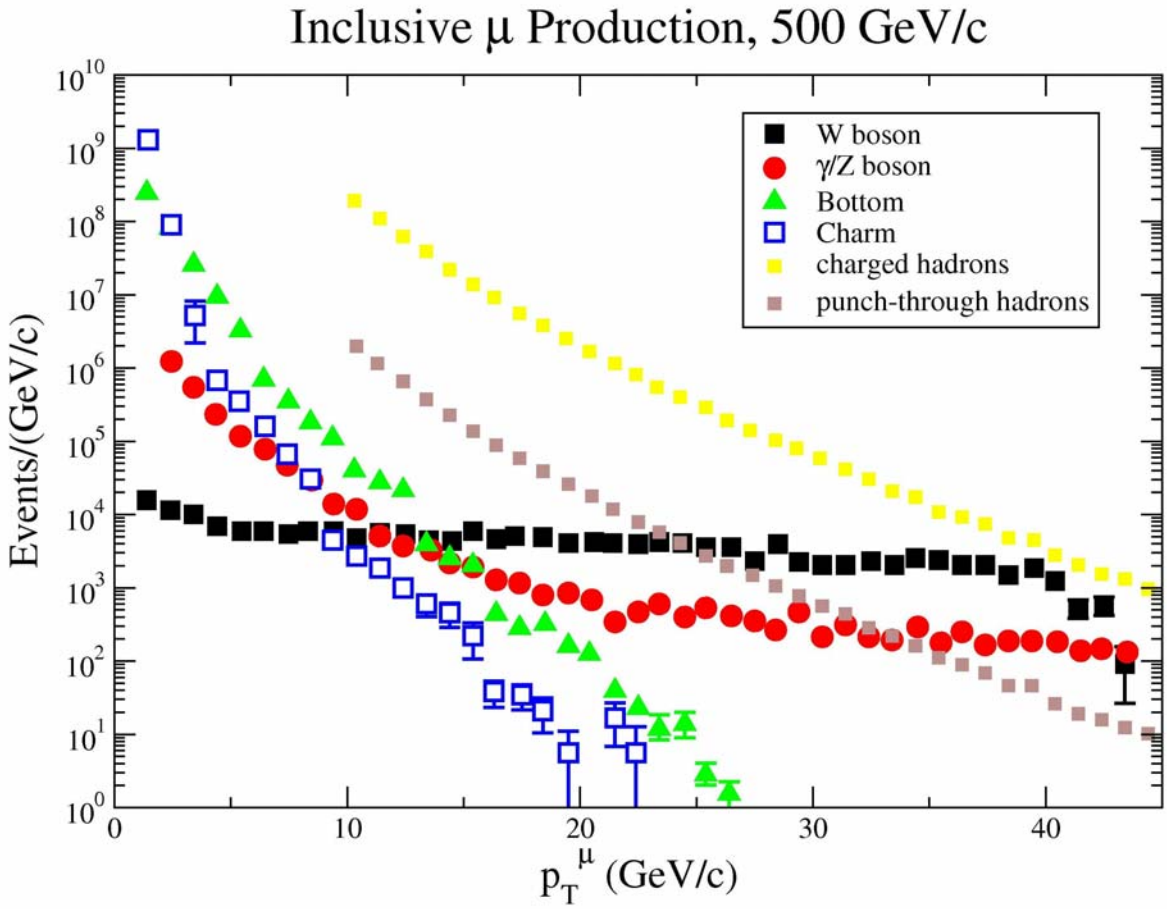

Figure 42 - Inclusive muon production showing punch-through hadrons in brown.

The main background for a *W* measurement is muons from heavy flavor and light hadron decay and/or punch-through (Figure 42). The background from heavy flavor decays can be identified and rejected based on a displaced secondary vertex; for light hadrons, an isolation cut can be used to suppress the background: in general, a muon from *W* decay has no accompanying jet, while a light hadron normally has associated jet particles around it. This could also allow us to extend the *W* physics to a broader kinematic coverage by lowering the minimum p_T requirement for muons from *W* decays. Figure 43 shows the expected sensitivity and *x*-range for the flavor dependent polarized quark distribution functions measured by the PHENIX muon spectrometers at $\sqrt{s}$ = 500 GeV.

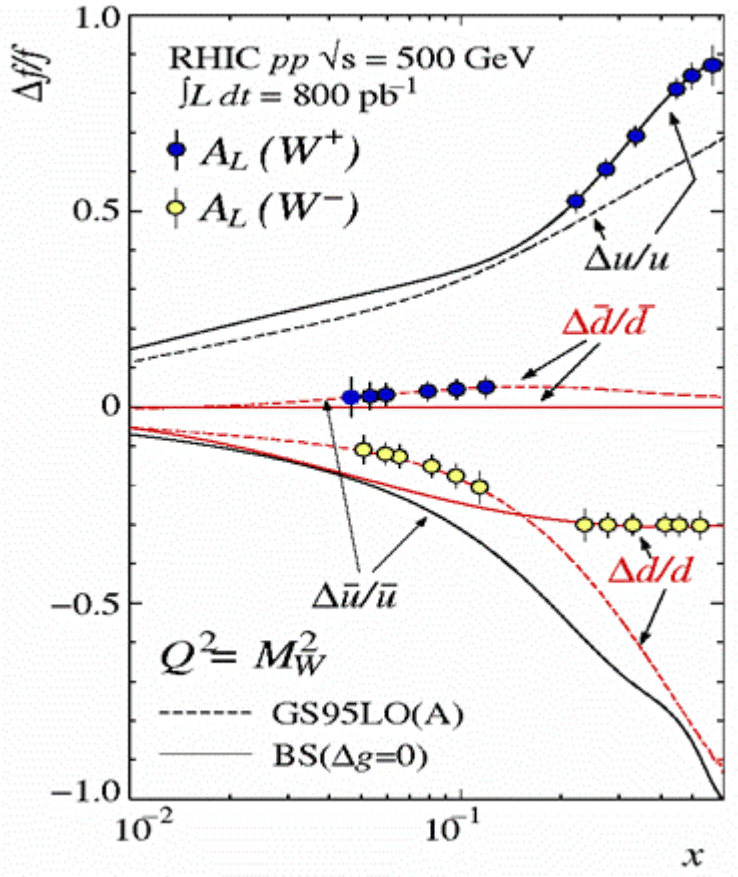

Figure 43 - Expected flavor dependent polarized quark distribution functions measured by the PHENIX muon spectrometers.

2.3.4 Physics with transversely polarized beams

The aim of this section on transverse spin is to make clear another unique measurement that the FVTX upgrade makes possible, namely the measurement of the **Sivers gluon distribution in** $p^{\uparrow}p \to DX$**.** To make this understandable, however, it is necessary to briefly introduce the phenomenology of transverse spin and transversity.

2.3.4.1 Introduction to Transverse Spin Phenomenology

In addition to the familiar unpolarized quark parton distribution function $q(x)$ measured in ep and pp scattering, and the polarized (helicity) distribution function $\Delta q(x)$ measured in $\vec{e}\vec{p}$ and $\vec{p}\vec{p}$ scattering, there is a third equally fundamental distribution function associated with the transverse polarization of the quarks, called the transversity distribution function $\delta q(x)$. In a basis of helicity spin states, the transversity distribution $\delta q(x)$ represents a

spin-flip amplitude between two helicity states. However, in a basis of transverse spin states the transversity distribution $\delta q(x)$ has a probabilistic interpretation similar to that of $\Delta q(x)$ in a helicity basis. For this reason, a measurement program involving transversely polarized protons has been developed at RHIC to measure $\delta q(x)$.

Transverse single spin asymmetries (SSAs) can be produced in a number of ways[xl]. The simplest mechanism is to observe the asymmetry proportional to the triple product of spin *S*, beam momentum *P*, and observed transverse momentum p_T , $A_N \propto S \cdot (P \times p_T)$, in inclusive hadron production $p^{\uparrow} + p \to h(p_t) + X$. However[xli] this asymmetry is suppressed by a factor $\alpha_s m_q / p_T$ and so this mechanism is not useful for the exploration of the transversity distribution function $\delta q(x)$.

Other mechanisms for SSAs arise when one (necessarily) takes into account the effect of initial-state parton transverse momentum k_T. Sivers showed[xlii] that a k_T-dependent quark distribution for a transversely polarized nucleon, anti-symmetric with respect to nucleon spin-flip, can be a source of SSAs. This distribution (now called the Sivers distribution) describes an initial-state correlation between the transverse spin of the nucleon *S* and the parton transverse momentum k_T, and thus contains a tremendous amount of information about the structure of the nucleon. The asymmetry it produces thus is proportional to $A_N \propto S \cdot (P \times k_T)$. As discussed below, this type of asymmetry is of most interest to us in regard to the FVTX upgrade.

Another mechanism involving parton transverse momentum k_T is the Collins-Heppelmann effect[xliii] whereby the final-state jet momentum P_{jet} is correlated to the spin and initial state k_T and produces an asymmetry $A_N \propto S \cdot (P_{jet} \times k_T)$.

The three mechanisms described so far all involve the transversity distribution $\delta q(x)$ through the transverse spin *S*. There is another mechanism to produce a transverse SSA, noted by Brodsky, Hwang and Schmidt[xliv]. Final state interactions between the struck quark and the spectator system can produce such asymmetries. We will not concern ourselves here with this mechanism, because the asymmetry we are most interested to discuss does not require this mechanism to be produced. However, such final state interactions could *modify* the asymmetry of interest.

The Sivers idea can be invoked to define a Sivers gluon function[xlv], and that is the topic of most interest to us here.

2.3.4.2 Measurement of the Sivers gluon distribution in $p^{\uparrow} p \to DX$

Recently[xlvi] a new window into the gluon structure of the nucleon was opened by the understanding that a measurement of the transverse single spin asymmetry in $p^{\uparrow} p \to DX$ is

uniquely sensitive to the Sivers gluon distribution function, see Figure 44. There are two channels that dominate open charm production; *s*-channel quark annihilation $q\bar{q} \to c\bar{c}$, and the gluon fusion process $gg \to c\bar{c}$. Gluons do not carry transverse spin, therefore for **both** of these channels there cannot be any polarization of the final state charm quarks if the initial state protons are only transversely polarized. The lack of final state quark polarization rules out any Collins effect, leaving the Sivers distribution as the only source of a single spin asymmetry.

The FVTX upgrade can make such a unique measurement idea into a reality. As already discussed in other sections of this proposal, *D* production can be tagged on an event-by-event basis, therefore a very clean sample of $p^{\uparrow}p \to DX$ events can be produced for subsequent SSA analysis. This same physics will also be accessible in the central arms, using the VTX upgrade, but this was not known at the time of the VTX proposal because the Anselmino et al. paper was not published at that time.

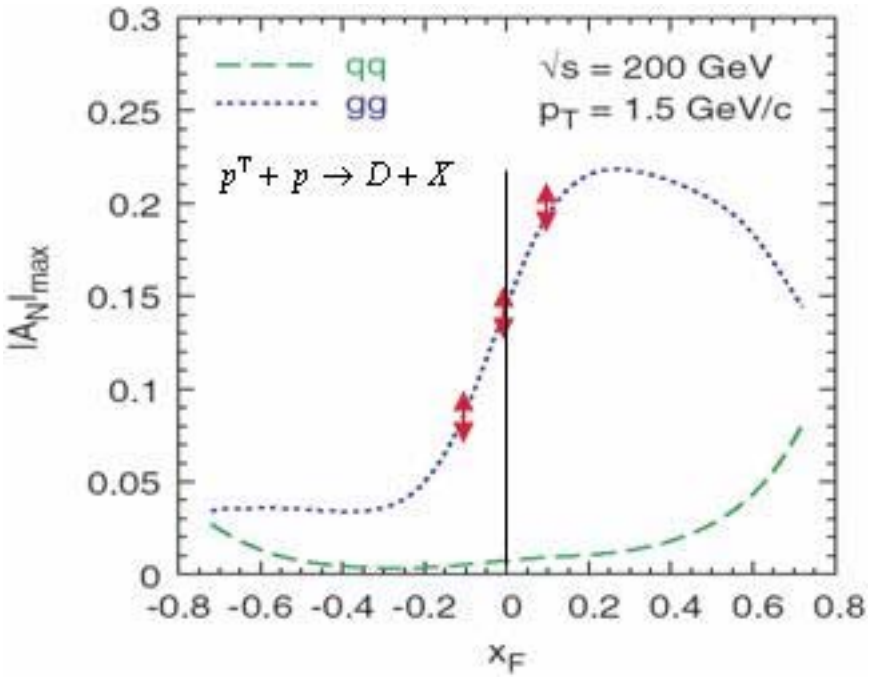

Figure 44 - Maximized values of single spin asymmetry A_N for the process pp->DX as a function of x_F at fixed transverse momentum calculated using saturated Sivers function. The dashed line corresponding to a maximized quark Sivers function (with the gluon Sivers function set to zero), while the dotted line corresponding to a maximized gluon Sivers function (with the quark Sivers function set to zero). Red marks indicate the x_F range that the PHENIX upgraded detectors can measure.

2.3.5 Tests of pQCD Model Calculations and Providing a Baseline for pA and AA Measurements

Spin plays a key role in fundamental interactions. The experimental study of spin observables (polarization, spin correlations and asymmetries) provides information on the most important dynamical properties of particle interactions. Moreover, the spin studies give us more complete information than the measurements of spin-averaged quantities and allow us to make a detailed comparison of various theoretical model calculations with the experiment. The fact that the nucleon spin composition can be measured directly from experiments has created an important frontier in hadron structure physics, has had a crucial impact on our basic knowledge of the internal structure of the nucleon and will eventually lead us to a better understanding of strong interaction phenomena. As an example of how current theory can help us to understand spin dependent QCD dynamics, Figure 45 shows an NRQCD prediction for the double spin asymmetry of the J/ψ in two different helicity states. Experimentally we can identify the helicity state by examining the dimuon angular distribution from the J/ψ decay.

Before using charm and beauty for spin and heavy ion physics, we need to test the next-to-leading-order (NLO) pQCD calculations for heavy-quark production. Qualitatively, low-p_T charm and beauty production are dominated by gluon-fusion, while production at high-p_T is expected to be dominated by the hard-scattered gluon splitting into a $Q\ \bar{Q}$ pair[xlvii]. Present data on charm and bottom production is scarce and of limited statistics. Data from polarized *pp* collisions at RHIC will provide critical information about our understanding of heavy quark production mechanisms.

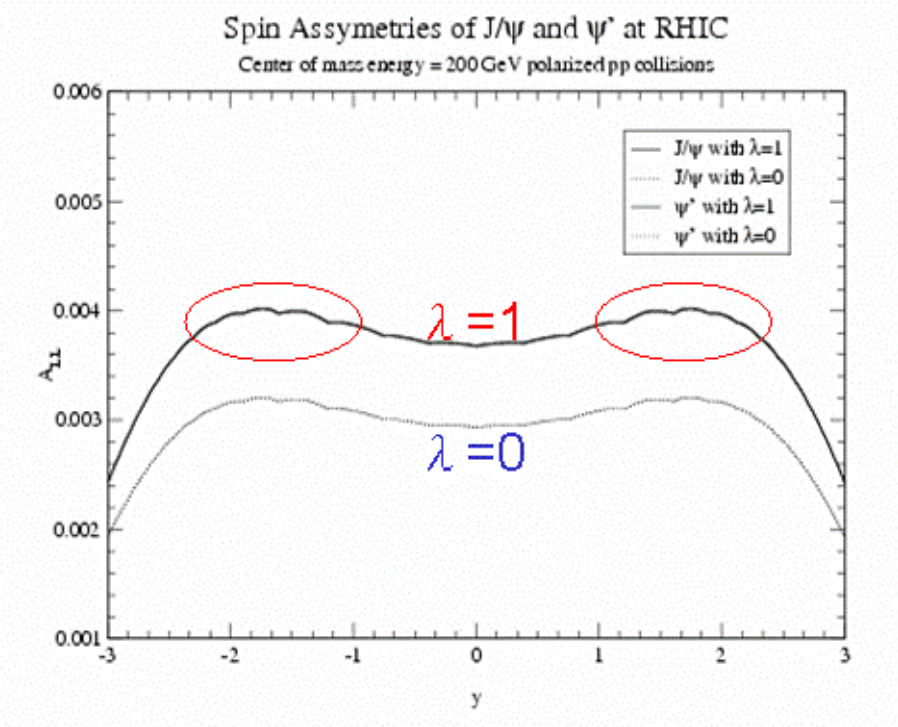

Figure 45 – Predicted double spin asymmetry for charmonium at RHIC[xlviii]. The asymmetry value depends on the final state charmonium polarization, which can be tested experimentally. The red circles indicate the acceptance region for the PHENIX muon arms and FVTX detector.

2.3.6 Summary of Physics Addressed by the FVTX in Polarized *pp* Collisions

In summary, the FVTX detector will significantly improve on the following physics in polarized *pp* collisions:

- Probing the polarized gluon distributions via muons from light hadron, open charm and beauty decay.
- Measurement of flavor dependent polarized quark distributions via muons from *W* production and providing the first experimental test of SU(2) flavor symmetry for polarized sea quarks.
- Providing a vital cross check of pQCD calculations for light and heavy hadron production in polarized pp collisions.

2.4 The Case for Two FVTX Endcaps vs One

There are a number of compelling reasons for having a FVTX in front of both South and North muon arms.

- In any asymmetric collision the physics can be quite different between the forward and backward rapidity regions and to capture all of this physics at once is clearly economical, as otherwise one would have to pay the cost of reversing the beams and then running twice as long. It is estimated that to reverse the beams in d+Au collisions might take 2-3 weeks and thus could cost as much as $2-3M. In d+Au collisions, as shown in Figure 46, the centrality dependence for production of various type of particles is quite different at forward rapidity (deuteron direction) and at backward rapidity (Au direction). See 2.22.2 for discussion of d+Au physics.

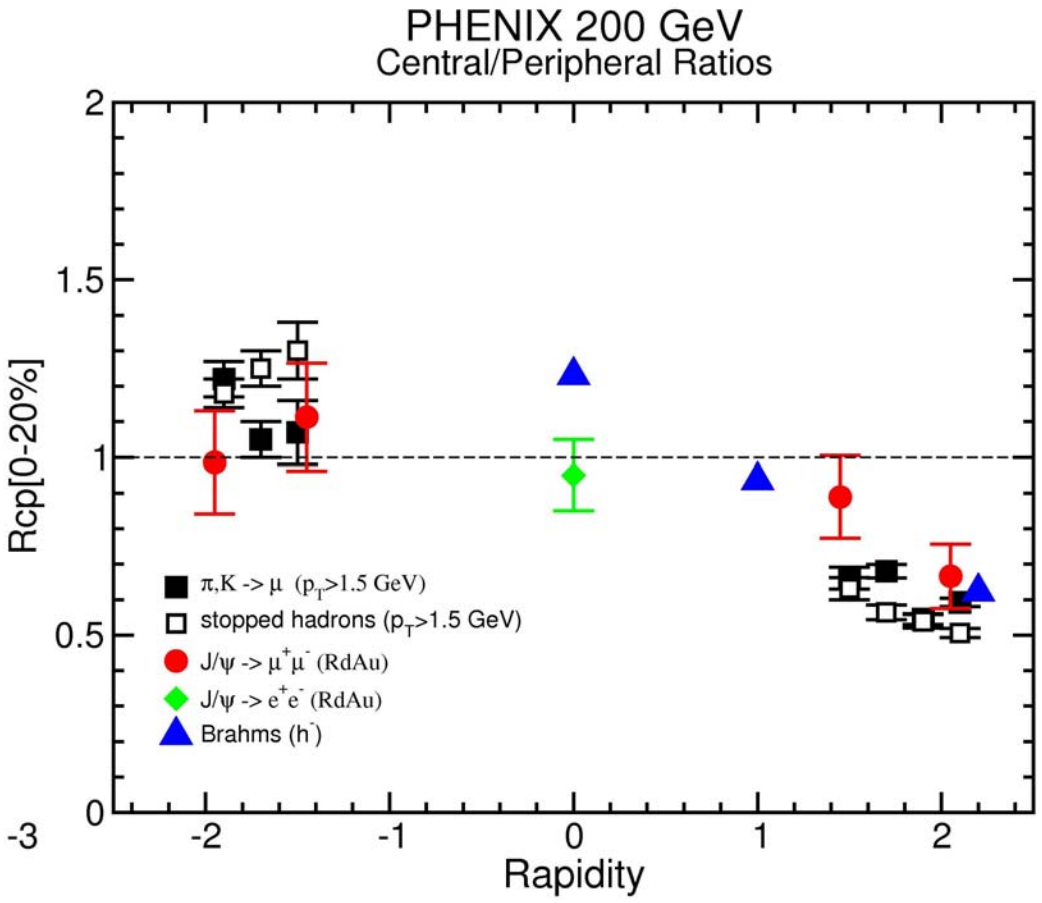

Figure 46 - Nuclear modification in dAu collisions in terms of the ratio between central and peripheral collision yields, Rcp, for light hadrons that decay into muons from PHENIX, compared to similar results from Brahms and to PHENIX data for the J/ψ.

- The simple factor of two in yield is also quite important for many of the rare probes, e.g. J/ψ, ψ', ϒ, Drell-Yan and B → J/ψ X, since their rates are small and results are often limited by statistics.
- Another direct benefit is the ϒ's and high-mass Drell-Yan events at mid-rapidity that can be seen by detecting one muon in each arm. As was shown in Figure 20, these signals have huge backgrounds from random coincidences of light-meson decays or punch-through hadrons in the two arms, so the FVTX's capability to eliminate much of this background is essential to make the two-arm signals clean enough to see.
- In symmetric collisions the simultaneous measurements in the two endcaps will also provide a robust check of the systematics by providing two largely independent measurements for comparison.

3 Simulations and Required Performance for the FVTX Upgrade

Now we will discuss the feasibility and performance issues that allow the FVTX to address the many physics topics discussed in the previous sections. Most of the physics studies require complementary studies in p+p, d+A and A+A collisions in order to establish the physics of the production (p+p), of the cold nuclear matter effects (p(d)+A) and of the effects of hot-dense matter (QGP) in heavy-ion collisions. Some of the most challenging performance issues occur in Au+Au collisions, especially in central Au+Au collisions where the occupancy and matching between the FVTX tracks and muon tracking tracks are most challenging. Here we will concentrate on the FVTX itself, but there are also very important issues that cross subsystem or upgrade subsystem boundaries including coordination of different subsystems (e.g. muon tracking, muon identifier, FVTX, muon trigger upgrade). These cross-subsystem issues will be discussed in the Appendices with synergy of subsystems in 9 and global forward triggering in Appendix B (Section 7).

The physics-driven requirements for the FVTX silicon endcap detectors include:

- Ability to match tracks from the muon arm (muon tracker and muon identifier) to those in the FVTX silicon mini-strips.
- Having sufficient segmentation to achieve clean matching to the correct FVTX track even in central Au+Au collisions where the density of soft light hadrons is highest. Occupancy levels of <1.5% are targeted.
- Sufficient position accuracy in the r-z plane so that the displacement resolution of the track with respect to the collision point is less than the $c\tau$ of charm and beauty decays, i.e. a resolution in z of less than 100μm, preferably at the level of ~50 μm for high momentum muons.
- Excellent accuracy for the primary vertex (<200 μm) using all tracks seen in the FVTX as well as those from the VTX (central rapidity barrel) vertex detector; with high efficiency (> 90%) even for p+p collisions.
- Good resolution in both r-ϕ and z are required. The 100μm z resolution quoted above is roughly equivalent to 40μm in distance-of-closest approach (or transverse separation of the detached and primary vertex points)

The following discussion of these requirements and the simulations that establish the FVTX performance to satisfy the requirements follow. First we discuss the general characteristics of the detector that go into the simulations, then performance estimates for the detached and primary vertices. Following that we look in detail at charm measurements via single muons, and then measurements with muon pairs (quarkonia and $B \rightarrow J/\psi\ X$). There is then a brief discussion of triggers and of rates for the different processes (with details in the Appendices). Finally we discuss the matching issues between the FVTX tracks and those in

the existing muon spectrometer, especially those for central Au+Au collisions, which are the most challenging.

3.1 General characteristics and track-level performance of the FVTX

For the simulations we have used a nominal thickness of 1% of a radiation length for each layer. This includes detector, readout and cooling in a simplified one-volume effective layer. 1% is achievable because we are implementing a design that has incorporated a readout bus in the silicon chips and sensors and we are able to thin the chips. We are striving to minimize this thickness, in particular for the critical first disk.

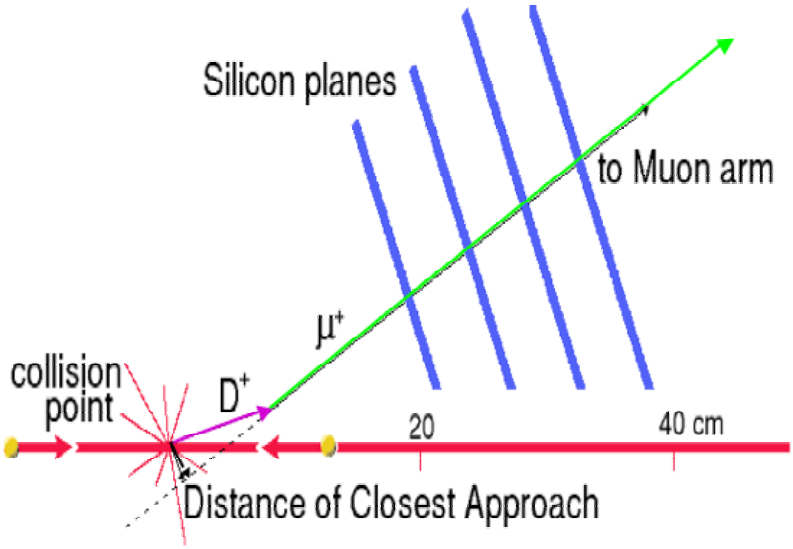

Figure 47 - Principle of operation of the FVTX silicon endcap detector in the r-z plane. A D meson is produced at the collision point. It travels a distance proportional to its lifetime (purple line), then decays to a muon (green line). The muon's trajectory is recorded in the four layers of silicon. The reconstructed muon track (dashed line) has a small, but finite distance of closest approach (dca) to the collision point (black line). The primary background is muons from pion and kaon decays, which have a much larger average dca.

Figure 47 shows the basic principle of operation of the FVTX endcap silicon detector. A D meson is created at the point where the two beams collide. It travels a distance proportional to its lifetime and then decays semi-leptonically into a muon. The muon travels off at a different angle (due to the decay process), passing through four silicon planes with 50μm radial pitch. The reconstructed muon track has a small but non-zero *distance of closest approach* (dca) – typically 200-300μm, unlike particles from pion and kaon decays, which have a much larger average dca.

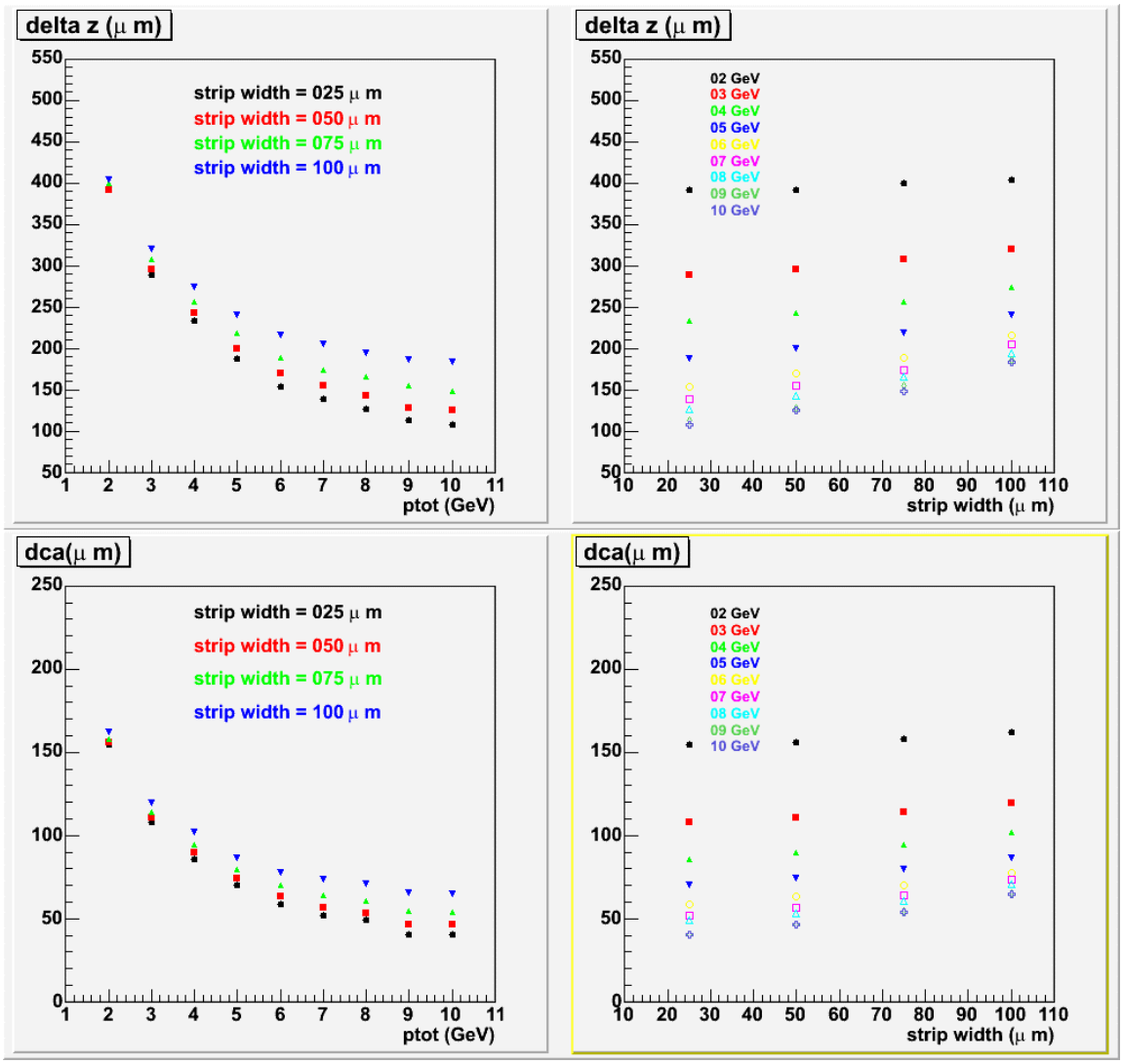

Figure 48 - Top panels: Simulated z-vertex resolution (microns) versus muon momentum (in GeV) and strip width (microns.) For example, with 50 micron strip spacing, a 5 GeV muon provides a z-vertex resolution of ~200 microns. Bottom panels: The corresponding resolution in terms of distance of closest approach is about three times smaller. The dca resolution for the 5 GeV muon is ~ 70 microns.

A simulation of the z-vertex resolution for single muons, as a function of transverse momentum and strip width is shown in Figure 48. The simulation includes the beam pipe, the central silicon barrels and the forward silicon tracker, with ~1% of a radiation length per silicon layer. The resolution is dominated by multiple scattering at low momenta and by the silicon strip width at high momenta. Also shown in the figure are the dca resolutions, which are about a factor of 3 smaller than the corresponding z-vertex resolutions. These

resolution studies do not include the effects of charge sharing, which could significantly improve the track resolution.

The endcap mini-strips vary in size with a radial pitch of 50μm and widths in ϕ (or mini-strip lengths) that vary between 2 and 13.5 mm as the radius increases. The simulated hit density at the first silicon layer for central collisions is shown in Figure 49. For 50μ×2mm strips at the smallest radii, a density of 7cm^{-2} translates into an occupancy = 0.7%. Accounting for charge sharing and a possible under-prediction of the total yield of soft charged particles, the maximum occupancy is expected to be ~1.5% for Au-Au central collisions.

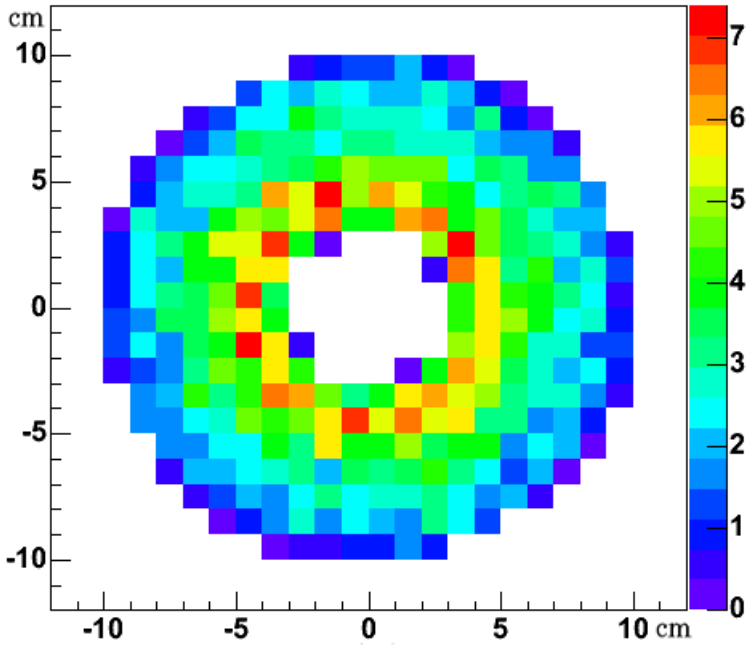

Figure 49 - Simulated occupancy at the first silicon plane for Au-Au central collisions using the Hijing model. The color scale is in units of hits per cm^2, with a maximum of 7 hits per cm^2 at the inner radius. The other silicon planes have lower occupancies.

3.2 Locating the Primary Vertex

The identification of displaced vertices depends on the accuracy with which the primary vertex can be determined. This is true for both the offline event reconstruction of the FVTX as well as any level 1 trigger algorithm that attempts to identify tracks from heavy quark

decays. We have studied the primary vertex resolution in p-p, p-Au and Au-Au central collisions, using HIJET together with PISA. For each beam species, the average number of particles traversing the FVTX were determined. These particles are typically soft pions with a mean momentum of about 1.4 GeV/c and most probable momenta of about 600 MeV/c. Each of these typically provides an impact parameter measurement with an accuracy of 160 μm, or an equivalent vertex resolution of 400 μm. Assuming that the accuracy of the vertex determination scales inversely as the square root of the number of measured tracks results in the primary vertex accuracies are shown in the table below. Since these tracks are all in the FVTX, they are available to a level 1 trigger. Also shown in the table are the additional pions detected in the VTX, which can be used to improve the vertex determination offline. The vertex resolution provided by each of these is about 210 μm.

Table 1 - Determination of primary vertex using prompt pions, shown versus collision species.

Collision Species at √s= 200 GeV	Number of pions detected in FVTX	Accuracy of primary vertex determination from FVTX alone	Additional pions in VTX	Primary vertex accuracy with FVTX + VTX
p-p min bias	5.8	168 μm	~3	98 μm
p-Au min bias	11.2	120 μm	~6	69 μm
Au-Au central	1730	10 μm	~900	6 μm

3.3 Charm Measurements

Si Endcaps: $D \to \mu X$, $D\overline{D} \to \mu e X$, $D\overline{D} \to \mu^+ \mu^- X$, $J/\psi \to \mu^+ \mu$, $\psi' \to \mu^+ \mu^-$

3.3.1 Single muons from semi-leptonic D meson decays: $D \to \mu X$

Each silicon endcap detector has four layers of pixel detectors, which measure the trajectory of particles within the nominal rapidity acceptance of the muon arms. The impact parameter of each track is determined accurately along the Z (beam) direction. For each detected muon, the impact parameter is used to eliminate muons that come from pion and kaon decays. These long-lived decays are the primary source of background muons with transverse momenta below 3 GeV/c. At higher momenta, hadrons which punch through the nosecone and central magnet steel are the primary background. These include hadrons which decay in the muon tracking volume and those that punch through even the steel layers of the muon identifiers.

Contrasted with these background muons are "prompt" single muons, which come from more short-lived decays, e.g. open charm and beauty. For transverse momenta below ~5 GeV/c the prompt muons are primarily from semi-leptonic charm decay. Other processes that produce prompt muons, such as J/ψ or Drell-Yan decays to muon pairs, have much smaller cross-sections times branching ratios. Muons from *B* decays become important only at larger transverse momenta.

The PYTHIA event generator was used to simulate semi-leptonic charm decays to muons. The total charm pair cross-section of 920 μb is taken from the PHENIX experiment at 200 GeV[xlix]. The decay muons were tracked through the proposed silicon vertex detector and then through the muon spectrometer using the PHENIX simulation package PISA. See Appendix C (Section 8).

The mean vertex of the detected muons from charm decay is 785 μm from the interaction vertex. This is ~2.5 times larger than the proper decay length of semi-leptonic charm decays (318 μm), due to the Lorentz boost. The impact parameter resolution for these muons ranges from 92 to 115 μm (and ~2.5 times larger for z-vertex resolution), depending on how many layers of silicon are traversed. By requiring that the muon vertex is within 1cm of the collision point we remove many of the muons from pion and kaon decay while retaining prompt muons from charm and beauty.

Figure 50 shows a simulated muon p_T spectrum, including charm, beauty and light quark decays, before the application of a vertex cut. The background from light quark decays dominates the spectrum below 4 GeV/c. The p_T distribution of muons that survive a 1 cm vertex cut is shown in Figure 51. This vertex cut reduces the muon background from light mesons by about an order of magnitude over what the muon arm alone can achieve, making a charm measurement possible even at low p_T. Note that the removal of the muon background from pion and kaon decays could be achieved with a detector with less spatial resolution. The resolution requirement is mainly driven by the physics program of measuring open beauty and rejecting punch-through hadrons (see next sections).

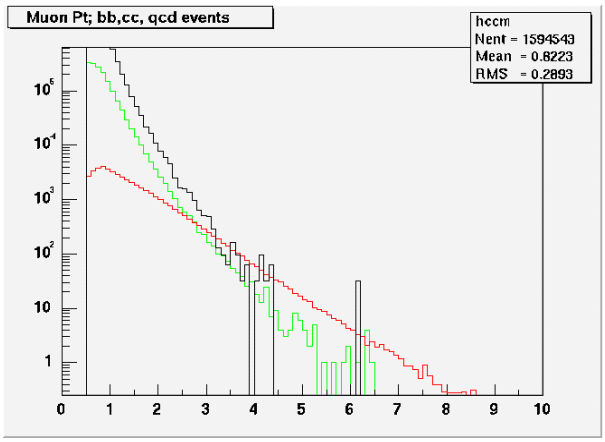

Figure 50 - Single muon p_T distributions for charm, beauty and backgrounds from low-mass meson decays, as expected for the 2003 d+Au run. Note that the light-meson decays are above charm up to near 4 GeV/c. The black curve is for pion and kaon decays, green is charm and red is beauty.

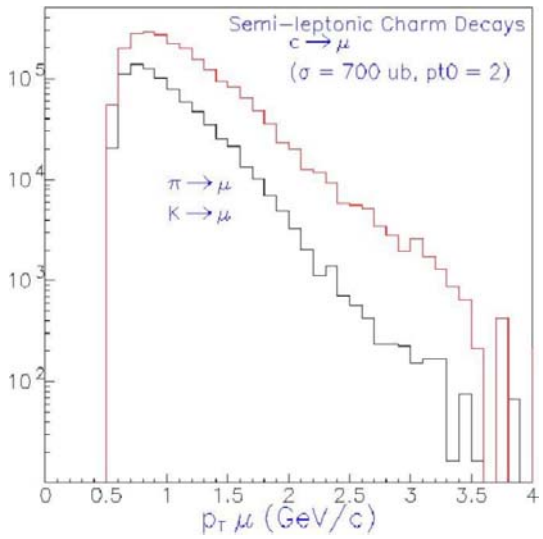

Figure 51 - The p_T distribution of muons that decay within 1 cm of the collision vertex. The red histogram is for charm decays while the black is for pion and kaon decays.

To further elucidate the power of the FVTX to reduce backgrounds we study the signal-to-background for various types of tracks when vertex cuts are made with the FVTX tracks. First lets examine the rejection of light hadron decays when the distance-of-closest-approach (DCA) is required to be smaller than certain values. This kind of vertex cut will eliminate large detached vertices which will be dominated by the light hadron (pion and Kaon) decays into muons, while keeping the smaller detached vertices from charm and beauty as well as the prompt particles that come directly from the primary vertex. The signal/background (Figure 52) is shown for D and B mesons relative to pion and Kaon decays for four different DCA cuts (no cut and < 0.5, 1.0, 1.5 σ_{DCA}). The values for σ_{DCA} are given in Table 2. The signal-to-background ratio can be brought to near one for both charm and beauty at transverse momenta above 2 GeV/c. Further rejection with more sophisticated cuts, such as those using a full Kalman filter fit of the tracks, may also be possible. The reduction of the light-hadron decays by this maximum DCA cut will be particularly important for the small-p_T part of the heavy-quark spectrum where the light hadrons otherwise dominate.

In these studies the relative base charm and beauty yields are taken from the yield calculations of Appendix 8 and the balance between heavy-quark production, decays of light hadrons and hadron punch-through is obtained from the p+p measurements shown in Figure 53. The resolution in decay length includes the effects of multiple scattering and digitization for 50 μm mini-strips.

Table 2 - Sigma of the DCA for the decay of different types of 5 GeV particles as used in the DCA cuts for Figure 52, Figure 54, Figure 55 and Figure 56.

Paticle Type	σ_{DCA}
Hadron punch through	73 μm
Pion	540 μm
Kaon	6924 μm
D	173 μm
B	424 μm

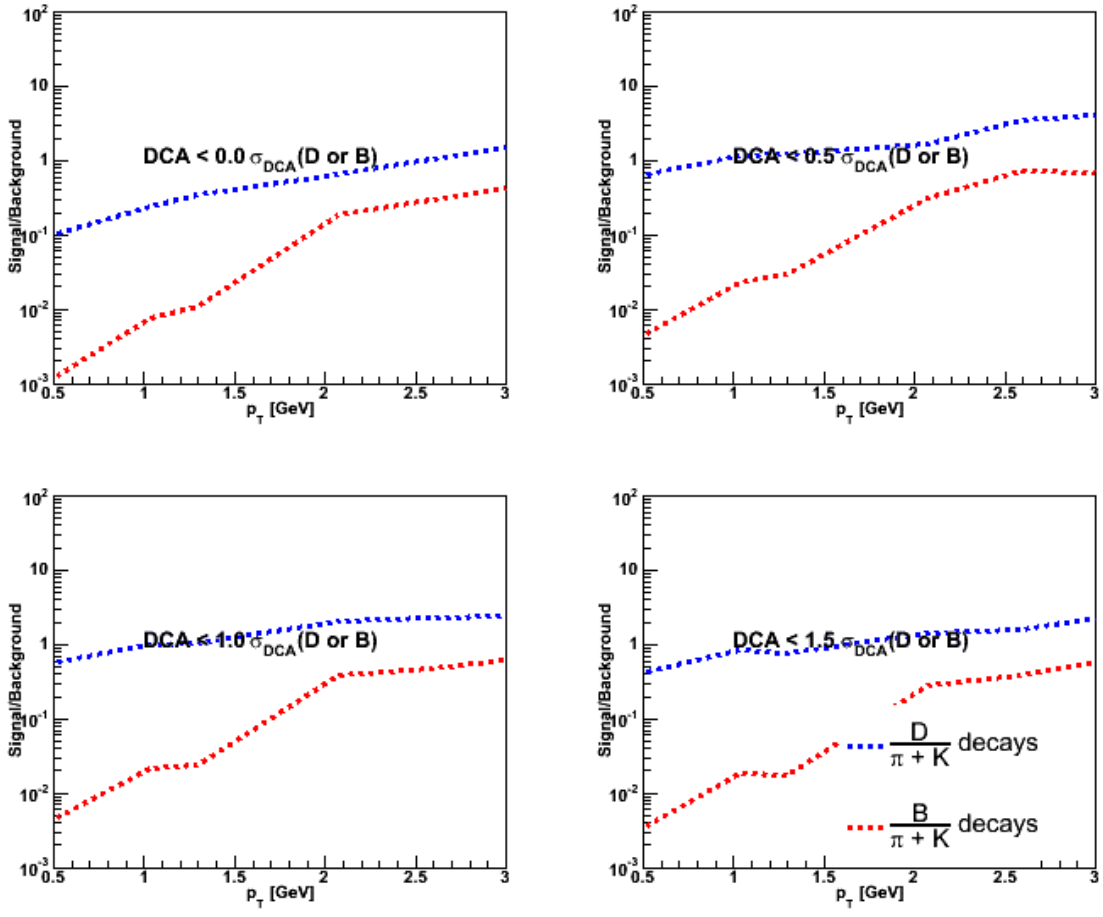

Figure 52 - Signal to noise for charm over pion + Kaon decays (blue) and beauty over pion + Kaon decays (red) vs p_T for several different maximum DCA cuts as shown.

Note that the punch-through hadrons are not shown in the preceding figures. Estimates of the relative amount of these hadrons versus the hadron decays and prompt muons are shown in Figure 53. The punch-throughs can be removed by applying an impact parameter cut to eliminate tracks originating within one or two sigma of the prompt vertex. Unlike the loose cut used to eliminate hadron decays in Figure 52, this cut requires good spatial resolution for high momentum tracks.

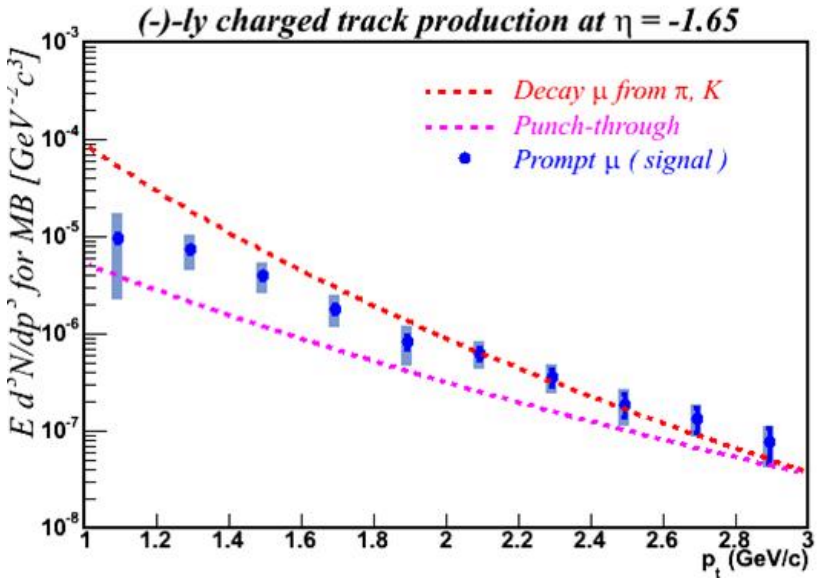

Figure 53 - The p_T distribution of negative prompt muons, decay muons and punch-through hadrons at pseudorapidity (η) = -1.65. The punch-throughs become the dominant background for p_T values above 3 GeV. The curves are simulations, while the data are PHENIX measurements.

An estimate of the effectiveness of a vertex cut that eliminates prompt decays (including punch-throughs) as discussed above, is shown in Figure 54 (signal-to-background for heavy quarks compared to punch-through hadrons). Here one can see that signal-to-noise can be brought well above one with values above ten for $p_T > 2$ GeV/c when small decay lengths are excluded.

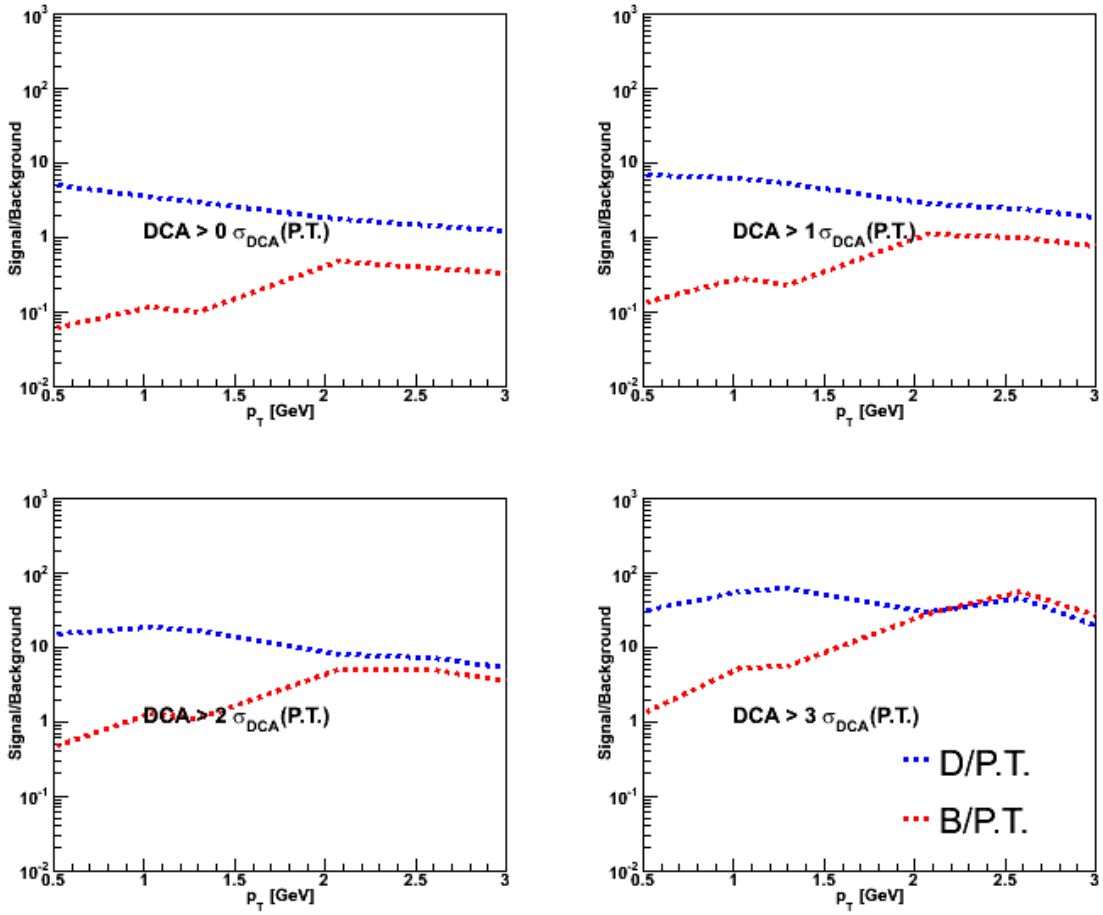

Figure 54 - Signal to noise for charm over punch-throughs (blue) and beauty over punch-throughs (red) vs p_T for several different DCA cuts as shown.

Finally we show signal-to-noise for charm (Figure 55) and for beauty (Figure 56) when a combined "window" cut is made that excludes both long decay length light hadron decays and prompt (small decay length) punch-through hadrons, i.e. a combination of the cuts shown in the previous plots. Here the signal-to-noise for charm (Figure 55) to the total (light hadron decays + punch-through hadrons) with this window cut is above one at all values of p_T. While for beauty (Figure 56) a signal-to-noise above one is achieved for values of p_T above about 2 GeV/c.

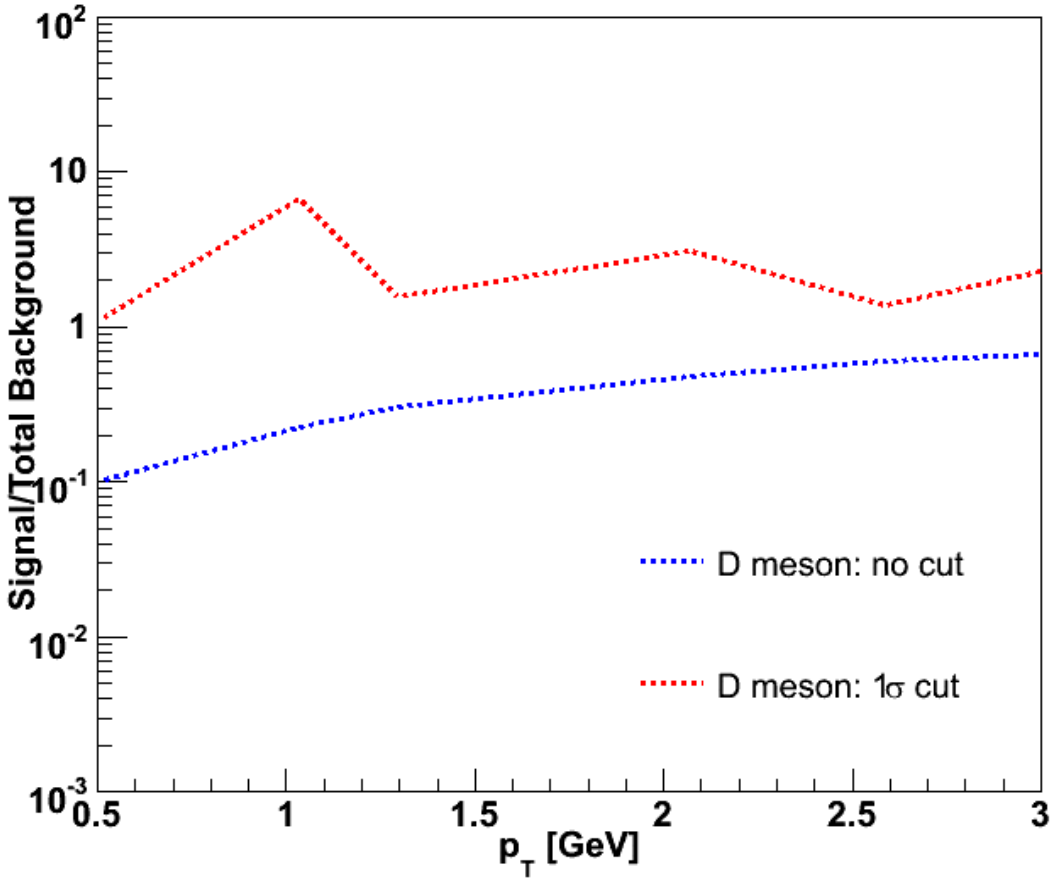

Figure 55 – Signal to background improvement between no vertex cut and a "window" cut at 1 sigma that excludes both large (pion and Kaon) and small (prompt punch-through hadrons) decay lengths for charm.

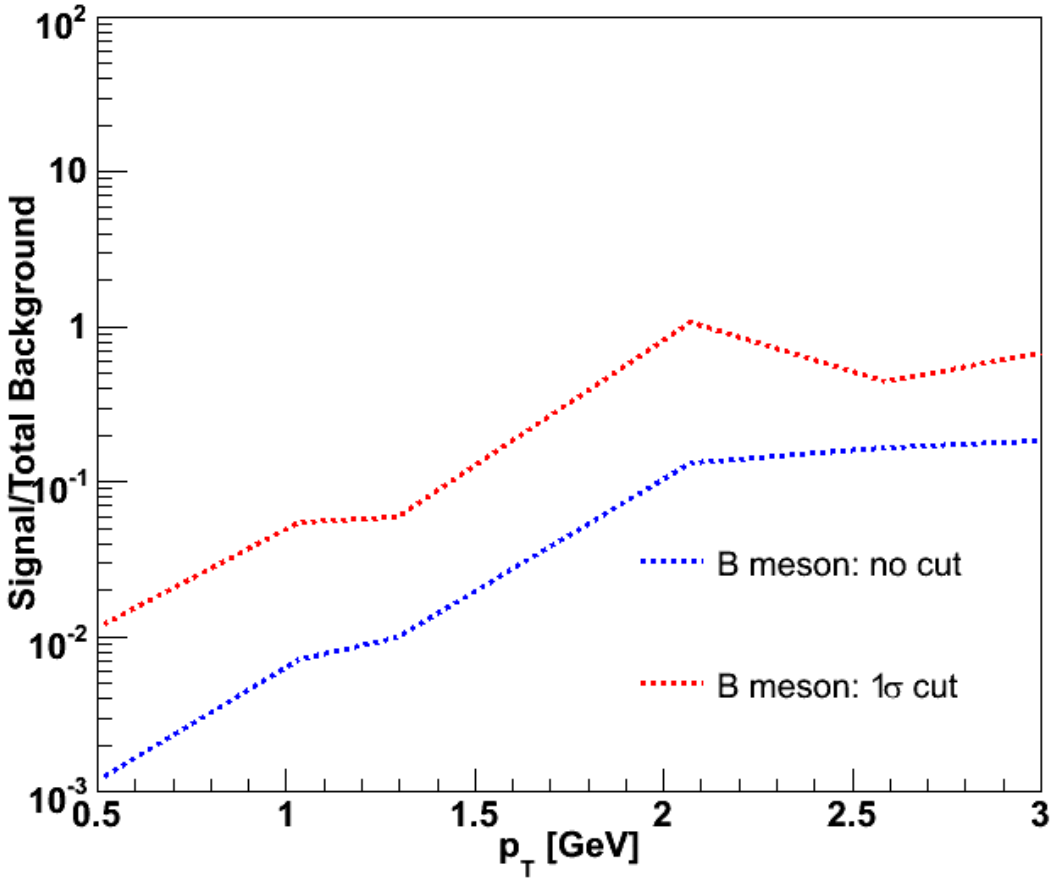

Figure 56 - Signal to background improvement between no vertex cut and a "window" cut at 1 sigma that excludes both large (pion and Kaon) and small (prompt punch-through hadrons) decay lengths for beauty.

To calculate the yield of charm, we assume a 920 μb D pair cross-section and an integrated RHIC-II *p*+*p* luminosity of 33 pb^{-1}per week. A total of ~$7x10^7$ semi-leptonic charm decays would be reconstructed. This rate is before application of a vertex or impact parameter cut. See details of the rate calculations in Appendix C (Section 8). Even if a large pre-scale is required for single muon triggers, the yield is still very large. Trigger issues are discussed in more detail in Appendix B (Section 7).

The momentum vector of the charm decay muon is correlated with the Bjorken-x variables of the two gluons that fused to create the charm quark pair. x_1 is primarily correlated with p_Z and x_2 with p_T of the muon. The fitted correlations from PYTHIA are shown in Figure 57. These can be used to extract model dependent measurements of the gluon momenta.

Since charm is produced in pairs, coincidence measurements of opposite-sign lepton pairs may serve to further enhance the signal to noise in *p*+*p* and *p*+*A* reactions. One could use vertex identified muon-electron coincidences to obtain a clean charm pair signal in the rapidity interval midway between the PHENIX central and muon arms.

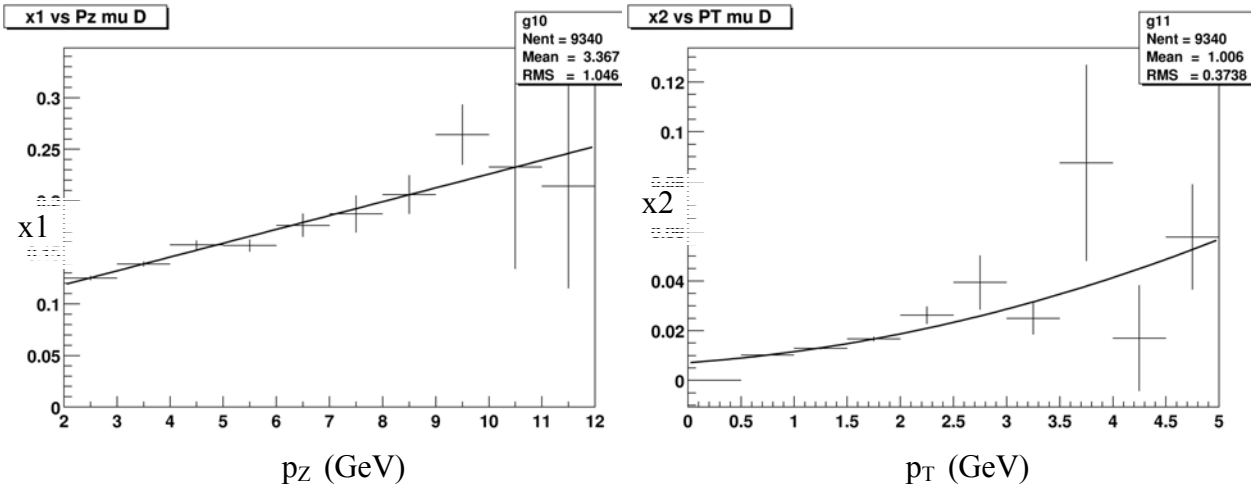

Figure 57 - Left panel: Correlation between x_1 and p_Z of muons from D meson decays (PYTHIA simulation.) Right panel: Correlation between x_2 and p_T.

3.3.2 Muon Pairs from J/ψ and ψ' Decays: J/ψ → $\mu^+\mu$, ψ' → $\mu^+\mu^-$

The PHENIX muon spectrometers provide large acceptance for dimuon events. On the order of 10,000 J/ψ decays have been reconstructed from data taken so far. Unfortunately, the precision of the J/ψ data from Au-Au interactions is currently limited by the uncertainty in the background underneath the J/ψ. This background is due to a combination of decay muons and punch-through hadrons.

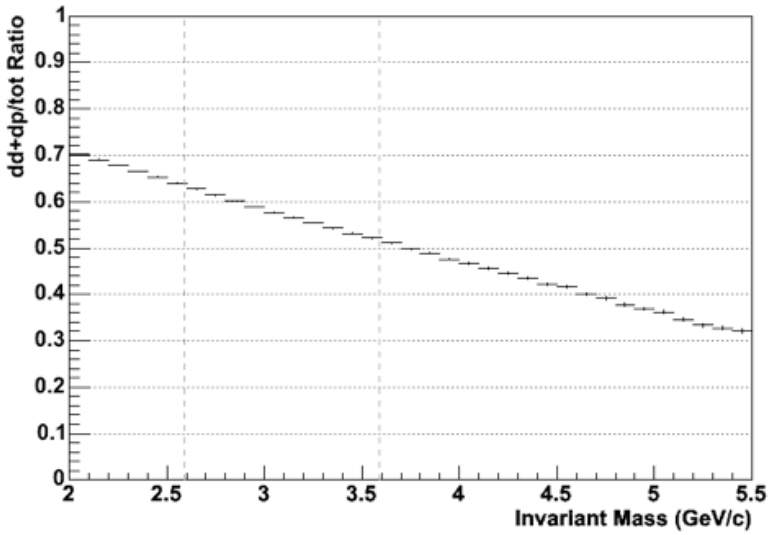

Figure 58 – Fraction of dimuon pair background containing decay muons versus dimuon mass. At the J/ψ mass (3.1 GeV), about 60% of the total background contains at least one decay muon, which can be rejected using the FVTX.

Figure 58 shows the estimated composition of the background in the J/ψ mass region. The vertical axis is the ratio of background events containing a decay muon to the total background. The FVTX detector can eliminate about 60% of the total background, by rejecting these decay muons. The punch-through hadrons cannot be easily eliminated by a vertex cut, since they are prompt. Figure 65 shows a preliminary dimuon mass spectrum for the most central collisions from Au-Au. The J/ψ peak is only visible after background subtraction. A factor of two reduction in the background under the J/ψ peak, coupled with an improved mass resolution described below, would significantly increase the accuracy of the J/ψ measurement.

Simulations of the background improvement for the dimuon mass spectrum are shown in Figure 59 for p+p collisions, Figure 60 for minimum-bias Au+Au collisions, and Figure 61 for central Au+Au collisions. For these simulations we assume that background from light meson decays is completely removed by the FVTX cuts, while the hadron punch-through remains as was discussed above. For the p+p spectrum the signal-to-background for the J/ψ is already quite good, so the improvement is not as dramatic. Howerver for the Au+Au collisions, especially those for central Au+Au (Figure 61), the J/ψ peak is very hard to see until the FVTX eliminates the light hadron decays and the improvement is quite dramatic. In these simulations, besides rejection of the light hadron decays, we also have an improvement of the J/ψ mass resolution from 150 MeV to 100 MeV. The yields are representative of those expected for RHIC-II luminosities and the starting signal-to-background ratios are taken from recent runs for Au+Au. Of course, we also expect that

with more sophisticated cuts in the future, we will be able to eliminate some of the punch-through's as well and further improve the signal-to-backgrounds shown here.

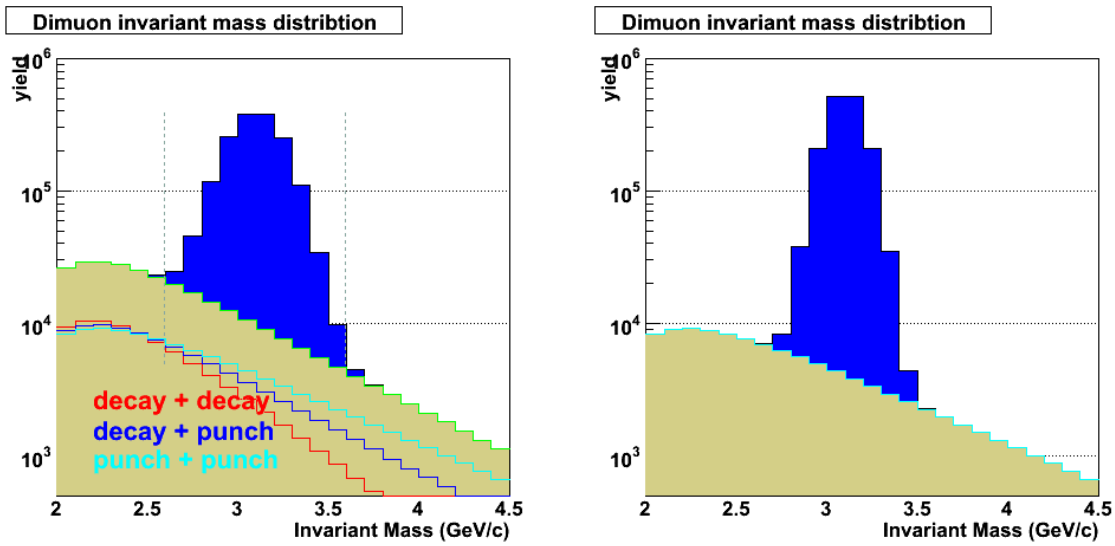

Figure 59 - Simulated dimuon mass spectrum for p+p collisions before (left) and after (right) FVTX vertex cuts are applied to eliminate the light meson decay backgrounds. The mass resolution of the J/ψ is also improved from 150 MeV to 100 MeV, as shown, by the FVTX. These plots correspond to a 10 week RHIC-II run and the initial signal/noise (before the FVTX cuts) is set according to that observed in the 2005 p+p run. There are about 15 million J/ψ events in the peak.

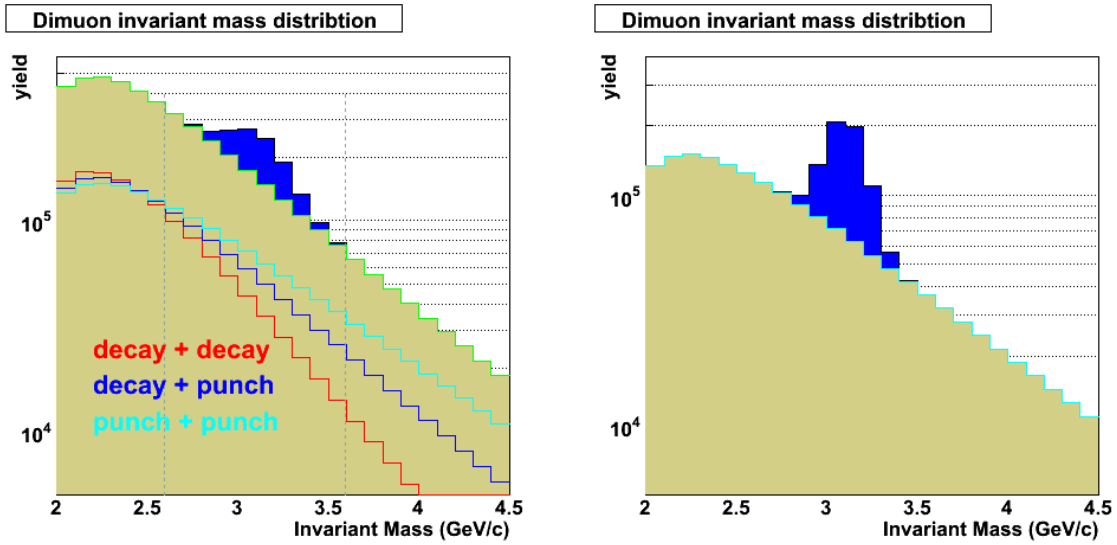

Figure 60 - Simulated dimuon mass spectrum for minimum bias Au+Au collisions before (left) and after (right) FVTX vertex cuts are applied to eliminate the light meson decay backgrounds. The mass resolution of the J/ψ is also improved from 150 MeV to 100 MeV, as shown, by the FVTX. These plots correspond to a 10 week RHIC-II run and the initial signal/noise (before the FVTX cuts) is set according to that observed in the 2004 Au+Au run. There are about 400,000 J/ψ events in the peak.

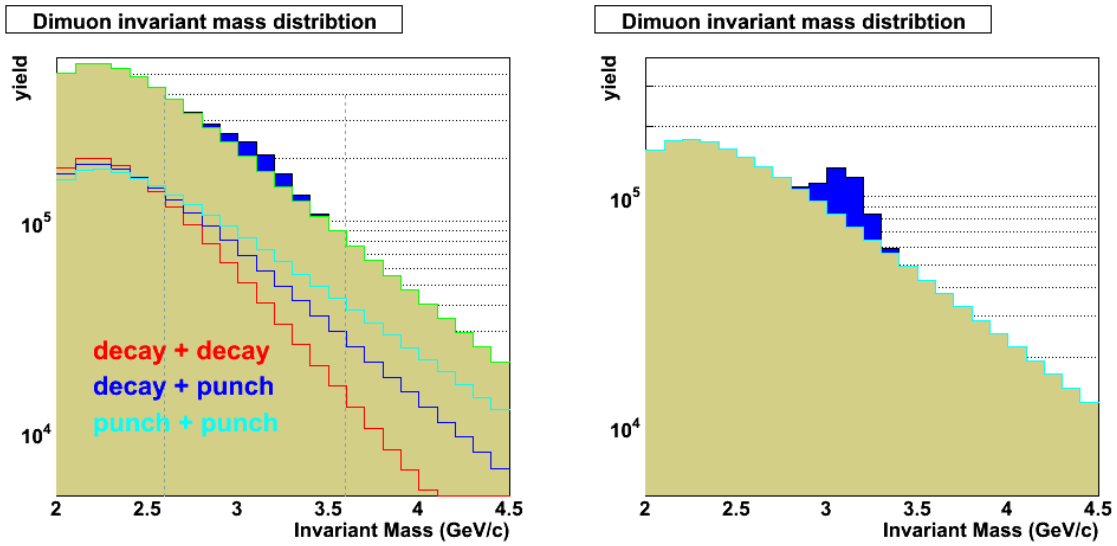

Figure 61 - Simulated dimuon mass spectrum for central Au+Au collisions before (left) and after (right) FVTX vertex cuts are applied to eliminate the light meson decay backgrounds. The mass resolution of the J/ψ is also improved from 150 MeV to 100 MeV, as shown, by the FVTX. These plots correspond to a 10 week RHIC-II run and the initial signal/noise (before the FVTX cuts) is set according to that observed in the 2004 Au+Au run. There are about 140,000 J/ψ events in the peak.

Identification of the ψ' in PHENIX has been hampered by the dimuon mass resolution and the large backgrounds. Both of these will be improved by the FVTX. The mass resolution can be improved by measuring the opening angle of the muon pair before multiple scattering occurs in the nosecone and central magnet. The resulting improvement in the mass resolution and background is shown in Figure 62 for p+p collisions, and Figure 63 for minimum bias Au+Au collisions. The improved access to the ψ' is clear for the p+p case, but for Au+Au collisions a more detailed simulation including subtraction of the remaining combinatoric background would be necessary to fully assess the quality of the Au+Au ψ' signal. Although not shown, one would expect the situation in d+Au collisions to be only slightly degraded from the rather nice ψ' signal in p+p collisions shown in Figure 62.

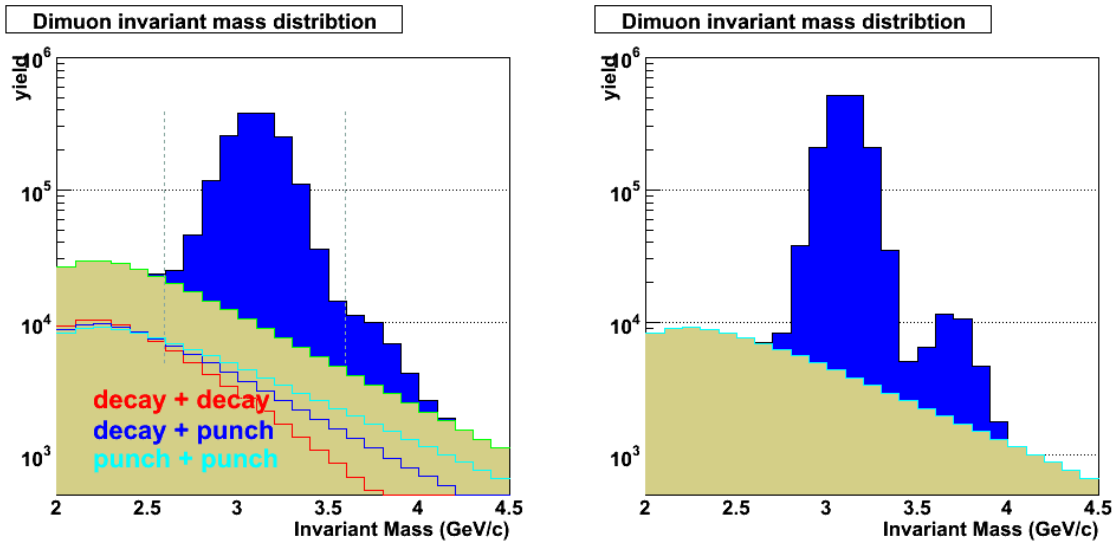

Figure 62 - Simulated dimuon mass spectrum for p+p collisions before (left) and after (right) FVTX vertex cuts are applied to eliminate the light meson decay backgrounds. The mass resolution of the J/ψ and ψ' are also improved from 150 MeV to 100 MeV, as shown, by the FVTX. These plots correspond to a 10 week RHIC-II run and the initial J/ψ signal/noise (before the FVTX cuts) is set according to that observed in the 2005 p+p run. There are about 1.5 million J/ψ and 27,000 ψ' counts in the peaks.

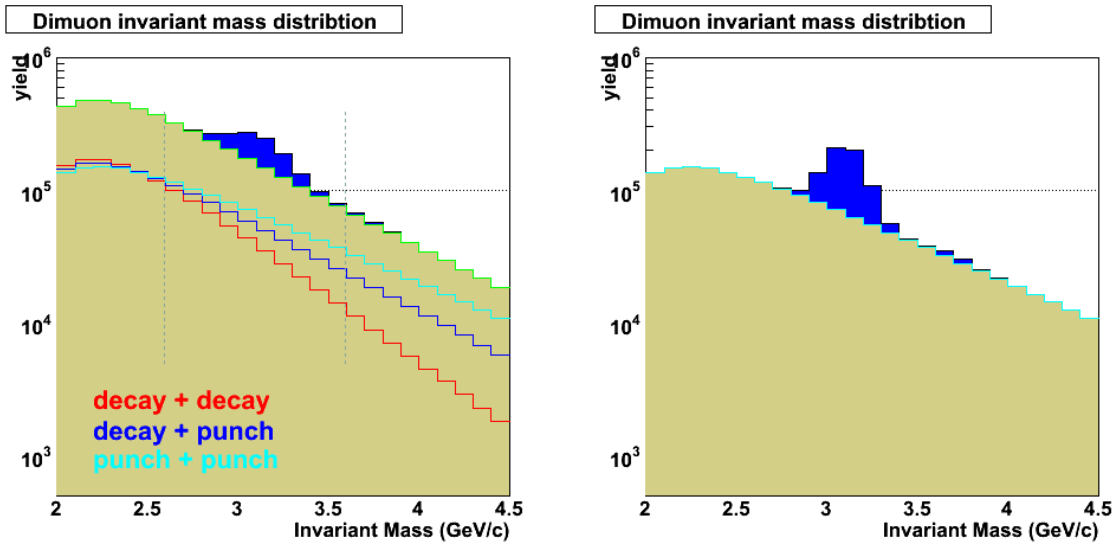

Figure 63 - Simulated dimuon mass spectrum for minimum bias Au+Au collisions before (left) and after (right) FVTX vertex cuts are applied to eliminate the light meson decay backgrounds. The mass resolution of the J/ψ and ψ' are also improved from 150 MeV to 100 MeV, as shown, by the FVTX. These plots correspond to a 10 week RHIC-II run and the initial J/ψ signal/noise (before the FVTX cuts) is set according to that observed in the 2004 Au+Au run. There are about 400,000 J/ψ and 7,100 ψ' counts in the peaks.

For the ϒ family resonances, since the mass resolution is dominated by the tracking resolution and measurements of the bending in the tracking magnetic field, are not expected to benefit much in terms of improved mass resolution from the FVTX tracker. On the other hand, like for the J/ψ the backgounds from decays of light mesons will be decreased. Also note that the ϒ family consists of three closely spaced resonances which do not appear to be well separated in present data, although this is difficult to judge given only a handful of ϒ events so far. Expectations from the PHENIX CDR were around 200 MeV mass resolution, but present resolution may be limited to more like 500 MeV. As luminosities increase we expect to be able to obtain resolutions closer to that originally expected, as shown in Figure 64.

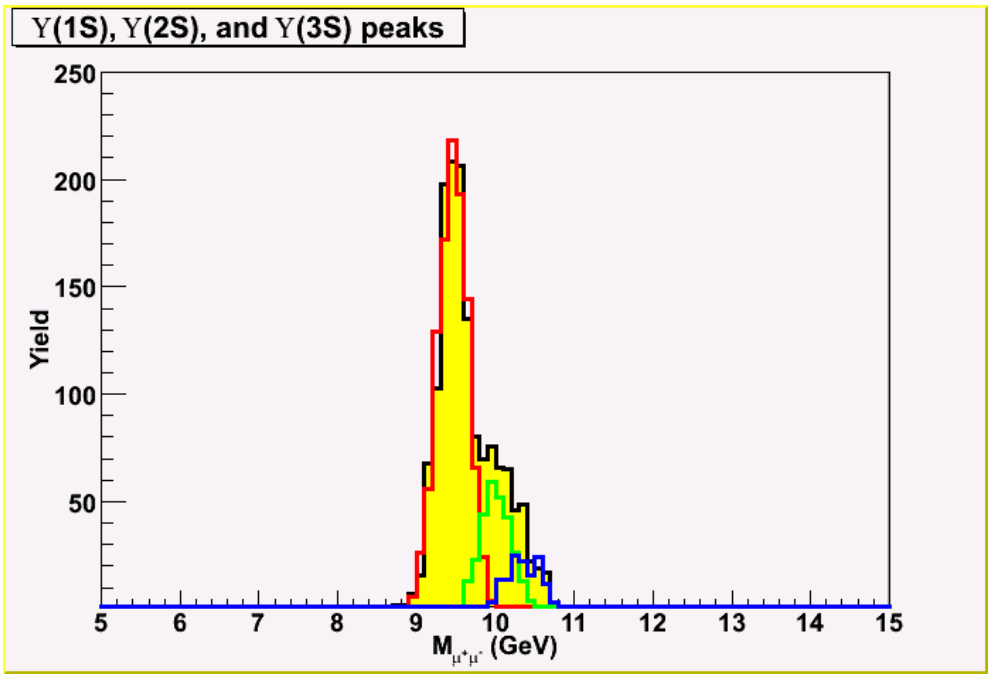

Figure 64 - Upsilon family (1S, 2S, 3S) for one week of running at RHIC-II luminosity with assumed mass resolution of 200 MeV.

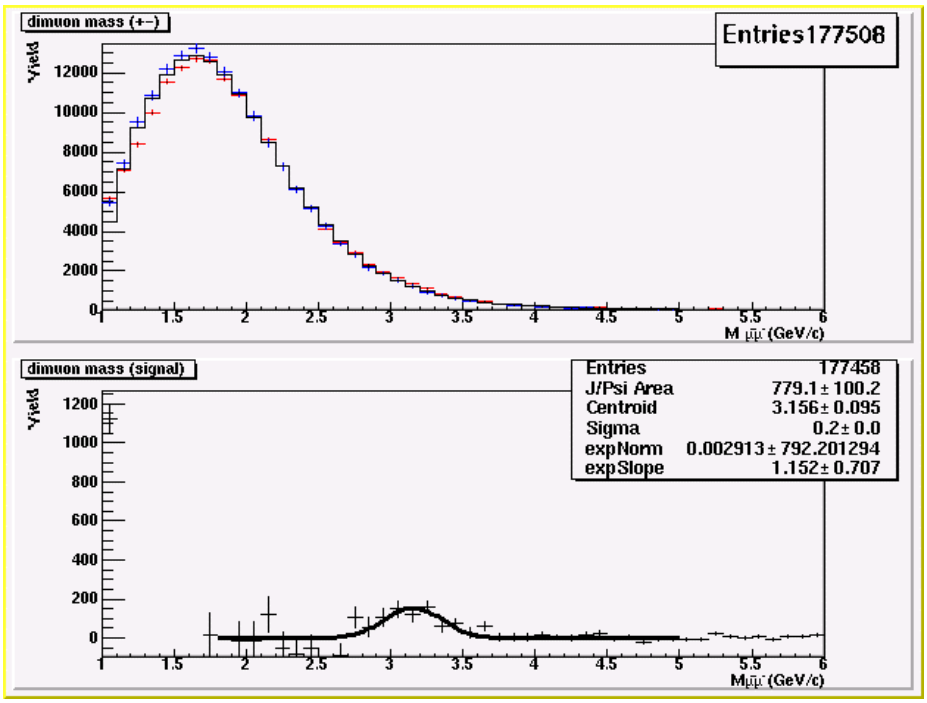

Figure 65 - PHENIX preliminary dimuon mass spectrum from 2004 for the most central Au-Au collisions. Top panel: The red histogram is for opposite sign muon pairs, while the black histogram is for smoothed like sign pairs. Bottom panel: The opposite sign spectrum after background subtraction. The peak at 3.1 GeV is the J/ψ. Note that the signal to background ration is less than 1:10.

3.3.3 Charm Pair Decays to Dimuons and Electron-muon Pairs: $D\overline{D} \to \mu^+\mu^- X$, $D\overline{D} \to \mu e X$

PHENIX has good acceptance for semi-leptonic charm pair decays. However, a direct measurement is difficult, due to the large numbers of muons from pion and kaon decays, together with the large backgrounds in the electron spectra. The FVTX, in combination with the proposed VTX (central barrel Si tracker), will eliminate most of these backgrounds. Electron-muon pairs are especially interesting, as they provide unique rapidity coverage in between the nominal muon and central arm acceptances.

3.4 Open Beauty Measurement

B meson production, while much less frequent than *D* production, is somewhat simpler to measure. The challenge is the relatively low rate. There seem to be at least two possible methods:

- Since beauty mesons have a larger lifetime than charm mesons, especially the D^0, it is possible to extract the beauty yield from the distribution of decay distances of single muons from semi-leptonic decays. Figure 66 and Figure 67 show the z decay and transverse momenta spectra fro B mesons compared to those from D mesons. As shown in Figure 67, at large transverse momentum (above about 3 GeV/c) beauty decays are expected to dominate the total muon yield, as shown previously in Figure 50.

- The decay channel $B \rightarrow J/\psi+X$ produces J/ψs that are displaced from the collision point by about one mm in Z. The FVTX can separate these from the prompt J/ψ.

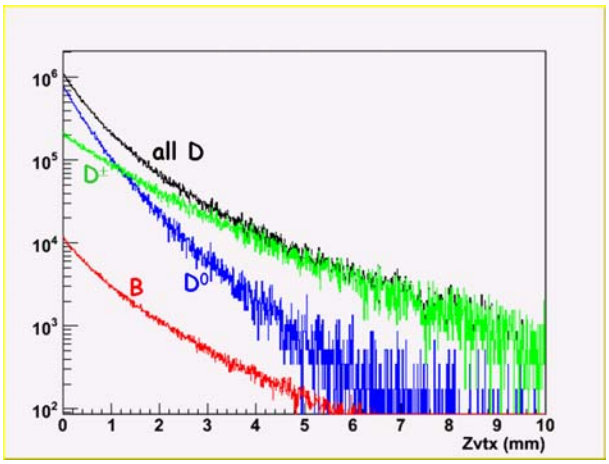

Figure 66 – The Z decay length for semi-leptonic decays of charm and beauty. The black curve shows all Ds, the green curve the charged $D^{\pm}$'s (cτ=315 μm), the blue curve neutral D^0's (cτ=124 μm), and the red curve B's (cτ=480 μm).

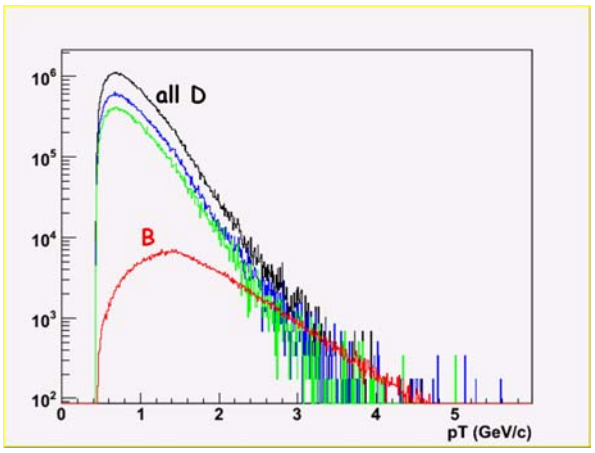

Figure 67 – Transverse momentum spectrum for charm and beauty decays. The different colored curves correspond to the same primary particles as in Figure 66.

3.4.1 B Meson Decays: $B \rightarrow J/\psi \rightarrow \mu^+\mu^-$, $B \rightarrow \mu X$

Applying a vertex cut on each reconstructed J/ψ has been used successfully to identify B-production in experiments at lower energies[1]. Since the B cross-section is larger at RHIC energies, the measurement should be easier. As the average p_T of J/ψ from beauty decays is larger than for prompt J/ψ, a p_T cut could also be used to enrich the beauty sample.

Pythia was used to simulate $B \rightarrow J/\psi \rightarrow \mu^+\mu^-$ decays. The resulting muons are tracked through the silicon and muon spectrometers using PISA. These muons have an impact

resolution of ~55 μm, significantly better than muons from D decays, due to their larger average momentum. The muon pair z-vertex resolution is ~133 μm, while the mean decay length is ~1.1mm. With a downstream pair z-vertex cut of 1 mm, 39% of the B decays are retained, while the prompt J/ψ are attenuated by a factor of 2×10^{-4}. Figure 68 shows the reconstructed Z-vertex distribution for the J/ψ from B decays as well as prompt J/ψ.

The momentum vector of the J/ψ resulting from beauty decay is correlated with the Bjorken-x variables of the two gluons that fused to create the beauty pair, just as was shown earlier for the muons from charm decays. The fitted correlations from PYTHIA are shown in Figure 69. Note that the x_2 values are much larger than for charm decays.

We have assumed a total $b\bar{b}$ cross-section of 2 μb and 4 μb for J/ψ production. The branching ratio (BR) of 1.09% for B→J/ψ has been previously measured. The total acceptance for these events into one Si Endcap is ~ 4.6%. Assuming an integrated RHIC-II p-p luminosity per week of 33 pb^{-1}, about 650 B→J/ψ events would be reconstructed after the application of a 1 mm vertex cut. For $B \to \mu X$, the acceptance is ~4.5%. The corresponding yield is ~880,000 reconstructed events. See rate details in Appendix C (Section 8). Thus, an excellent *B* measurement is possible.

3.4.2 Muon Pairs from Upsilon Decays: $\Upsilon \to \mu^+\mu^-$

PHENIX has recently reported the first Upsilon (b-bbar resonance) decay to dimuons seen at RHIC[li]. These high mass events are at forward rapidities and have both muons detected in the same muon arm, where the backgrounds are low. PHENIX can also detect upsilon decays at central rapidity where one muon goes into the north muon arm and one into the south. At present these upsilons are not observable due to large backgrounds from pion and kaon decays. The FVTX will eliminate ~60% of this background, providing a significant increase in the effective acceptance for upsilon decays. PHENIX already has a limited acceptance for upsilon decays to electron pairs, but the yields are presently too low to be useful.

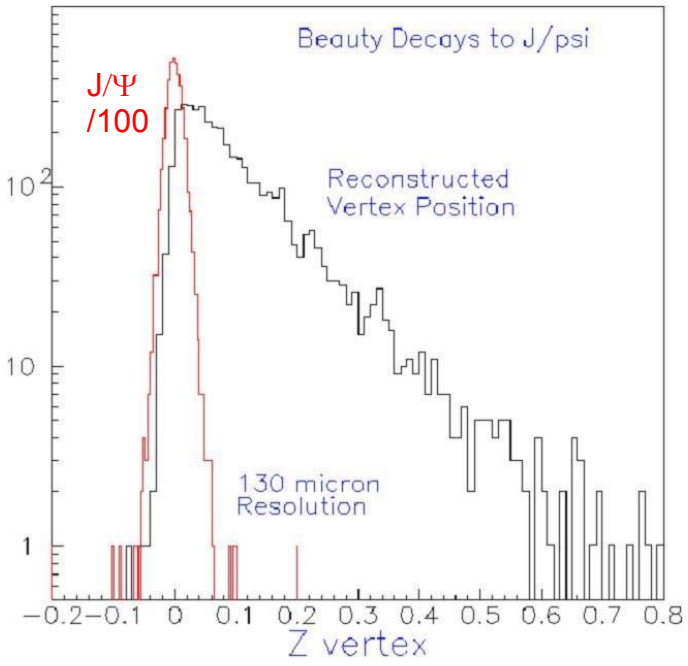

Figure 68 - The reconstructed Z-vertex distribution for J/ψ from B decays (black line) and for prompt J/ψ (red line). Note that the J/ψ yield has been scaled down by a factor of 100. The relative yield of J/ψ from B decays versus prompt J/ψ is estimated to be about 1%.

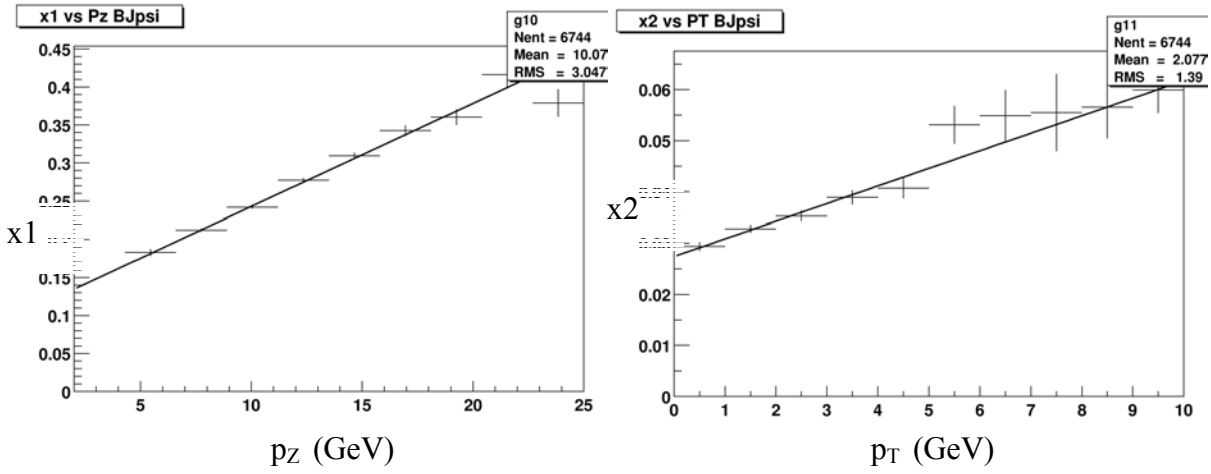

Figure 69 - Left panel: Correlation between gluon x1 and p_Z of J/ψ from B meson decays (PYTHIA simulation.) Right panel: Correlation between x2 and p_T.

3.5 Trigger Plans

An increasingly important issue as RHIC luminosities rise is to be able to capture all (or a sufficient) amount of the physics signals through the DAQ onto archival storage. The first line of attack on this issue is to use fast level-1 triggers to identify interesting physics events and make sure as many of them as possible are read out, and are not prescaled away. Estimates of the needed rejection factors beyond those from the present muon identifier based level-1 triggers are estimated in Appendix C (Section 8). Roughly they are,

Table 3 – Level-1 Rejection factors needed beyond those available from the present muon triggers.

	Single muons		Di-muons	
	p+p	Au+Au	p+p	Au+Au
2008 RHIC-I	~1/20		1	~1/5
RHIC-II	~1/100		~1/1.4	~1/40

These triggers would probably be formed by first finding tracks in various subsystem independently (muon identifier, muon trigger upgrade, FVTX, etc.), then combining these in the final stages to allow matching of tracks and use of information such as a rough momentum determination from one subsystem in the final cut decisions applied to integrated tracks from both (all) subsystems. This would be implemented on high-speed level-1 trigger boards containing state-of-the-art FPGA's.

Physics triggers that are needed include:

- $B \rightarrow J/\psi$ X where the existing muon trigger would identify a muon pair, the muon trigger upgrade would assure these tracks came from the primary vertex using its RPC pad pointing and time-of-flight information; and then this combined road would be matched to a FVTX pair which would be required to have a detached vertex ($\Delta Z_{vertex} > 0.1$ cm).
- Other pair triggers (e.g. prompt J/ψ, ψ' and Υ) could be formed by requiring a prompt rather than downstream vertex.
- Single muon D and B decays using single-track combined roads matching FVTX tracks that have detached vertices. In this case a vertex cut of 400μm < ΔZvertex < 1 cm could be made, and for the lower momentum tracks (as identified by the muon trigger momentum measurement) where the rejection might not be sufficient a momentum-dependent prescale could be applied. While at higher momentum all detached vertex tracks could be kept.
- It might also be advantageous to use the FVTX for a more efficient minimum-bias trigger in p+p collisions, where the present BBC-based trigger only achieves an efficiency of ~55%.

More details on the developing trigger plans are discussed in Appendix B (Section 7), and further discussion of the synergy of the different subsystems and upgrades is discussed in Appendix D (Section 9).

The Iowa State group is actively developing the trigger plans and associated hardware with the help of a STTR grant along with Northern Micro Design Inc.

After events are selected and passed on by the level-1 triggers, they can then be examined further by level-2 triggers implemented in a large array of parallel processors as has been done already at PHENIX. These processors can do fast reconstruction of the events including full combinations of the different subsystem information and could then make more refined cuts including mass cuts for pair triggers, or selecting high momentum tracks using the higher resolution information from the muon tracks which would only be available at level-2 and above (not in level-1). This resulting information could then be used to cut the data rate down further, or just to allow creation of filtered event streams enriched for the most important physics topics that would enable fast offline analysis for timely physics results.

3.6 Si Endcap Event Rates

The event yields in the previous sections are summarized below in Table 4. They assume an integrated p+p luminosity of 33 pb^{-1} and Au+Au luminosity of 2.5 nb^{-1}. The FVTX yields for semileptonic heavy quark decays are about an order of magnitude larger than for the VTX silicon barrel, due to the larger acceptance of the silicon endcap. The *B* decay rates would benefit most from the increased luminosity at RHIC II . Details of the rate estimates and additional count estimates for d+Au collisions and for p_T bins can be found in Section 8.5.

Table 4 – Triggered rates for RHIC-II p+p and Au+Au in one week of running. Integrated luminosities are 33 pb^{-1} for p+p and 2.5 nb^{-1} for Au+Au. The semileptonic decay rates are before application of a vertex cut.

Observable	Counts per RHIC-II p+p week	Counts per RHIC-II Au+Au week
$D \rightarrow \mu X$	~ 71M	~180M
$B \rightarrow \mu X$	~880k	~2.3M
$B \rightarrow J/\psi\ X \rightarrow \mu\mu$	~650	~1.7k

3.7 Matching Tracks from the Muon Spectrometers to the FVTX

Track matching between the Si Endcaps and the Muon Spectrometers was studied by using Hijing Au-Au central collisions in a PISA simulation. (See also 3.2) As seen in the previous table, Au-Au central collisions produce nearly two thousand tracks in the FVTX. Only a few of these particles manage to penetrate deep into the muon identifiers. Being able to correctly match the muon tracks to those found in the FVTX is of obvious importance. We envision this matching being done in stages as follows: First, tracks are found in the muon spectrometers, seeded by roads in the muon identifiers, as done in all existing PHENIX muon analyses. Second, those tracks are projected forward, through the central magnet and nosecone, into the FVTX. A momentum-dependent window is computed, based upon the expected amount of multiple scattering. FVTX tracks are found within that window. Finally, each of those tracks are joined to the muon track and fitted using a Kalman filter. The combined track with the highest probability is retained. The first two steps of this matching procedure have been studied in some detail. The Kalman fitter extension to include the FVTX hits is presently under development.

PISA was used to simulate the projection accuracy for a 5.5 GeV muon from the Station 1 of the muon tracker into the FVTX. Two types of projection are possible, based upon using either the momentum vector or position vector at Station 1. The momentum vector method results in 1.8 cm mean displacement from the corresponding hit at the last plane of the FVTX, while the position vector gives 0.45 cm. Setting the window size to a radius of 1.5 cm (for the position vector method) gives an efficiency of 99% for retaining the correct hit in the FVTX. The average pion track density at the last plane of the FVTX is 0.38 pions / cm^2 for central Au-Au collisions. Therefore, a track finding window of 1.5 cm radius typically contains about 2.7 background pions.

These pions can largely be rejected by making a χ^2 cut on the straightness of the tracks inside the FVTX. Since most of the pions have low momenta, they multiple scatter significantly in each of the four silicon planes, unlike the high momentum muons from heavy quarks decays. For example, a total χ^2 cut of 25 (referenced to the intrinsic strip width of 50 um) rejects 61% of the background, leaving only 1.1 pions in the projection window. The same cut retains ~95% of the muons above 5 GeV and ~89% of the muons above 2.5 GeV, as shown in the following table.

FVTX tracks	# of pions in a 1.5 cm radius muon track finding window	Tracks surviving a χ^2 cut of 25
Background pions	2.7	1.1 (39%)
Signal muons above 2.5 GeV/c		89%
Signal muons above 5 GeV/c		95%

Table 5 – Rejection of background pions from Au-Au central collisions using a χ^2 cut. Also shown is the fraction of signal muons that would survive the χ^2 cut.

Initial simulations including fitting of the track using the Kalman filter technique has recently been completed. With the Kalman filter it is possible to cut on the combined χ^2 of the fully fitted track. This χ^2 will include contributions from multiple scattering in the FVTX, as well as the track position and angle matches between the FVTX and muon tracker. It will also take the momentum dependence of these into account. Based on the pion rejection already available from just considering the multiple scattering, we expect that we will be able to correctly identify which of the two tracks is the muon.

Initial results for the χ^2 of the Kalman filter track in central Au+Au occupancy are shown for matching to background tracklets (black histogram) in the FVTX and to good muon tracklet (red histogram) at 3 GeV (Figure 70) or 9 GeV momentum (Figure 71). A clear distinction in χ^2 is seen between the muon tracking matches with the background tracklets in the silicon or the correct muon tracklet. If one simply picks the best χ^2 track for the match in each case one gets a efficiency for picking the correct tracklet of 93% (9 GeV muon), 83% (6 GeV muon) and 75% (3 GeV muon).

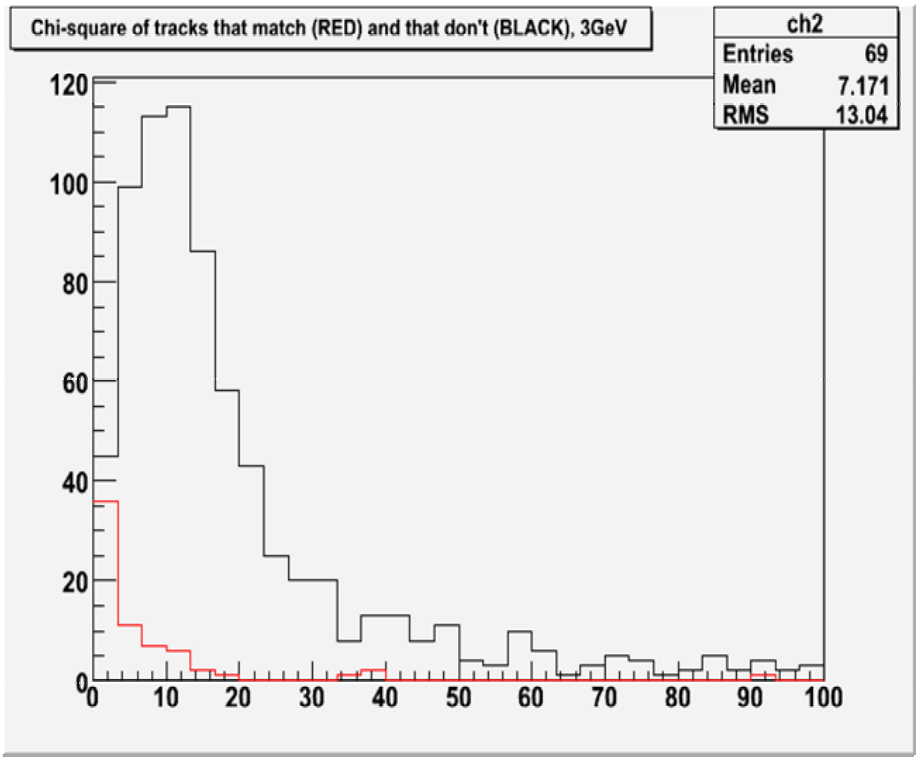

Figure 70 - Matching of 3 GeV muon tracking tracks with FVTX silicon tracks in central Au+Au collisions. The red historgram shows the Kalman filter χ^2 for the correctly matches tracks while the black histogram shows that for the soft pion background tracks. The correct FVTX track is matched 75% of the time.

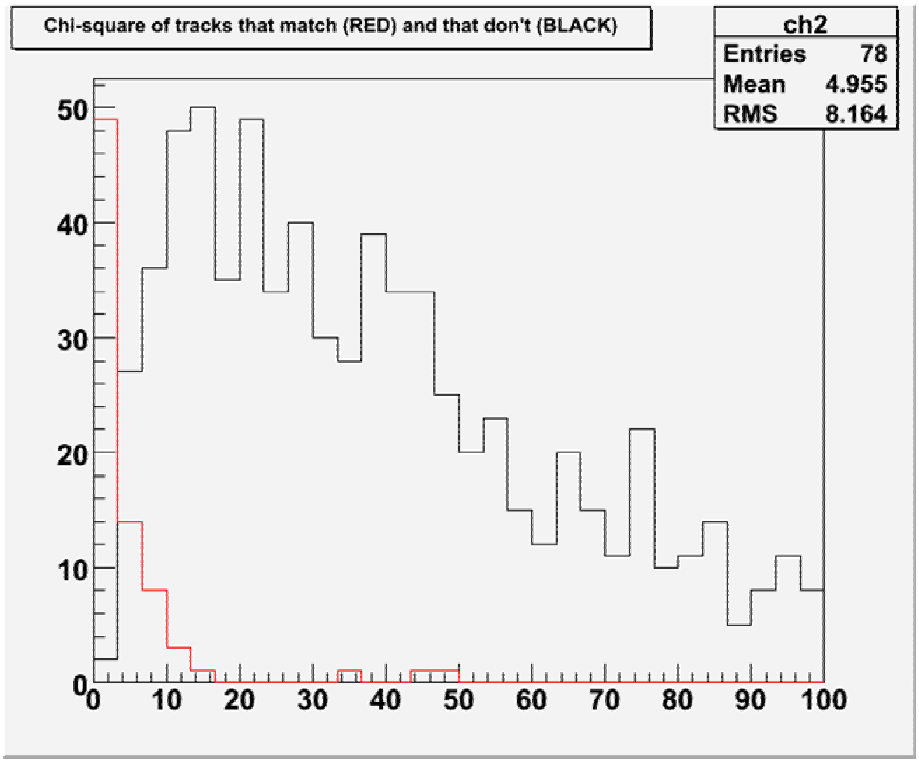

Figure 71 - Matching of 9 GeV muon tracking tracks with FVTX silicon tracks in central Au+Au collisions. The red histogram shows the Kalman filter χ^2 for the correctly matches tracks while the black histogram shows that for the soft pion background tracks. The correct FVTX track is matched 93% of the time.

3.8 Integration with PHENIX

The proposed Endcap vertex detector matches and extends the capability of the existing muon spectrometer arms. A central vertex detector for PHENIX has also been proposed and is currently being reviewed by the DOE. We are actively investigating the integration of the two detectors, both in terms of mechanical design and simulated performance. Figure 72 shows the various layers of active silicon traversed by muons as a function of the track angle (y-axis) and primary vertex position (x-axis). The crosshatched magenta region corresponds to tracks that hit all four of the FVTX silicon layers. Most of those tracks first traverse one or both of the central barrel silicon pixel layers (areas above the two blue 'pix hit' lines). Those additional hits will provide useful track confirmation for the pattern recognition, an improved impact parameter plus a precise measure of the azimuthal angle of the track, which the FVTX would otherwise only roughly reconstruct.

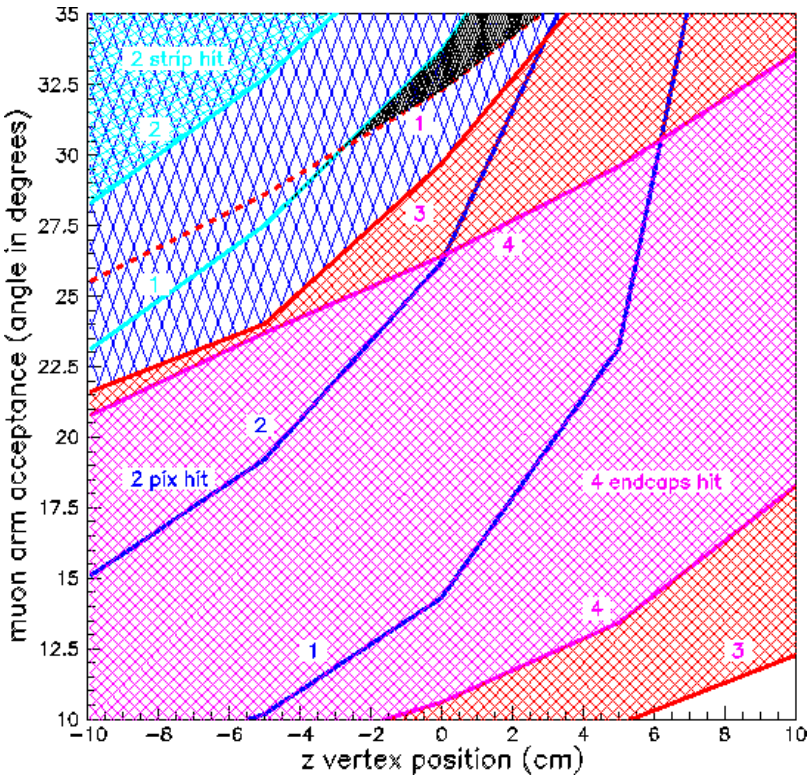

Figure 72 - Plot of vertex silicon layers hit as a function of muon track angle (y-axis) and primary vertex position (x-axis). The magenta crosshatched area includes tracks that hit all four FVTX layers (labeled endcap hits), while the red hatched area has three VTX hits. The area above the dark blue lines (labeled pix hits) indicates the number of barrel pixel layers hit, either one or two. Over much of the FVTX active area, at least one barrel pixel layer is also hit.

4 FVTX Detector system

4.1 Overview

The FVTX detector system is composed of two identical endcap sections, one in the front of the north muon spectrometer and one in the front of the south muon spectrometer. Figure 73 (and Figure 1) show a three dimensional model of the two detectors, the geometrical parameters are shown in Table 6. The VTX detector consists of a barrel region and the two endcap regions enclosed in an environmental enclosure. The environmental enclosure is needed because the barrel detector must be operated at 0 deg C. The enclosure radius is 20 cm except close to the absorbers (the nose-cone surface) where the enclosure extends out to at least 45 cm. The larger radius ends are used for the barrel pixel layer transition electronics and all of the barrel bus cables, power and cooling lines. plus all of the utilities and cables for the forward vertex system. An ongoing integration study of these utilities and cable routing is being pursued for the VTX barrel upgrade. The design of the enclosure and mechanical structure will include the needs of both the barrel and the forward upgrades. The four endcap lampshades contain 48 individual wedge shaped towers mounted on a carbon composite cooling substrate. Each wedge supports silicon sensors with readout chips flip chip assembled to the sensors, one on each side of the cooling substrate so that the acceptance is hermetic in the radial direction. In addition, adjacent wedges overlap by about one millimeter to give hermetic coverage in the phi direction. The technology for the sensors is identical to the patented p-spray ATLAS detectors with the strips oriented so that the strips nearest the beam pipe at a radius of 3.5 cm are short, ~2.0mm long in the phi coordinate, and at the largest radius of 18 cm they are about 13.5 mm long, i.e. individual strips fan out on from the center of the 7.5 deg wedge. The maximum occupancy at the inner strip is 1.5%. The total number of readout strips in each endcap is ~ 860,000. The PHX chips on each sensor are connected to a flexible kapton bus that takes the data outside of the enclosure.

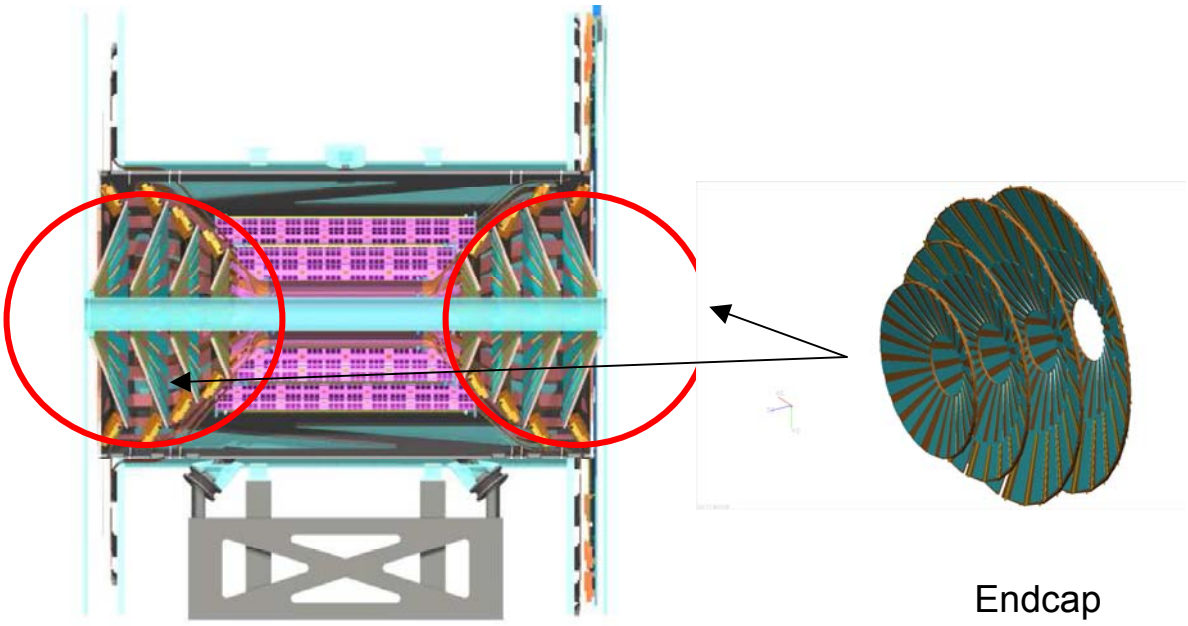

Figure 73 - 3-D model of the full vertex detector showing the barrel portion and the endcaps on left and on the right. Also shown is the VTX mounting fixture in the bottom of the picture.

Table 6 - Summary of the parameters of the FVTX disks.

FVTX	Disk	Z1	Z2	Z3	Z4
Geometrical	z (cm)	20.0	26.0	32.0	38.0
Dimensions	R (cm) inner	3.5	3.5	3.5	3.5
	R (cm) outer	10.6	14.0	18.0	18.0
Unit Counts	# of wedges	48	48	48	48
	sensors/wedge	2	2	2	2
	readout chips	6	8	11	11
	Readout Channels	147k	197k	270k	270k
Radiation Length	Sensor (300 :m)	0.3	0.3	0.3	0.3
	Readout (150 :m)	0.2	0.2	0.2	0.2
	Bus	0.2	0.2	0.2	0.2
	Ladder&cooling	0.5	0.5	0.5	0.5
	total	1.2	1.2	1.2	1.2

4.2 Silicon Readout Chip - PHX

A number of candidate chips for the readout of the endcaps were investigated, most were developed by the Fermi National Lab Electrical Engineering Department. The ASIC development group is lead by Ray Yarema. Initially we looked at the LHCb pixel chip developed for the LHCb experiment (a faster version of the ALICE chip). However, to cover the acceptance of the muon arms would have taken ~16 x 10^6 channels. FNAL Electrical Engineering Department had developed in parallel the FPIX 2.1 chip, a low-noise programmable Si pixel readout chip for the recently discontinued BTeV experiment. The chip is an advanced mixed analog/digital DC-coupled design optimized for a p-sprayed silicon detector with 50 μm by 400 μm pixels. The device has very low noise (60 electrons RMS at zero input capacitance) and high-speed readout, up to 840Mbits/. The BTeV data-push technology enables the interfacing to a level 1 type trigger with order micro second latency. Each channel has 90 uW power. Approximately 3000 FPIX2 chips have been produced in an engineering run, with a very high yield of fully functional devices. Test results are very encouraging, with the prototypes demonstrating excellent performance and minimal crosstalk. The FPIX2 and specifications are shown in Figure 74.

Advanced mixed analog/digital design
128 rows x 22 columns (2816 channels)
50 μm x 400 μm pixels
High speed readout intended for use in Level 1 trigger
Up to 840 Mbits/sec data output
Very low noise
Excellent threshold matching
DC coupled input
Fully programmable device
Output directly drives long cable (10 feet)
Rad hard to 50 Mrads

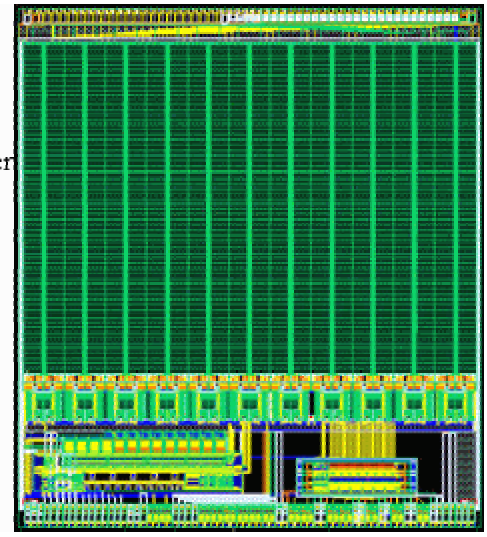

Figure 74 - The FNAL FPIX2 pixel readout chip

The electrical design of the FPIX2 chip is similar to that needed for the Si Endcap pixels. The main change required is to adapt the physical chip geometry to accommodate the Endcap sensors larger mini-strips. Ray Yarema has offered the services of his engineers and facilities to perform this work. They have already completed a conceptual layout of the modified PHX readout chip, which is shown in Figure 75.

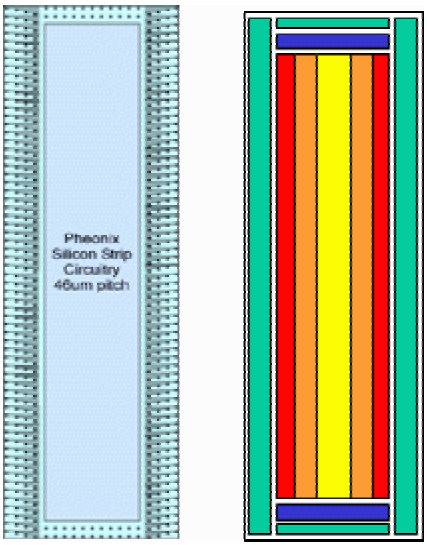

Figure 75 - Conceptual layout of the PHX pixel readout chip. The left side graphic depicts the general layout of the chip. Green is the area for bonding, blue the programming interface, red the discriminator, orange the pipeline and yellow the digital interface. The left side graphic shows the bonding layout, the bump spacing is 200 micron. The signal and power bus will be routed on the surface on the chip and bonded via the bump bonds on the ends of the chip.

The proposed conceptual design has the readout and power bus structure integrated onto the chip itself, simplifying the sensor-readout assembly process. This has never been done before since detailed simulations are needed to validate this idea. Preliminary calculations indicate that it should work. The PHX chip will be bump-bonded to the sensor, with 200 μm bump spacing. This relatively large spacing was chosen to ensure high yields during the assembly process. Yarema's team has also simulated the FPIX2 response with input capacitances corresponding to our larger mini-strips and found it to be acceptable. Design studies of the equivalent noise charge of the FPIX2 cell including the expected capacitance of our ministrips have already been done. The results are shown in Figure 76. With a nominal capacitance of the mini strips of about 1.5 pf, we would expect an ENC of 300 electrons. For a 300 um sensor (24,000 electrons for a minimum ionizing particle) this would correspond to a signal to noise of about 75 to 1. The more meaningful ratio is the signal to threshold ratio because it impacts the noise occupancy. BTeV was designed to run at a threshold of about 1500 electrons, i.e. a signal to threshold of about 16 to 1. Optimization of the PHX chip could improve these figures. The PHX chips have LVDS outputs that are designed to drive the data cables up to 30 feet.

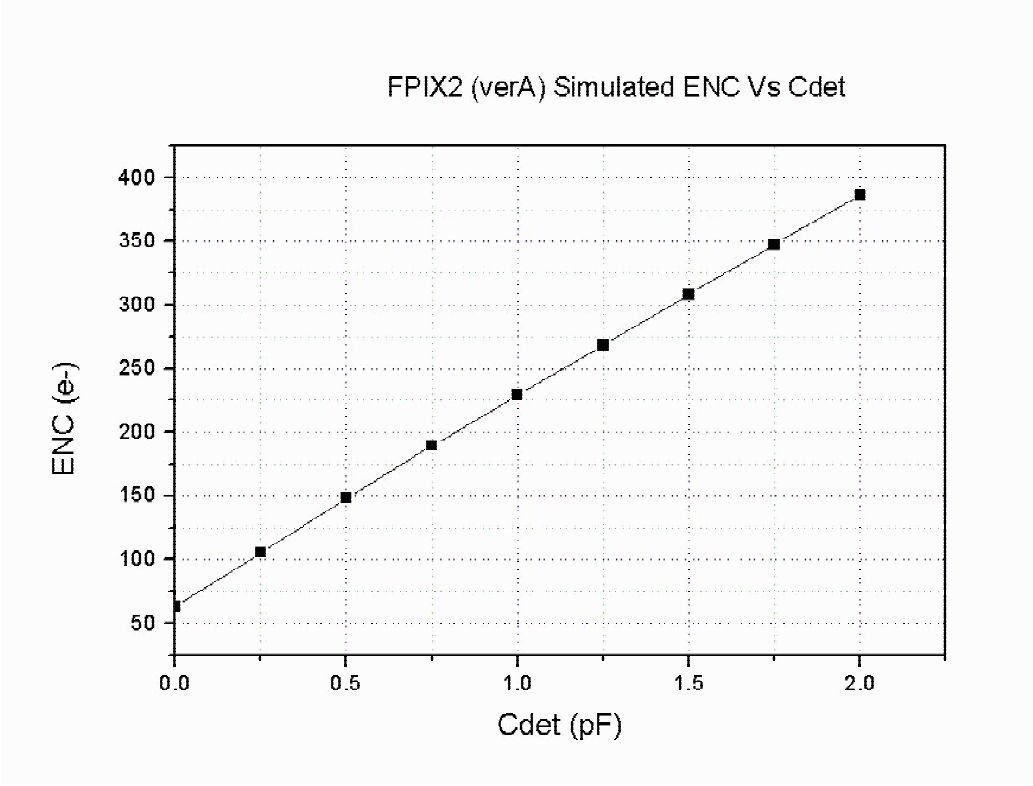

Figure 76 - The equivalent noise charge (ENC) versus capacitance.

4.3 Silicon Mini-strip Sensors

We plan on using existing technology for the silicon sensor. Pixel Sensor technology from the ATLAS and BTeV efforts will have the pixel layout (masks) modified to match the longer mini-strips that we need. The sensor technology needed for the modified PHX chip is the n^+ on n concept. The pixels consist of n^+ - implantations in high resistivity n type silicon while the pn-junction is located on the sensor's backside surrounded by a multi guard ring structure. An advantage of this type of sensor compared to the standard p^+n – sensors is that it can be operated partially depleted - if full depletion cannot be reached anymore due to radiation damage. Also, it keeps the side close to the pixel chip to be held at ground potential thereby eliminating potentially disruptive discharges between the sensor and chip. Developing the masks for this effort will be done in concert with the vendors of the sensors. Lengthy and costly R&D for the sensors is not necessary. The material and electrical specifications for the BTeV sensors are listed below.

MATERIAL SPECIFICATION:

Wafer diameter	4 inches (100mm)
Crystal orientation	<100>

Thickness	250 μm +10 □m –20 □m
Uniformity (across wafer)	< 10 μm
Wafer bowing after processing	< 50 μm (sagitta)
Doping of starting material:	n-type
Resistivity:	1.5 -2.5 KΩ cm
Uniformity of resistivity (wafer to wafer)	±25%
Oxygenation:	The wafers need to undergo an oxygen thermal diffusion process for 24 hours at 1150C
Polishing:	Double sided
Passivation:	Covering both sides except for bond pads (both bump and wire bond pads) and reference marks. It can either be silicon oxide or silicon nitride.

DESIGN PARAMETERS

- Devices shall be n^+ pixels on n substrate using "moderated p-spray" as the n-isolation technology. Note: *This is covered by a Non-Disclosure Agreement with six institutes in the ATLAS collaboration and three patents held by Garching Innovation.*
- The full design for the masks will be provided by us in electronic form (GDS-2 file)
- Vendor will finalize the design details according to their design rules and process, and will work with us on the final design and mask layout. Any proposed change to the design must be approved by the BTeV pixel group.
- Mask alignment precision within the same side : ±2um
- Mask Alignment precision between front and back side: ±5um
- Processing parameters shall be the same as for the ATLAS production moderated p-spray detectors (as covered by the Non-Disclosure Agreement and patents mentioned above):

Front Side (n-side)

1. N-implantation:
   - minimum width 5 μm
   - minimum spacing 5 μm
2. P-implantation "moderated p-spray":
   - minimum width 5 μm
   - minimum spacing 5 μm
3. Contact holes in oxide:
   - minimum diameter 5 μm
   - minimum spacing 20 μm

4. Metal:
    - minimum width 8 μm
    - minimum spacing 5 μm
5. Contact holes in passivation:
   - Minimum diameter 12 μm
    - minimum spacing 40 μm
    -

Back Side (p-side):

1. p-implantation:
    a. minimum width 5 μm
    b. minimum spacing 5 μm
2. Contact via in oxide (or nitride):
    a. minimum diameter 5 μm
    b. minimum spacing 10 μm
3. Metal:
    a. minimum width 8 μm
    b. minimum spacing 5 μm
4. Contact via in passivation:
   - minimum width 50 μm
   - minimum spacing 100 μm

Three different silicon sensors of trapezoidal shape are used to tile the active areas of the Si Endcap, as shown in Figure 77. Also shown is the arrangement of the readout chips on each of the sensors. The largest sensor is 79 mm high and 27 mm wide at its large end. Six PHX chips are used to readout the 3072 mini-strips. The smaller sensors contain 2560 and 1536 strips, respectively.

The Si Endcap detector layers are assembled as shown in Figure 78 through Figure 80. First, the sensors are tiled on carbon wedges that serve as the support and cooling structure for each of the sector assemblies (Figure 78). Next, 24 sectors are joined to form each of the four stations (Figure 79). Finally, the four stations are assembled for each Si Endcap detector (Figure 80). Each Endcap contains approximately 860,000 strips.

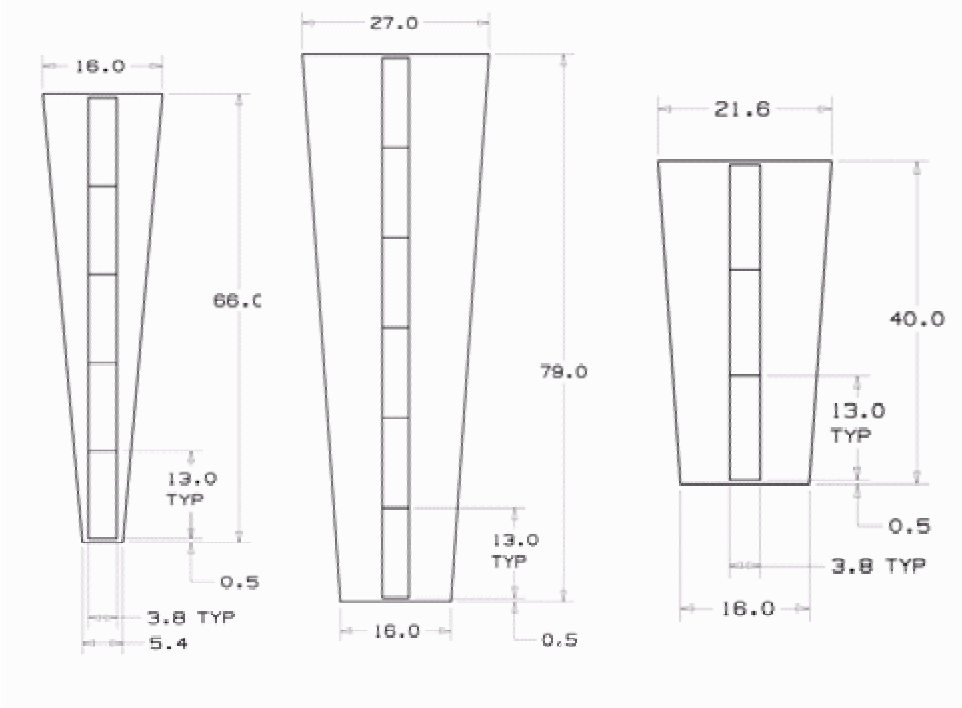

Figure 77 - Three silicon detector sizes will be used. The largest will have 6 chips reading out two rows of 1536 strips, the intermediate silicon will have 5 chips reading out two rows of 1280 strips and the smallest silicon is half the size of the largest with 3 chips reading out two rows of 768 strips. (All dimensions are in millimeter)

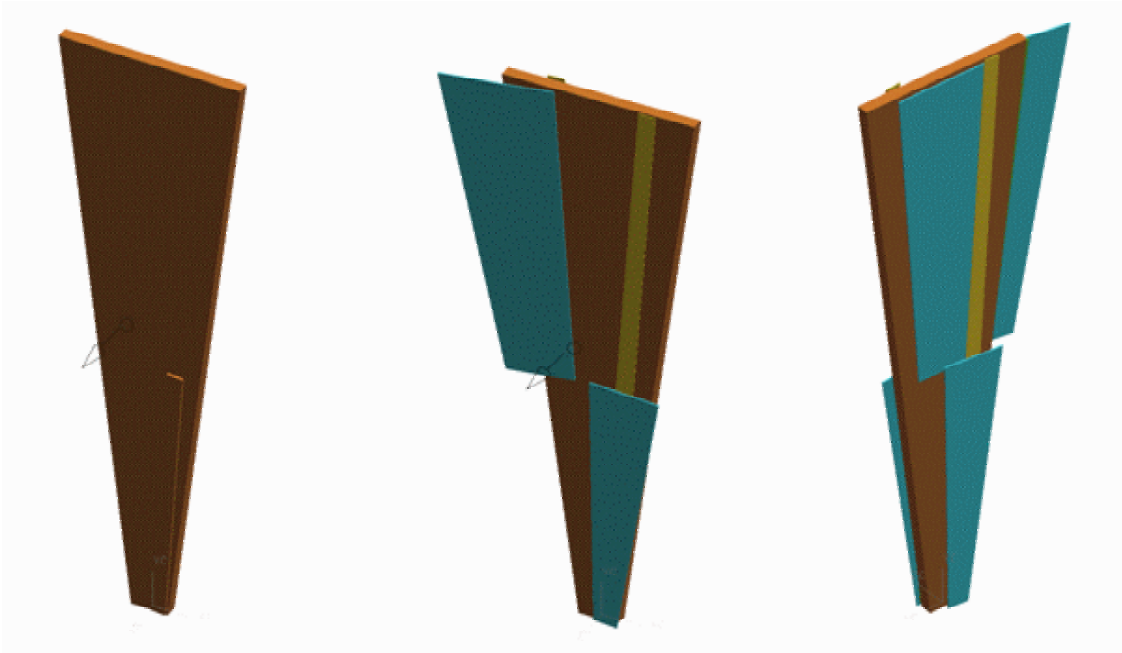

Figure 78 - A wedge assembly will have 24 carbon panels (one shown here in brown) in azimuth, each of them carrying 4 silicon detectors (blue), two in the front and two in the back. They overlap on the edges by a few millimeters to avoid dead areas. The bus on a silicon assembly is routed on the chips as described above, the connection of the inner silicon detectors is realized via a kapton bus (golden).

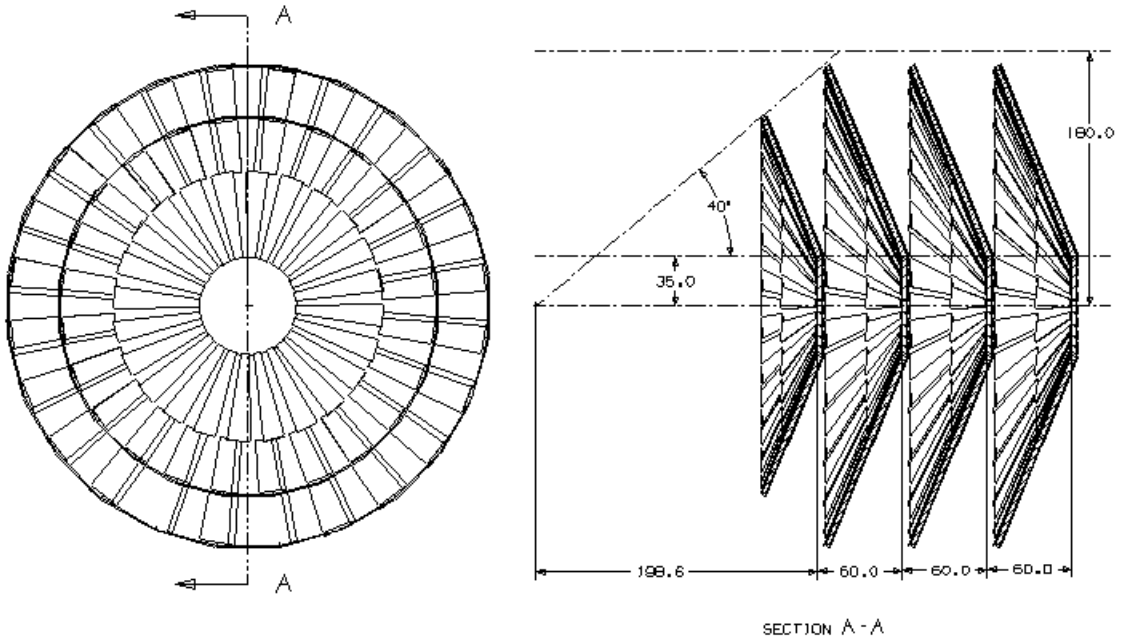

Figure 79. Each station carries 24 wedges, i.e. 96 silicon detectors. The stations are placed at ~20, 26, 32 and 38 cm from the interaction point.

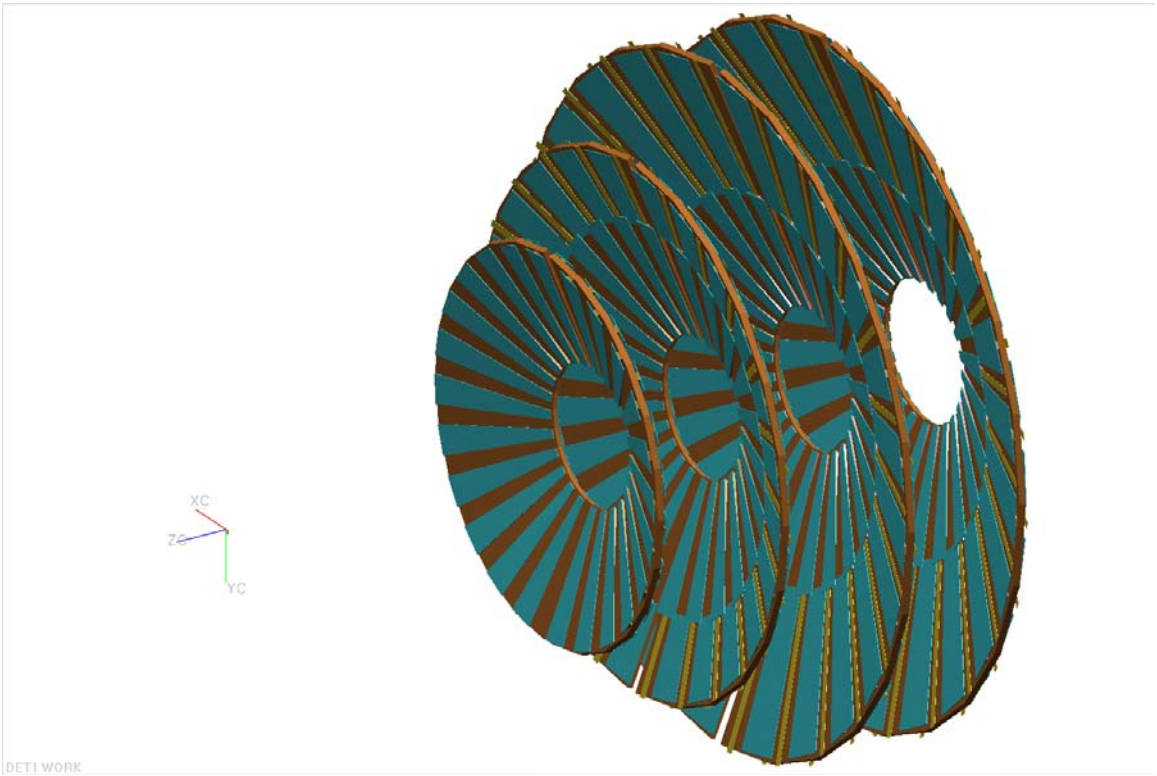

Figure 80. Each endcap will have 4 stations of silicon detectors. The inner station has a reduced size in order to not interfere with other PHENIX detectors.

4.4 Electronics Transition Module

The electronics transition module will take the continuously streaming data (data-push) from the PHX via flexible cables, buffer the data for 64 beam clocks (emulating the 64 beam clock analog buffer of current PHENIX detectors), grab the data from the appropriate beam clock upon a Level-1 trigger and reformat the data before it is sent to the PHENIX DCMs. A possible data buffering concept proposed by Dr. C.Y.Chi, Columbia University, and M.L. Brooks, LANL is shown in Figure 81. The PHX data with the beam clock counter is routed by an FPGA chip to one of 64 buffers corresponding to the beam clock number. The FPGA than allows the data from the appropriate beam clock to be sent to a Level 1 trigger (currently under development by Iowa State University) or to the DCM if a LV1 trigger accept is received. The existing PHENIX DCMs can be used without modification. The time to pass all of the data to the Level 1 trigger is expected to be less than 1 us.

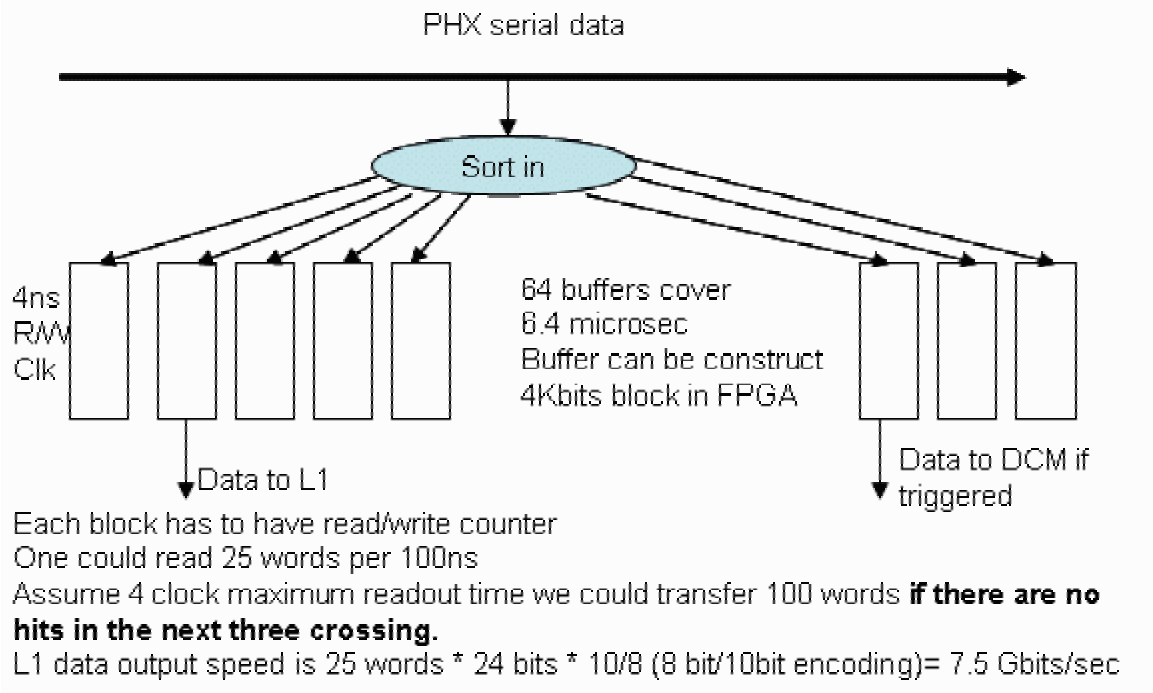

Figure 81 - The transition module concept proposed by Columbia.

The buffering requirements of the transition module are expected to be quite modest with <50 kbits of data expected in Central AuAu events for up to 44 chips serviced by the same FPGA. The tracks in the central region are approximately straight, i.e. a track typically intersects 4 wedges that are located behind each other. Thus 4 stations with 11 chips each is a natural choice of segmentation. Noise hits are expected to take even less space. The readout time is expected to be less than 4 beam clocks for Central AuAu events, as we plan to use at least two readout lines per chip. Some calculations of data sizes and readout times can be found in Table 7, for various options of readout lines, chip "ganging", and assuming the readout clock is synchronized to give an integral number of beam clocks needed per data word.

Layers Ganged	chan/ chip	chips/ board	chan/ board	Occup ancy	Real Hits/ 64 Clocks	Real data size /64 clks (kbits)	Noise	Clks	Noise Hits/ 64 Clks	Noise data size/64 clocks (kbits)	Buffer for 64 clocks (kbits)	# of Read Lines	Readout Time (ns)
1	512	11	5632	0.015	84.48	2.03	0.001	64	360.4	8.7	10.7	1	212.4
4	512	44	22528	0.015	337.92	8.11	0.001	64	1441.8	34.6	42.7	1	212.4
1	512	11	5632	0.015	84.48	2.03	0.001	64	360.4	8.7	10.7	2	106.2
4	512	44	22528	0.015	337.92	8.11	0.001	64	1441.8	34.6	42.7	2	106.2
1	512	11	5632	0.015	84.48	2.03	0.001	64	360.4	8.7	10.7	4	35.3
4	512	44	22528	0.015	337.92	8.11	0.001	64	1441.8	34.6	42.7	4	35.3
1	512	11	5632	0.015	84.48	2.03	0.001	64	360.4	8.7	10.7	6	35.4
4	512	44	22528	0.015	337.92	8.11	0.001	64	1441.8	34.6	42.7	6	35.4

Table 7 - Buffer requirements for the transition module for most challenging case of AuAu events, various options of readout lines/chip, different levels of chip "ganging", and a extremely conservative noise estimate. In addition the time to readout an event is given for the same conditions.

4.5 Mechanical Structure and Cooling

The mechanical structures and cooling are part of the integrated design of the barrel and endcaps. The majority of the support structure will be designed as part of the barrel effort and remaining issues concerning ladders and cooling specific to the endcaps will be part of this proposal.

A conceptual design of the silicon vertex detector was commissioned by the LANL group to HYTEC, Inc. HYTEC provided the mechanical designs for the ATLAS silicon pixel group and has 15 years of design experience with silicon vertex detectors. For PHENIX they have also designed the station-1 muon detectors and the station-2 spider and they also did the finite element analysis for the station-3 octants. The VTX mechanical conceptual design was completed and a report written. Recently, in September 2005, the original concept was reanalyzed to incorporate changes that have occurred over the past 2-½ years, a report was issued in October 2005. We summarize the results of both reports:

For the internal support and cooling of the VTX and FVTX detector, the major results of the conceptual design are:

- The use of sandwich composites will satisfy the radiation length requirements and provide the required stiffness.
- The outer frame structure should be a single diameter encompassing both the barrel and end-caps.
- The modular clamshell design can satisfy the stability requirements provided the connection issues are studied further.
- An octagon arrangement is suggested to facilitate utility routing and fabrication.
- Structural end disks at either end of the structure are recommended to prevent

deformation
• The ladders should have a simple support at one end and floating support at the other end to minimize thermal strains

The R&D issues identified are:
• Building prototypes of ladder assemblies to verify calculations.
• Building full-scale prototype to test static and dynamic stiffness.
• Develop connections of modules.
• Develop support design.
• Refine calculations and develop full concept for 0 deg operation.

4.5.1 Design Criteria

The goal of the study was to establish a feasible design and to identify outstanding design issues. The study was based on a preliminary list of design requirements and a straw-man layout of the detector structure. To adequately address all structural and mounting issues, a fully integrated design, which includes the barrel detectors and future end-caps extension, is needed. This design needs to address all integration issues not only for the barrel and the end-cap vertex trackers, but also with other potential PHENIX upgrades.

The design requirements of the conceptual study were,
• Modular Design
  - o End-caps detectors can be mounted independently at a later time
  - o Support structure separated vertically into two half shells
• Detector Coverage
  - o Hermetic design
  - o Four barrel layers
  - o Four end-cap layers in each forward section
  - o Fiducial volume < 20 cm radius, z < 40cm
• Radiation length goal < 1% per layer
• Room temperature operation desirable, 0 deg Celsius if needed
• Dimensional stability < 25 microns

4.5.2 Structural Support

The selection of materials for the support structure is based upon the above criteria where the most important material properties are low radiation length, low density, high stiffness, and availability. Out of three candidates (i) beryllium, (ii) graphite fiber reinforced plastic (GFRP), and (iii) Carbon-Carbon, the GFRP was chosen for the study because of its wide availability, works well in sandwich composites, and has good radiation length and strength properties. The GFRP is still the material of choice.

4.5.3 The Enclosure and Environmental Envelope

The original conceptual design was for room temperature operation. Because of the requirement for 0 deg operation, we now need to include an environmental enclosure. Shown in Figure 82 is an isometric view of this new design. The original concept was for an octagonal structural enclosure uniform in outside radius and this is retained. Added is the new environmental enclosure to contain the dry gas.

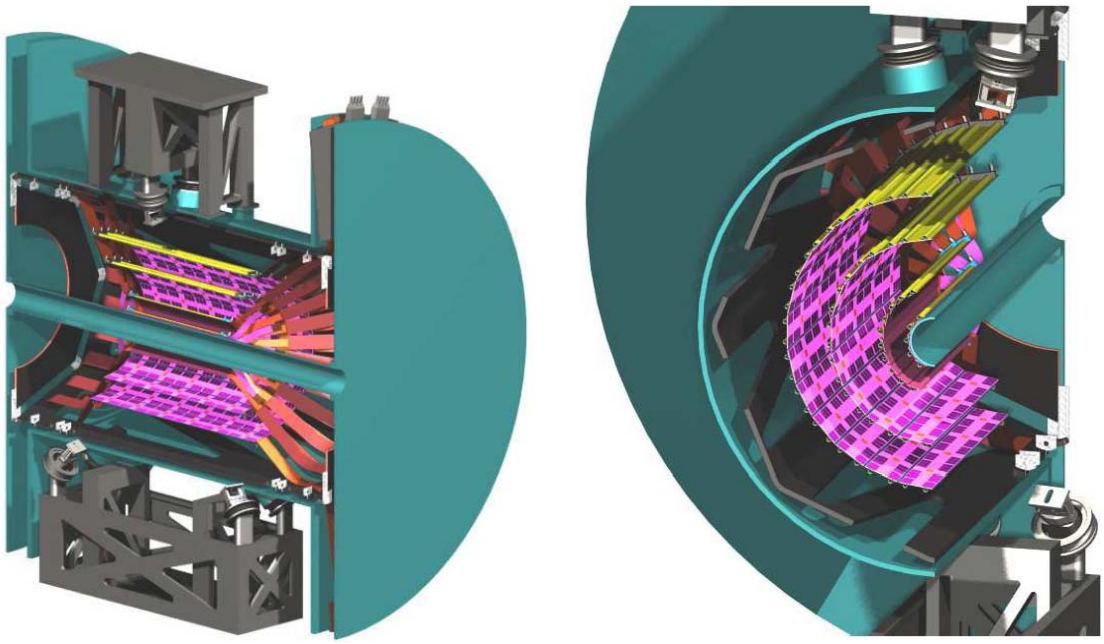

Figure 82 - An isometric view of the VTX showing all of the internal features coaxial with the beam tube: (moving out from the beam tube), two cylinders of pixel detectors, two cylinders of strip detectors, the GRFP structure (gray in color), and finally, the cylindrical enclosure wall.

4.5.4 Endcap Ladder Structure

The forward regions consist of 4 conical arrays of ladder modules tilted from the normal to the beam pipe by 22 deg. Conceptually, we have chosen a flat octagonal panel structure with sensors and electronics mounted on either side of the panel so that we can achieve hermetic coverage. Figure 83 shows this arrangement on the left and an octagon panel structure on Figure 84.

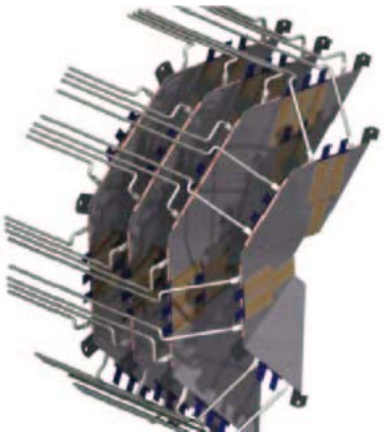

Figure 83 - 3D model of octagonal disk like structures for the endcap ministrips. Cooling tubes are to demonstrate both the number and routing.

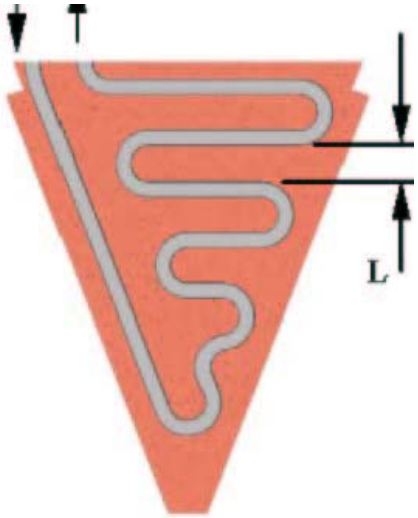

Figure 84 - The octagon panel structure is on the right with the cooling channel shown. A heat load of 0.1 W/cm2 is assumed.**

The original concept was designed for a modified LHCb chip with a total heat load on each endcap of approximately 450 W, or about 15W per octant panel. The new PHX chip has a heat load of 90 uW per channel so the total for each end cap now is ~70 W or 2.2 W per octant panel. This much lower number indicates that convective cooling might be possible. In comparison to the barrel this is a very small heat load and greatly simplifies the removal of heat. The octant panel structure consists of a composite sandwich of C_C facings on either side of a carbon foam in which is embedded an aluminum cooling tube (Figure 85). Thermal and gravity sag calculations were performed in a manner similar to those discussed in chapter 4 and no serious distortions were observed. For the case of 0 deg Celsius operation, more work is necessary.

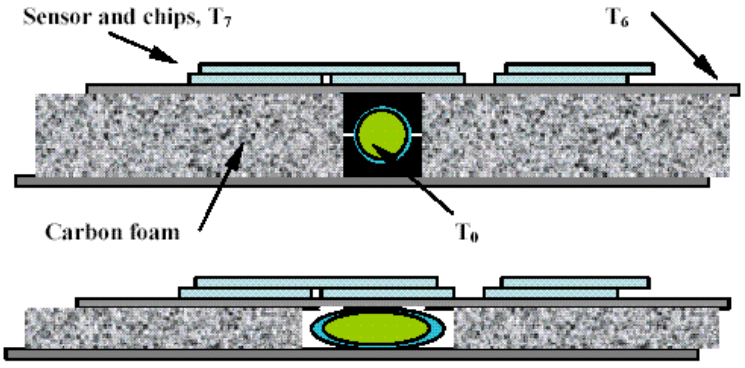

Figure 85 - Illustration of an embedded cooling passage arrangement in the composite sandwich used in the endcap thermal and static calculations. The upper panel depicts a circular tube with supports and the bottom panel shows a flattened tube that enhances heat transfer and provides a thinner sandwich.

4.5.5 Radiation Length

The thermal and static design studies produced a range of solutions for the endcaps. Figure 86 shows the radiation length estimate for different cooling tube dimensions. The parameters used in the calculations are:

- Al tube, 200 micron.
- 4 mm carbon foam separator.
- Tube support 2 mm wider than tube diameter.
- Sandwich facings of 400 micron.

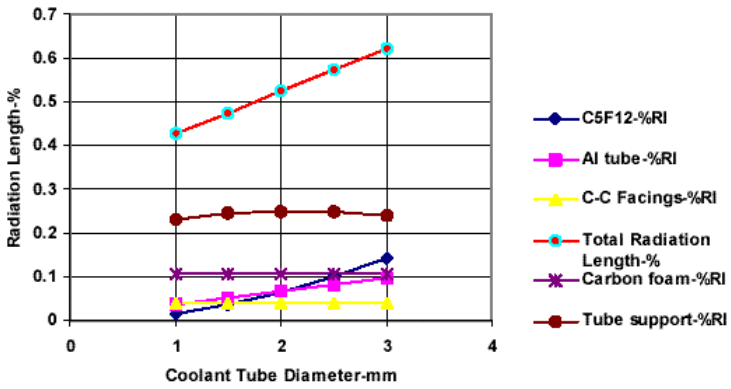

Figure 86 - Estimated normal radiation length for the endcap octant panel for different tube diameters.

4.6 Endcap Analysis Summary

The conceptual design studies revealed the following:

- Single phase cooling is well suited to the endcaps.
- Two adjacent octant panels can be cooled in series thus reducing service connections.
- 2mm cooling tubes and panel thickness are adequate.
- The radiation length of the octant panel exclusive of sensor and electronics is ~ 0.6 %.

The R&D issues consist of refining the calculations, designing attachment points to the main support structure, and prototyping the octant panels.

5 R+D Schedule, Responsibilities and Budget

5.1 R+D Areas

The R&D associated with the endcaps involves modifying the topology of the PHX chip, developing the interface between the PHX chip and the existing PHENIX DCMs,

modifying the design of an existing sensor, developing the wedge structure, and developing the bus and flex cable. The data interface is the most involved of the R&D projects. The rest are starting from existing technology or use standard commercial concepts. The R&D for the endcaps will be supported at LANL and BNL. At LANL we will complete the R&D for the interface, the mechanical support and ladder, and the sensor design. BNL will support the R&D for the PHX design and modification. All activities will begin in FY2006.

5.1.1 PHX

The PHX chip is a modification of the FPIX 2.1 pixel chip used for the BTeV experiment. The modifications take it from a 22 column x 128 row structure to a 2 column x 256 channel structure. The R&D issues involve optimizing the front-end for the mini-strips, designing the built-in bus structure and incorporating the redesign of the digital section to be identical to that in the FSSR chip. The novel R&D issue is the integral bus and will be addressed first.

5.1.2 Sensor

The sensor will be identical technology that is used in the BTeV sensor design, which is the same as that used in the ATLAS pixel detector. We have obtained the design specifications for this sensor. We will produce new drawings for the 2 column, ministrip layout. The significant R&D will be to design into the sensor the small bus extension for the daisy chain from one chip to another.

5.1.3 Interface

The interface board that will connect between the PHX chip and PHENIX DCMs will need to provide the following functions:

- Provide buffering of the continuously streaming data from the PHX chips for 64 beam clocks, and this buffering must be adequate for everything from pp running to central AuAu events
- Upon a lvl-1 accept, retrieve the data from the buffer for the appropriate beam clock and package it into a format acceptable by the DCM
- Pass beam clock to the PHX chip, assure sychronization
- Provide an interface to download initialization settings to the PHX chips
- Perhaps provide ability to reset PHX chip(s)

We expect the board design to be not too much different from a number of other PHENIX interface boards, containing one or more FPGA to handle the data buffering and packaging and I/O lines to PHENIX T+FC, DCM, ARCnet (or equivalent) and to the PHX chip readout lines. The FPGA code development will take several months, as has

been standard for PHENIX. We are hoping that we can begin development on the code even in the absence of the final PHENIX interface board as we already have an FNAL-designed Xilinx FPGA board which can nominally provide all the I/O lines needed to develop the code that has the needed functions. We have organized a team with members from Columbia, Iowa State and LANL to address this portion of the project.

5.2 Schedule

The schedule for the FTVX project is shown in Figure 87. Included in the schedule is the R&D timeline. We have assumed R&D money begins in the second quarter of FY06 and construction funds begin in the first quarter of FY08. Task durations are based on previous experience of the engineering teams and quotes. The total project duration is due primarily to the sensor and PHX R&D and procurement times.

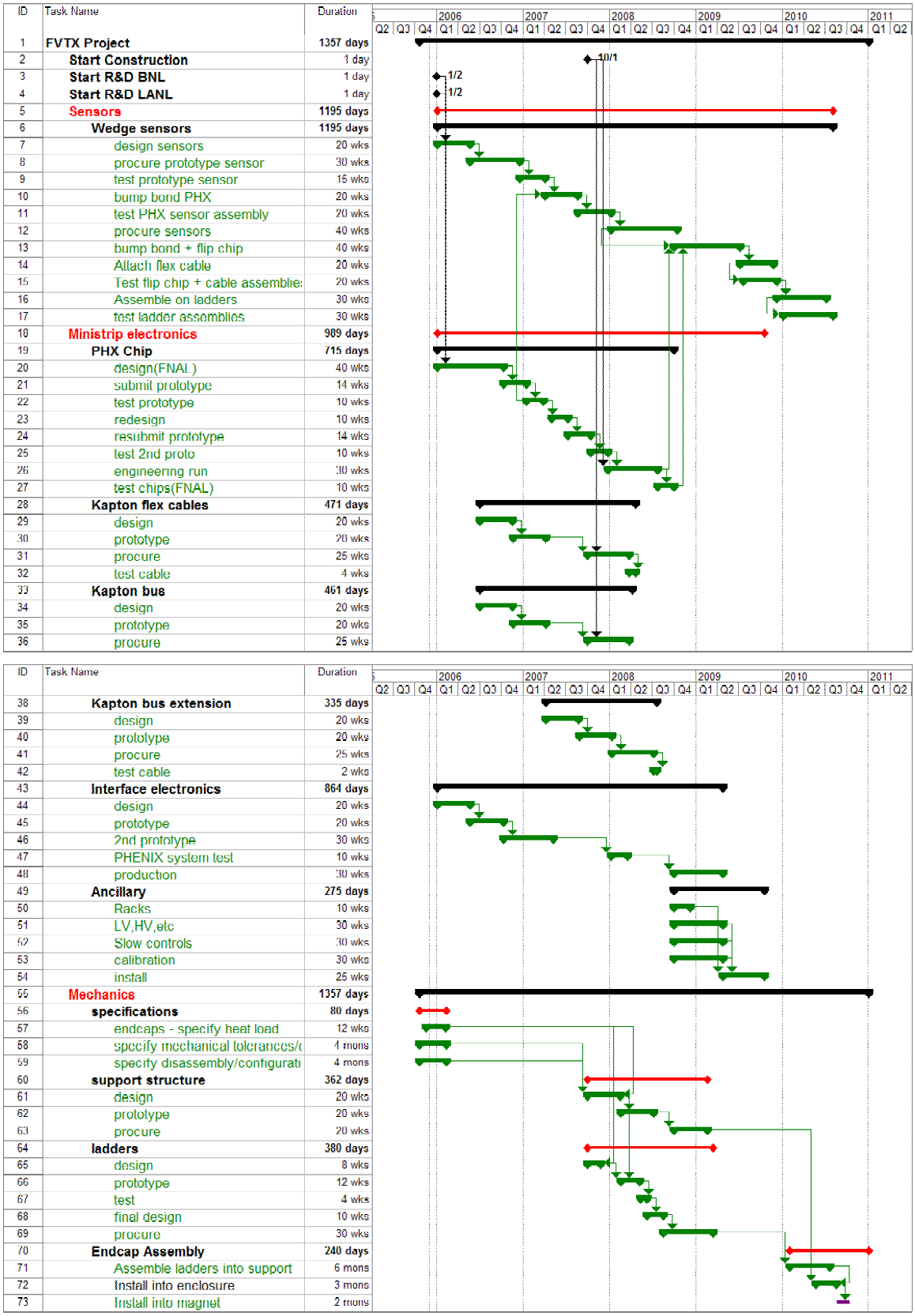

Figure 87 – PHENIX Forward Silicon Vertex (FVTX) project timeline.

5.2.1 Cost

Since the FVTX will be added to the existing barrel vertex detector, VTX, much of the needed infrastructure, cooling, enclosure, cable routing, installation procedures, etc. will already have been done and be in place. In this cost estimate only those items needed for fitting the FVTX into the VTX enclosure are considered. The costs in Table 8 are generally obtained from cost estimates by the engineering team who will be doing the work and from cost estimates for work already done by those teams. For example, the cost estimate for the PHX chip came from the FNAL engineers who designed the FPIX2 chip. The HYTEC engineering team previously designed the ATLAS pixel mechanical structures and that forms the basis for the mechanical cost estimates. The cost basis for the sensors are from quotes from ON Semiconductor Inc. in Prague, Czech Republic and CIS Semiconductor obtained in Nov. 2005 and on drawings of the wafers with the FVTX wedges (Figure 88) The contingency analysis method is listed in Appendix A (Section 6).

Forward Endcap Cost Estimate - FVTX					Tech	Cost	Schedule	Design	Weight	total	Cost with
2 endcaps	R&D BNL(k$)	R&D LANL(k$)	Construction(k$)	comments	Risk	Risk	Risk	Risk		contin	Continger
Mechanical ladder and support structure	55	50	224	HYTEC Estimate	4	4	4	4	2	0.24	277.76
Assembly jigs			20	engineering estimate	4	4	4	4	1	0.16	23.2
Silicon Sensor		50									
purchase			388	CIS and ON quotes, 10% spare, 60% yi	8	2	8	4	2	0.32	512.16
setup and masks			12	CIS and ON quotes	4	2	4	0	1	0.1	13.2
dicing			20	$ 100 wafer	4	8	8	0	1	0.2	24
sensor Q/A and testing			50	University students + engineer	4	4	4	0	1	0.12	56
PHX chip, tested	440										
engineering run			348	FNAL estimate	8	4	4	0	2	0.28	445.44
testing			60	FNAL tech	4	4	8	0	1	0.16	69.6
bump bond chip to sensor			423	Btev experience, $75/chip	8	4	8	0	2	0.32	558.36
Inteface - phx to DCM, CHI+MB concept		200	300	$500 for 400 units,arcnet $40k,engineeri	8	6	4	15	2	0.47	441
DCM,fibers,TFC fanout,..			150	existing designs	4	4	4	0	1	0.12	168
slow controls			50	existing designs	4	4	4	0	1	0.12	56
calibration system			20		4	4	4	0	1	0.12	22.4
Assembly and test ladders			200	FNAL techs	4	6	4	0	2	0.24	248
Assemble ladders in frame			100	techs and students	6	6	4	0	1	0.16	116
Electronics Integration			250	Engineer	4	6	4	0	2	0.24	310
Mechanical Integration			250	Engineer	4	6	4	0	2	0.24	310
power supplies, distr. Cards ,cables			100	VTX designs	4	4	2	4	1	0.14	114
bus		20	50	32 flex cables, includes 4 spares	8	6	4	15	2	0.47	73.5
flex cables, sensor to bus		20	160	672 flex cables, $200 each, 20% spares	8	6	4	15	2	0.47	235.2
fibercables, bus to enclosure		20	50	32 -12channel units	8	6	4	15	2	0.47	73.5
Misc cables, etc			150	enclosure to racks, fibers, etc	4	8	4	4	1	0.2	180
lab equipment			100	probe, test equipment	4	4	4	0	1	0.12	112
Management			100		2	4	2	0	1	0.08	108
total	495	360	3575								4547.32
BNL overhead 18%											
LANL overhead 36%											

Table 8 – Cost estimate for the FVTX endcaps with contingency. The methodology used for contingency is in Appendix A (Section 6).

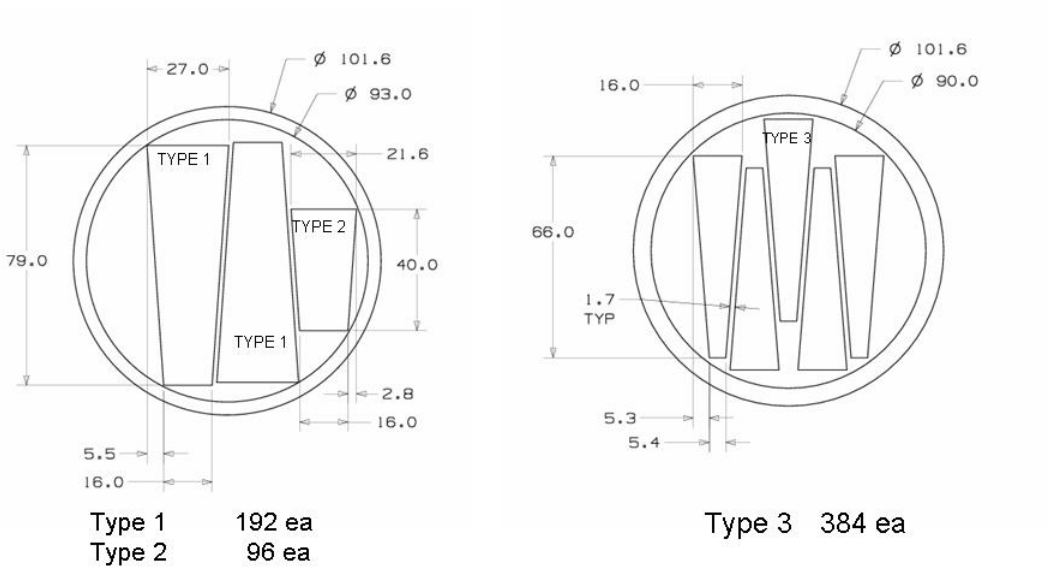

Figure 88 - Silicon wafer layout used for wedge sensor cost estimate.

5.2.2 Project Management and Responsibilities

The LANL Group will work together with HYTEC inc. to develop the design for the Endcap mechanical ladder and cooling. LANL has formed collaboration with FNAL to design, prototype and test the PHX readout chip. An MOU with PHENIX, BNL physics department and FNAL for R&D of the PHX chip was signed in 2004.

The organizational chart for the FVTX project is shown in Figure 89.

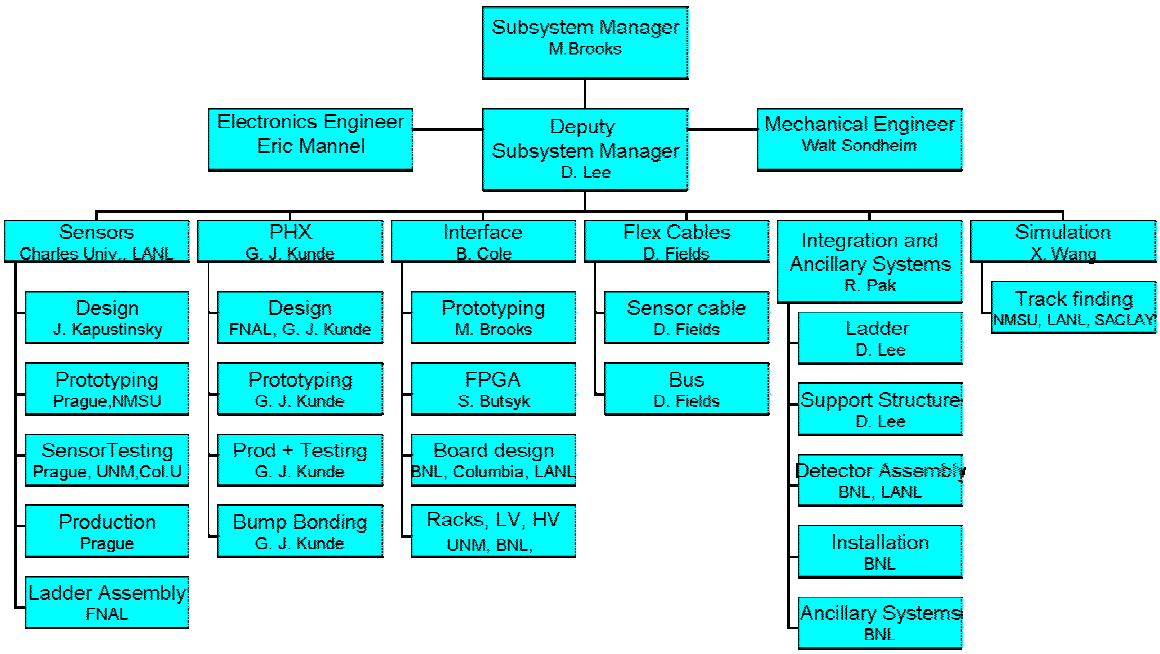

Figure 89 - Organizational Chart for the FVTX project.

Institutional Responsibilities

Los Alamos National Laboratory

LANL coordinate work to procure the silicon sensors, work with FNAL on the development of the PHX chip, with Columbia on development of the interface to PHENIX DAQ, and on the simulation effort with NMSU. Los Alamos is currently leading the mechanical engineering and the integration effort for the barrel detector, and will continue those efforts for the FVTX.

Columbia University

Columbia University is an acknowledged expert on the PHENIX DAQ system. They will work on the interface between the PHX chip and the PHENIX DAQ. The lead electronics engineer also comes from Columbia.

Iowa State University

Iowa State University is currently working on management details with the barrel detector and working on an (funded) SBIR effort addressing the level 1 trigger capabilities of the FVTX. They are also involved with the interface module.

Charles University, Czech Technical University, Institute of Physics, Academy of Sciences, Prague, Czech Republic

Charles University has been active in the development, testing, assembly, and commissioning of the ATLAS pixel sensors. They will do the same for the FVTX effort and additionally participate in software development.

New Mexico State University

NMSU will work on comprehensive simulations for the FVTX effort.

University of New Mexico

UNM has experience in testing, Q/A and a laboratory for characterization of sensors. They are currently working on the barrel strip sensors and will do the same for the FVTX effort.

Ecole Polytechnique, Saclay

Ecole Polytech has contributed to the electronics and software for the muon system has expressed interest in doing the same for the FVTX. Saclay will work on software.

Yonsei University, Seoul, Korea

The Yonsei group has worked on electronics and software for the muon system and will do the same for the FVTX.

6 Appendix A – Contingency Analysis

6.1 Contingency Analysis

The average contingency for the FVTX is 27 %.

This section describes how the contingency for a given WBS element was calculated. Risk is a function of the following factors: the sophistication of the technology, the maturity of the design effort, the accuracy of the cost sources and the impact of delays in the schedule. Risk analysis is performed for each WBS element at the lowest level estimated. Results of this analysis are related to a contingency, which is listed for each WBS element. The goal is to make the method of contingency determination uniform for all project WBS elements.

Definitions

Base Cost Estimate – The estimated cost of doing things correctly the first time. Contingency is not included in the base cost.

Cost Contingency – The amount of money, above and beyond the base cost, that is required to ensure the project's success. This money is used only for omissions and unexpected difficulties that may arise. Contingency funds are held by the Project Manager.

Risk Factors

Technical Risk – Based on the technical content or technology required to complete the element, the technical risk indicates how common the technology is that is required to accomplish the task or fabricate the component. If the technology is so common that the element can be bought "off-the-shelf", i.e., there are several vendors that stock and sell the item, it has very low technical risk, therefore a risk factor of 1 is appropriate. On the opposite end of the scale are elements that extend the current "state-of-the-art" in this technology. These are elements that carry technical risk factors of 10 or 15. Between these are: making modifications to existing designs (risk factor 2-3), creating a new design which does not require state-of-the-art technology (risk factor 4 & 6), and creating a design which requires R&D, and advances the state-of-the-art slightly (risk factor 8 & 10).

Cost Risk – Cost risk is based on the data available at the time of the cost estimate. It is subdivided into 4 categories.

The first category is for elements for which there is a recent price quote from a vendor or a recent catalog price. If the price of the complete element, or the sum of its parts, can be found in a catalog, the appropriate risk factor to be applied is 1. If there is an engineering drawing or specification for the element, and a reliable vendor has recently quoted a price based on these, the cost risk factor to be applied is 2. Similarly, if a vendor has quoted a price based on a sketch that represents the element, and the element's design will not change prior to its fabrication, the appropriate cost risk factor would be 3.

The second category is for elements for which there exists some relevant experience. If the element is similar to something done previously with a known cost, the cost risk factor is 4. If the element is something for which there is no recent experience, but the capability exists, the cost risk is 6. If the element is not necessarily similar to something done before, and is not similar to in-house capabilities, but is something that can be comfortably estimated, the risk factor is 8.

The third category is for elements for which there is information that, when scaled, can give insight into the cost of an element or series of elements. The cost risk factor for this category is 10.

The fourth category is for elements for which there is an educated guess, using the judgment of engineers or physicists. If there is experience of a similar nature, but not necessarily designing, fabricating or installing another device, and the labor type and quantity necessary to perform this function can be estimated comfortably, a cost risk factor of 15 is appropriate.

Schedule Risk – If a delay in the completion of the element could lead to a delay in a critical path or near critical path component, the schedule risk is 8. If a delay in the completion of the element could cause a schedule slip in a subsystem which is not on the critical path, the schedule risk is 4. Only elements where a delay in their completion would not affect the completion of any other item have schedule risks of 2.

Design Risk – is directly related to the maturity of the design effort. When the element design is nearly complete, quantity counts and parts lists finished, the risk associated with design is nearly zero; therefore a risk factor of 0 is applied. This is also the case when the element is an "off-the-shelf" item and the parts counts and quantities are finalized. When the element is still just an idea or concept, with crude sketches the only justification for the cost estimate, the risk associated with design state is high or 15. Between these two extremes are the stages of conceptual design and preliminary design. In conceptual design, when layout drawings of the entire element are approaching completion, some preliminary scoping analyses have been completed, and parts counts are preliminary, the design risk factor is 8. During preliminary design, when there are complete layout drawings, some details worked out, complete parts counts, and some analysis for sizing and showing design feasibility, the appropriate design risk is 4.

Weighting Factors

The weight applied to the risk factors depends on whether there are multiple or single risks involved in completing an element.

The weights applied to technical risk depend upon whether the element requires pushing the current state-of-the-art in design, manufacturing, or both. If the element requires pushing both, the weight to be applied is high, or 4; if either the design or manufacturing are commonplace, the weighting factor is 2.

For weights applied to cost risk, the two factors are material costs and labor costs. If either of these are in doubt, but not both, the weight to be applied to cost risk is 1. If they are both in doubt, the weight applied is 2.

The weight factor given to schedule risk is always 1.

The weight factor given to design risk is always 1 and so is not shown explicitly.

Procedure

The following procedure is used for estimating contingency.

Step 1 – The conceptual state of the element is compared with Table 4 to determine risk factors. A technical risk factor is assigned based on the technology level of the design. A design risk factor is assigned based upon the current state (maturity) of the design. A cost risk factor is assigned based on the estimating methodology used to arrive at a cost estimate for that element. Similarly, a schedule risk factor is identified based on that element's criticality to the overall schedule.

Step 2 – The potential risk within an element is compared with Table 5 to determine the appropriate weighting factors.

Step 3 – The individual risk factors are multiplied by the appropriate weighting factors and then summed to determine the composite contingency percentage.

Step 4 – This calculation is performed for each element at its lowest level.

Step 5 – The dollar amount of contingency for an element is calculated by multiplying the base cost by the composite contingency percentage.

Risk Factor	**Technical**	**Cost**	**Schedule**	**Design**
0	Not used	Not used	Not used	Detail design > 50% done
1	Existing design and off-the-shelf H/W	Off-the-shelf or catalog item	Not used	Not used
2	Minor modifications to an existing design	Vendor quote from established drawings	No schedule impact on any other item	Not used
3	Extensive modifications to an existing design	Vendor quote with some design sketches	Not used	Not used
4	New design; nothing exotic	In-house estimate based on previous similar experience	Delays completion of non-critical subsystem item	Preliminary design >50% done; some analysis done
6	New design; different from established designs or existing technology	In-house estimate for item with minimal experience but related to existing capabilities	Not used	Not used
8	New design; requires some R&D but does not	In-house estimate for item with minimal experience	Delays completion of critical path subsystem item	Conceptual design phase; some drawings; many

	advance the state-of-the-art	and minimal in-house capability		sketches
10	New design of new technology; advances state-of-the-art	Top-down estimate from analogous programs	Not used	Not used
15	New design; well beyond current state-of-the-art	Engineering judgment	Not used	Concept only

Table 9 - Technical, cost and schedule risk factors.

Risk Factor	Condition	Weighting Factor
Technical	Design OR Manufacturing	2
	Design AND Manufacturing	4
Cost	Material Cost OR Labor Rate	1
	Material Cost AND Labor Rate	2
Schedule	Same for all	1
Design	Same for all	1

Table 10 - Technical, cost, schedule and design weighting factors.

7 Appendix B – The FVTX Level-1 Trigger System

7.1 Introduction

In this Appendix we present the current status of a conceptual design for a Level-1 trigger system utilizing the FVTX detector. While many of the details remain to be worked out, the design outlined here is a powerful, flexible trigger system that exploits synergies between many PHENIX upgrades and can address a wide array of physics observables.

We begin by summarizing the additional required event rejection for single and di-muon physics with the PHENIX detector beyond that currently available with the existing Muon Identifier Local Level-1 (MuID LL1). We outline a trigger strategy starting with an FVTX LL1 system for the identification of tracks from both the primary and displaced vertices. This trigger strategy requires combining the FVTX LL1 output with additional information from the PHENIX Muon Trigger Upgrade, which we describe in detail. We then report on the current hardware research and development effort, and conclude with a cost estimate for the FVTX LL1

7.2 Required Event Rejection

The required event rejection for heavy flavor physics with the PHENIX muon arms in future RHIC and RHIC-II running can be divided into two classes of trigger signals – single muons and muon pairs.

The existing trigger option for single muons is to trigger on at least one deep muon road in the Muon Identifier (MuID). A deep road is defined as a track in LL1 that penetrates all layers of the MuID. The achieved rejection factors for the 1-Deep MuID LL1 trigger in both p+p and Au+Au are shown in Table 11 (taken from Table 26 in this proposal). Also shown are the required rejections for the end of RHIC-I running as well as for RHIC-II. The required rejections are what are needed to ensure that the triggers are not prescaled (Table 27 this proposal). Prescaling means that valid triggers are not written to disk because the rate exceeds a bandwidth limit at Level-1 (1kHz). For convenience the required rejections are factorized into the current rejection and the required improvement.

Table 11 - Event rejection required beyond the MuID LL1 for RHIC-I (2008) and RHIC-II running for single muon triggers.

Existing Trigger MuID 1-Deep	Achieved Rejection	Rejection needed 2008	Rejection needed RHIC-II
p+p	478	478*21	478*71
Au+Au	5	5*15	5*116

Table 12 demonstrates that a new Level-1 trigger needs to increase the rejections already at the end of RHIC-I era (2008) and definitely by RHIC-II in order to maximize the collected statistics on open charm and beauty from a given time running the experiment.

The existing trigger option for muon pairs is to trigger on two roads in the MuID LL1. In order to maximize the efficiency for the physics signals of interest, combinations with shallow roads (only utilizing the first three MuID gaps) are used in p+p collisions, where the MuID occupancy is low. The achieved rejection factors for the 1-Deep 1-Shallow trigger in p+p and 2-Deep trigger in Au+Au are shown in the Table 12 (taken from Table 26 in this proposal). Also shown are the required rejections for the end of RHIC-I running as well as for RHIC-II. Again, the required rejections are factorized into the current rejection and the needed improvement.

Table 12 - Event rejection required beyond the MuID LL1 for RHIC-I (2008) and RHIC-II running for di-muon triggers.

Existing Trigger MuID	Achieved Rejection	Rejection needed 2008	Rejection needed RHIC-II
p+p 1-Deep 1-Shallow	23500	< 23500	23500*1.4
Au+Au 2-Deep	15.7	15.7*5	15.7*37

Table 12 demonstrates that a new Level-1 trigger needs to increase the rejections already at the end of Au+Au RHIC-I era (2008) and definitely by RHIC-II in order to get the most statistics in the $B \to J/\psi$ channel from a given time running the experiment. Another way of expressing this is that if no increase in rejection is obtained, then in Au+Au 2008 only one in every 5 produced $B \to J/\psi$ will be recorded, the other events will have to be prescaled away. Note that for p+p running very little to no increase in muon pair trigger rejection is needed.

7.3 FVTX LL1 Trigger Strategy

Based on the physics that the FVTX is designed to address and on the expected collision rates of p+p and A+A collisions at RHIC, there are three main types of triggers that a new Level-1 trigger needs to deliver; displaced single tracks for use in open charm and beauty production, a pair trigger for $B \to J/\psi$ and upsilon production, and an event-trigger to improve the efficiency of min-bias and ultra-peripheral collisions. More details on each are given below. We begin by presenting details of the trigger strategy to be used in the FVTX, followed by a combination with the downstream Muon Trigger.

7.3.1 Single Displaced Tracks

The goal of this trigger is to select events that have a track in the FVTX (comprised of hits in three to four stations) that are displaced from the collision vertex. Large additional sources of displaced tracks are pion and kaon decays, that have a much larger decay lifetime. This leads to a strategy of requiring tracks that are displaced from the collision vertex but are still within several charm/beauty lifetimes to reduce the contamination from pions and kaons. As an example consider a trigger on z-displacement, how far the z-coordinate of the track is from the collision vertex (a similar cut could be placed on the radial distance of closest approach, or DCA)

$$\Delta z_{LOWER} < \Delta z < \Delta z_{UPPER}$$

Since most charm and beauty decays occur close to the collision vertex (exponential decay is largest at t=0), you would like to make Δz_{LOWER} as small as possible while still maintaining an acceptable rejection factor. Since the resolution of pointing back to the collision vertex depends on the momentum, you may be able to afford a tighter Δz_{LOWER} cut at higher momentum in order to catch more of the charm and beauty decays.

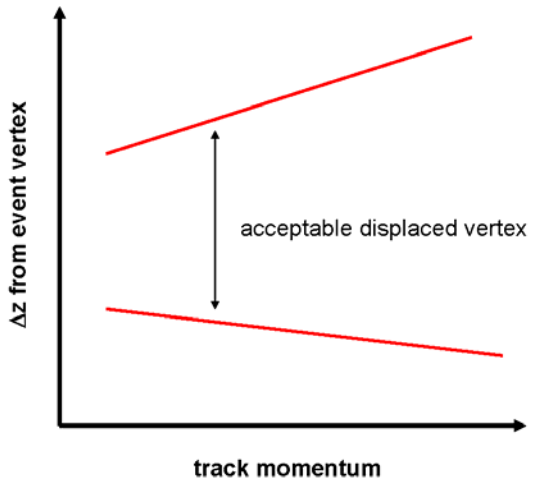

Figure 90 - A schematic representation a displaced vertex cut in the FVTX Level-1 as a function of momentum. The upper limit is designed to reject muons from pion and kaon decays, while the lower cut defines a minimum distance from the event vertex. To avoid potential bias against high momentum decays and still achieve a reasonable rejection factor, it will be necessary to change the upper cut as a function of momentum.

A different reason compels us to also consider that the Δz_{UPPER} cut also needs to be momentum dependent. One would like to make Δz_{UPPER} as small as possible that is consistent with catching several lifetimes of charm/beauty decays ($c\tau \sim$ 300-500 μm). The smaller you can make Δz_{UPPER}, the fewer pion decays you trigger on and the better the trigger rejection. This is shown schematically in Figure 90.

The need to have Δz_{LOWER} and Δz_{UPPER} cuts momentum dependent drives the need for information to be combined from the displaced tracks of the FTVX LL1 and the momentum information from tracks in the downstream Muon Trigger.

7.3.2 Muon Pair Trigger

The requirements for the two main physics cases are exactly complementary: the $B \to J/\psi$ requires a trigger on two tracks that are both displaced, while the upsilon and continuum physics require a trigger on two tracks that come from the main collision vertex.

A potentially powerful pair trigger is to require that both FVTX tracks come from a region that is within a distance a few times the track resolution, or $(\Delta z_1 - \Delta z_2) < n\sigma$, where n=2-3. This trigger will only achieve a sizeable rejection if both FVTX tracks are matched to muon tracks in the downstream Muon Trigger, otherwise the trigger will be satisfied by any pair of primary tracks that do not decay (primary protons, for example). This trigger satisfies all the pair physics goals and should remove many of the random combinations of decaying pions, and therefore it has the potential to reach high rejections.

7.4 Combined Forward Muon Trigger

As emphasized above, much of the physics to be addressed by the FVTX requires the ability to trigger effectively on the presence of a displaced vertex which results in a downstream track in the PHENIX Muon Tracker (MuTr) and Muon Identifier (MuID) detectors. While the FVTX is designed to accurately measure tracks whose origin is displaced from the main event vertex, it cannot identify these tracks as muons nor classify them according to momentum (for large momenta). Because of this, the FVTX LL1 is envisioned to operate as a key part of a combined forward physics trigger that makes use of additional information from the existing PHENIX MuID Local Level-1 and the planned Muon Trigger Upgrade funded by the National Science Foundation.

In the sections that follow we introduce and describe the PHENIX Muon Trigger Upgrade and describe how the FVTX and MuonTrigger systems can be combined to provide a trigger that can address a wide array of physics observables.

7.4.1 The PHENIX Muon Trigger Upgrade

The planned PHENIX Muon Trigger Upgrade is designed primarily to address the needs of the PHENIX spin program in polarized p+p collisions at $\sqrt{s} = 500$ GeV. In order to measure the antiquark contribution to the nucleon spin, it is necessary to trigger on very

high momentum muons originating from the decay of polarized *W* bosons. Low momentum muons from pion and kaon decay, as well as from charm (and to some extent, beauty) decays occur at a substantial rate, so that a trigger is required that can select muons based on momentum as measured in the PHENIX muon arm.

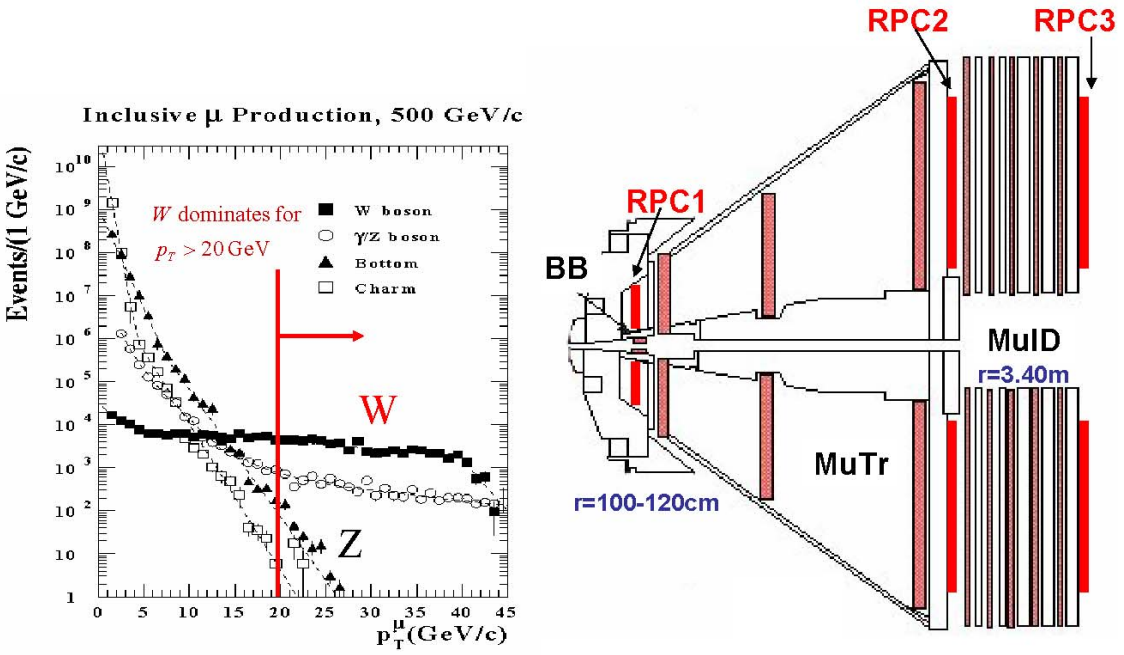

Figure 91 - The PHENIX Muon Trigger Upgrade is designed to provide an effective trigger on muons from the decay of polarized W bosons in polarized p+p collisions at 500GeV. Such muons dominate the inclusive muon production above a momentum of ~20GeV/c. The location of the additional RPC chambers that will be added to the PHENIX muon arm are shown at right.

The Muon Trigger Upgrade will consist of three additional resistive plate chambers (RPC's), two of which will provide tracking in the magnetic field volume and a third that will be used for the rejection of beam-associated backgrounds. These chambers are planned to have a segmentation of 1^o in the phi angle, with 24 segments in theta, although current plans only call for two theta segments at the trigger level. The momentum of the track is measured by the difference in angle between the track hit at the first and second RPC stations. A cut at 2^o corresponds roughly to a cut at a muon momentum of 12 GeV and yields sufficient rejection for the spin program, although the possibility of simultaneously selecting lower-momentum regions (possibly prescaled) will be retained. Finally, track candidates in the RPC chambers will be matched to deep roads in the existing MuID LL1 trigger system. This matching will be done by passing the deep road information along a backplane in the trigger crate to the new Muon RPC (MuPC) Level-1 trigger.

The hardware for the RPC-based Level-1 trigger system will be based on an improved design of the trigger boards used for the MuID LL1. These boards, designated GenLL1 Rev2, are based on a generic design that uses Xilinx FPGA's to implement the trigger algorithm and incorporate up to twenty 1Gbit fiber transceivers as input. We plan to

make use of the generic nature of this design to implement the Combined Trigger Processor (described below) that will combine the output of the FVTX and Muon Level-1 trigger into an extremely flexible and powerful trigger system.

The Muon Trigger Upgrade is funded by a grant from the National Science Foundation, and is planned to be installed and commissioned in PHENIX in 2007-2008, and ready for operation in 2009.

7.5 Combining the FVTX with Downstream Muon Trigger

We envision a trigger strategy where the information from the FVTX is combined and matched with track momentum information from the downstream Muon Trigger. Because the displaced vertex cut needs to be a function of momentum, and the FVTX does not accurately determine the track momentum, it will generate several sets of trigger primitives based on assumed momentum range. Likewise, the Muon Trigger will generate primitives for a selection of candidate momenta. The exact granularity of the trigger primitives in Δz and track momentum will need to be determined by simulation and event rejection requirements.

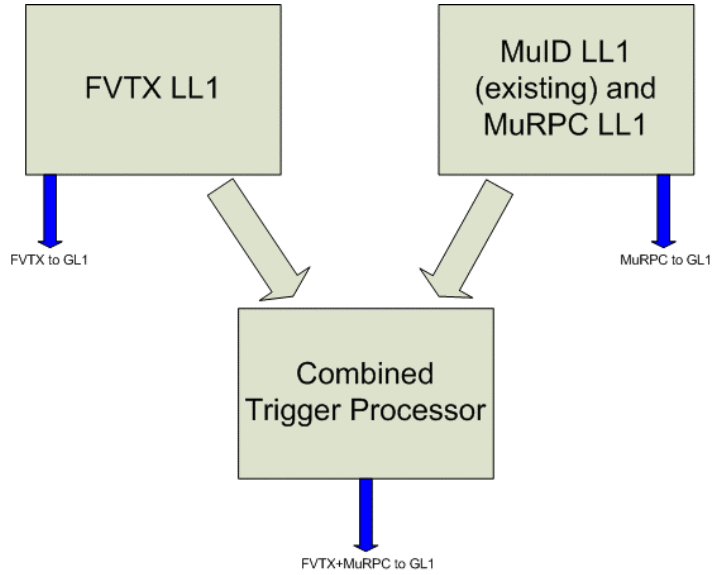

Figure 92 - Block diagram showing the communication between the FVTX and combined MuID and MuRPC triggers with the Combined Trigger Processor. Each LL1 system will have the ability to send trigger data to Global Level-1 (GL1) for independent triggering, or the primitives can be combined in the Combined Trigger Processor (as described in the text) to generate trigger primitives based on information from both systems.

This primitive information will be sent to a combined in a Combined Trigger Processor, as shown in Figure 92. Assuming four FVTX sets of trigger primitives, corresponding to a "low" and "high" momentum assumption (and therefore cut as outlined in Figure 92) combined with a displaced or primary track, and three sets of momentum regions defined by the Muon Trigger as "low", "middle" and "high" we show in Table 13 possible

combinations of trigger primitives for different physics signals. For the sake of being concrete we assume p+p collisions at $\sqrt{s} = 500\text{GeV}$ and therefore the inclusive muon distribution shown in Figure 91. The Muon Trigger momentum selections correspond to regions where charm ("low"), beauty ("middle") or W decay ("high") dominate the inclusive muon spectra.

Physics Signal	FVTX Primitives	Muon Trigger Primitives	Min. No. of Tracks
$D, B \to \mu X$ (single muon, displaced vertex)	displaced vtx ("low" and "high")	"low" and "middle" momentum	1
$B \to J/\psi$ (pair, displaced vertex)	displaced vtx ("low" and "high")	"low" and "middle" momentum	2
$J/\psi, \psi'$ (pair, primary vertex)	primary vertex ("low" and "high")	"low" and "middle" momentum	2
Υ, $\mu\mu$ continuum (pair, primary vertex)	primary vertex ("low" and "high")	"low" and "middle" momentum	2 (same arm, high η) 2 (opposite arm, central)
$W \to \mu\nu$	(not required)	"high" momentum	

Table 13 - Physics signals and potential FVTX and muon trigger primitive combinations that could be used to generate Level-1 triggers.

7.5.1 Hardware Integration of FVTX and Muon Trigger Systems

In previous sections we have outlined a trigger strategy that requires the integration of trigger information from the downstream muon arm with information from the FVTX. We plan to do this by transmitting trigger primitives from both the FVTX LL1 and the Muon Level-1 trigger to a Combined Trigger Processor. We envision that the primitives will consist of mappings of candidates in (θ,φ) space at the back of the FVTX detector with a granularity that is determined by the resolution of the RPC trigger. Each element in the mapping will be a "1" if the system detected a candidate matching a set of requirements in that (θ,φ) element, and a "0" otherwise. There may be several groups of these primitives based on momentum region of interest and vertex origin of the FVTX tracks, as described above.

The combination of the trigger primitive mapping is relatively straightforward in the Combined Trigger Processor, and is essentially an AND operation on the individual map elements. The generation of the trigger data sent to the Global Level-1 trigger will then

consist of a count of the number of elements in each combined primitive map that satisfies the AND operation.

As an example, a trigger on a pair of tracks originating away from the event vertex (for example, the decay $B \rightarrow J/\psi$) would be generated by a trigger primitive map from the FVTX trigger for tracks originating within a window away from the event vertex and a trigger primitive map (or several maps) from the Muon Trigger indicating candidates within selected momentum ranges. If more than two elements in the trigger primitive array survive the AND operation between the FVTX and Muon Trigger, the pair trigger is satisfied.

The exact method by which trigger primitive data is pushed from the FVTX and Muon Trigger LL1 systems into the Combined Trigger Processor will be determined based on the number of maps (and hence the amount of data) that will need to pass between the systems. It is possible that all three systems could coexist in a single crate for each arm, or that individual crates for each system will communicate over fiber or copper links.

We note that some modification of the Muon Trigger design may be necessary to allow an optimal combined trigger. While it is already envisioned that the Muon Trigger will allow lower momentum selections (possible prescaled at GL1) to allow triggering on tracks from charm and beauty decay, it is possible that additional segmentation in theta will be required by the combined trigger, especially in the heavy ion environment. Simulations are underway to determine the required segmentation and the potential impact on the Muon Trigger.

Finally, we note that additional elements could be incorporated into this Combined Trigger Processor approach could be used to incorporate additional PHENIX detectors into the trigger if required by the physics program. For example, the PHENIX Nose Cone Calorimeter is a calorimeter proposed to cover the same rapidity region as the PHENIX muon arms. Such a calorimeter could be included to provide an isolation cut at the trigger level, for example.

7.6 Research and Development on FVTX LL1 Trigger Design

An FY2005 Phase I Small Business Technology Transfer (STTR) award was granted to to Northern Microdesign and ISU. The key personnel in this project are

- Bill Black, President Northern Microdesign previously at Xilinx, Inc. (until September 2003) where he was responsible for the analog portion of the 10Gb/s serial transceivers on the newly introduced Virtex II Pro-X chips
- Nader Badr, Engineer Northern Microdesign with experience in high-speed chip to chip communications and protection circuits
- Gary Sleege, Engineer Iowa State University who has worked on previous PHENIX Level-1 trigger projects, including the MuID LL1
- John Lajoie, Craig Ogilvie at Iowa State University

A Phase II STTR has since been awarded to this group for FY06/07 to continue the Phase-I development and produce a hardware prototype.

During the Phase I project displaced vertex calculations were successfully run on an FPGA using simulated events into one FVTX arm with the simulated event preloaded into memory. The goals of Phase I were to

- Develop a starting algorithm for displaced vertices
- Test if the calculation is feasible for central Au+Au, i.e. to calculate DCAs for all tracks within the maximum PHENIX Level-1 of 4μs.

Single and multiple-track events were simulated using standard PHENIX packages of GEANT for zero magnetic field. This case was chosen as the simplest starting algorithm to set the overall scale for the size and timing of the tracking algorithm. Extension of the Phase-1 algorithms to nonzero magnetic fields is being developed in Phase II.

Within the FPGA we implemented a pipelined four stage algorithm that consisted of (see Figure 93):

1. Hit sorting and preparation
2. Straight-line finding
    a. Hits in station 0 paired with max/min collision point
    b. Searched for hits in station 1 within tolerance
    c. Line between station-0 and station-1 hits
    d. Searched for hits in 2, 3 within tolerance
3. Collision vertex from found lines
4. DCA from collision vertex calculated for each track

The timing for this algorithm was established for single- and multiple-track events then scaled to the full central Au+Au event. The test was done for a single Xilinx XC2VPX70 FPGA, but the scaling for a full central Au+Au event assumes eight XC4VLX200 FPGAs on a board (or equivalent logic in a smaller number of units, such as the Virtex-4). Such a prototype board is the major goal of the Phase-II STTR grant. The timing for the algorithm is shown in Table 14.

Task	Time (ns) Central Au+Au
Hit Format converter	30
Hit Sorter	30
Line-finder	960*
Collision Vertex	70
Secondary Tracks	120
Total	1210

Table 14 - Time budget for the STTR Phase-I FVTX algorithm as described in the text. Notes that the time required for the line finding algorithm could be reduced with added parallelization.

Since the time required to calculate track DCA's is less than the maximum PHENIX Level-1 latency of 4 μs, it seems that an FVTX displaced-vertex trigger is feasible for Au+Au collisions.

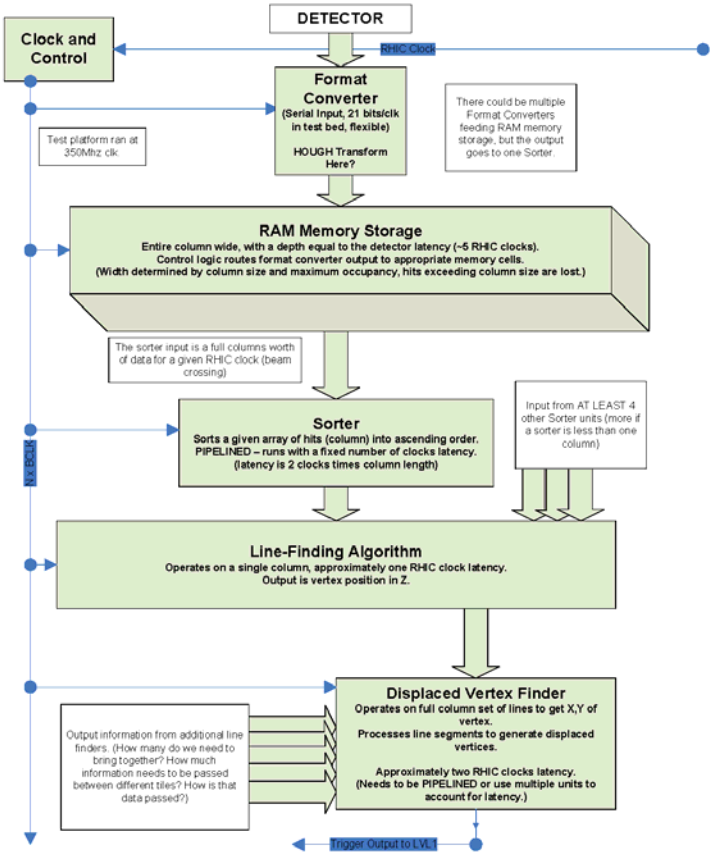

Figure 93 - Block diagram of the FVTX LL1 trigger algorithm, as implemented by Northern Microdesign for STTR Phase-1 feasibility testing.

The major goal of the Phase-II STTR is to produce a prototype board that could be used with the prototype FVTX being installed in PHENIX using LANL's LDRD grant. The result of this development should be a well-developed design for the trigger hardware required for the full FVTX LL1.

7.7 FVTX LL1 Cost Estimate

The full FVTX detector consists of 48 wedges per station, four stations per arm, with 5632 channels per wedge. We plan to develop a Level-1 trigger board that can service eight wedges over four stations, or a total of 5632 x 8 x 4 = 180k channels.

Each wedge will send a single fiber to the trigger board, for a total of 32 fibers per trigger board. For a AuAu event, assuming 1.5% occupancy and 24 bits per hit channel yields 8.3kB per event input to the trigger tile, or 0.259kB per fiber. This can be easily accommodated in a modern 7.5Gbit/s serial link (the Xilinx Virtex-4 FPGA's incorporate transceivers capable of speeds up to 10Gbit/s).

Item Description	Est. Cost
Trigger Tile Boards: **(assumes 12 boards + 3 spares)**	**$510k**
Cost Breakdown per board:	
Board Manufacture	$3k
Assembly	$2k
Interface, Monitoring and Control Logic (Ethernet interface)	$5k
Xilinx Virtex-4 FPGA's (four per board @ $5K per FPGA)	$20k
Fiber Transceivers	$4k
Total Cost Per-Board:	$34k
Combined Trigger Processor: **(assumes 1+1 spare)**	**$25k**
Engineering Design:	**$60K**
Production Board Design	$20k
Systems Integration Support	$20k
Backplane Design	$10K
Combined Trigger Processor FPGA Design	$10K
Crates, Power Supplies and Controllers	**$25k**
Estimated Total System Cost:	**$620k**

Table 15 - Cost estimate breakdown for the FVTX LL1 trigger. The estimate is based on the conceptual design as outlined in the proposal and assumes that the prototype board design is completed as part of the Northern Microdesign Phase-II STTR. The Combined Trigger Processor is assumed to be a GenLL1 Rev2 board, as used in the Muon RPC trigger, so the costs shown are for materials and additional programming.

A breakdown of the estimated cost of a full FVTX LL1 system, consisting of 12 FVTX LL1 trigger boards with two spares and all required infrastructure, is shown in Table 15. This cost estimate assumes the use of Xilinx Virtex-4 FPGA's based on current prices; however, we emphasize that no final technology choice has been made. We also assume that we will be able to use the existing design of the GenLL1 Rev2 boards to implement the Combined Trigger Processor, so that new hardware for this purpose does not need to be developed. The costs listed in Table 1 are based on price quotations for the FPGA's as well as our previous experience in designing trigger hardware.

The cost estimate presented in Table 15 should be viewed as setting that expected scale of the cost of the Level-1 trigger project. Additional refinement will be possible once continued development has refined trigger algorithms that can achieve the required rejections.

Note that the cost listed in Table 15 is not included in the baseline FVTX budget. It is assumed that once the FVTX project is approved we will pursue additional independent funding for this FVTX trigger. We also view the triggering problem as an issue to spans multiple forward PHENIX subsystems that should be addressed in a global way.

8 Appendix C – Estimates for Rates and Triggers for the PHENIX FVTX

8.1 Cross sections, branching ratios and acceptances:

8.1.1 D → mu X

We take the PHENIX result from hep-ex-/0508034,

$$\sigma_{c\bar{c}} = 920 \pm 150 \pm 540 \mu b$$

which gives a single-charm cross section of 1840 μb.

We get the branching ratio to a muon from the PDB and use the average of the charged and neutral D branching ratios (since the number of charged and neutral D's is about equal),

$D^+ \to l + X$ is 17.2%.
$D^0 \to \mu + X$ is 6.6%,

and use 11.9%

For the acceptance we use a Pythia simulation which gives 2.32% (after taking out the branching ratio) for muons with theta 10-35 degrees and a total momentum greater than 2.5 GeV. An additional factor of 0.84 is included on top of the Pythia acceptance to account for octant boundary gaps, etc.

3826/1000000 muons pass the 10-35 degree and p>2.5 GeV cuts, so,
Acc = 3826/1000000/11.9%*84% = 2.32%

Pythia version 6.205 is used with CTEQ5L, M_{charm} = 1.25 GeV and K=1.

To estimate the p_T dependence of the yields we use the p_T shape of the spectra from the above simulations, given as follows as fractional yield in each bin:

All	$0<p_T<1$	$1<p_T<2$	$2<p_T<3$	$3<p_T<4$	$4<p_T<5$
1.00	0.68	0.31	0.012	0.00073	0.000147

8.1.2 B → mu X

We take the $b\bar{b}$ cross section from Ramona Vogt's FONNL calculations as shown in her RHIC-II workshop talk (April 2005),

$$\sigma_{b\bar{b}} = 2\mu b$$

(Her calculations, see below, varied between 1.25 and 2.7 μb for different parameters)

Bottom Cross Sections

m (GeV)	μ_F/m	μ_R/m	σ(all y) (μb)	$\sigma(\lvert y\rvert \le 0.75)$ (μb)	$\sigma(1.2 \le \lvert y\rvert \le 2.2)$ (μb)
$\sqrt{s} = 200$ GeV					
4.5	1	1	2.38	1.100	0.320
4.75	1	1	1.82	0.846	0.242
5	1	1	1.40	0.661	0.185
4.75	0.5	0.5	2.72	1.253	0.365
4.75	0.5	1	1.87	0.864	0.249
4.75	1	0.5	2.67	1.236	0.357
4.75	2	2	1.25	0.589	0.166
4.75	2	1	1.74	0.814	0.231
4.75	1	2	1.33	0.621	0.176
$\sqrt{s} = 500$ GeV					
4.5	1	1	12.26	4.69	1.81
4.75	1	1	9.77	3.78	1.44
5	1	1	7.87	3.08	1.16
4.75	0.5	0.5	13.51	5.19	1.99
4.75	0.5	1	8.98	3.47	1.38
4.75	1	0.5	14.29	5.50	2.11
4.75	2	2	7.40	2.88	1.09
4.75	2	1	10.09	3.91	1.49
4.75	1	2	7.16	2.78	1.05

Table 4: Bottom cross sections obtained from the parameter sets used to determined the theoretical uncertainty band in pp collisions at $\sqrt{s} = 200$ and 500 GeV with the CTEQ6M densities.

Figure 94 - Cross section calculations for beauty with FONNL for various parameters from Ramona Vogt.

Which gives a single-beauty cross section of 4 μb.

For the branching ratio we take 10.87% from the PDB for an admixture of B^+/B^0.

For the acceptance we use 14.5% from a Pythia simulation that requires the muon be within theta 10-35 degrees and with a total momentum above 2.5 GeV. An additional factor of 0.84 is included on top of the Pythia acceptance to account for octant boundary gaps, etc.

1880/100000 muons pass the 10-35 degree and p>2.5 GeV cuts
Acc = 1880/100000/10.87%*84% = 14.5%

All	$0<p_T<1$	$1<p_T<2$	$2<p_T<3$	$3<p_T<4$	$4<pT<5$	$5<p_T<6$
1.00	0.131	0.572	0.234	0.0496	0.0103	0.00258

8.1.3 $B \rightarrow J/\psi X$

We use the 4 μb cross section for B given above.

For the combined branching ratio we use 1.094% ($B \rightarrow J/\psi X$) and 5.9% ($J/\psi \rightarrow \mu\mu$) which gives 0.065%

For the acceptance we use 4.6% from a Pythia simulation that requires both muons to lie within theta 10-35 degrees and have a total momentum above 2.5 GeV. An additional factor of 0.70 for a pair is included on top of the Pythia acceptance to account for octant boundary gaps, etc.

(42/1000000)/(1.094%*5.9%)*0.7 = 4.6%

A Z_{vtx}>1 mm vertex cut is made with an efficiency for $B \rightarrow J/\psi X$ of 39%.

8.2 Luminosities

We use the RHIC-II luminosities from T. Roser as given at,

http://www.phenix.bnl.gov/phenix/WWW/publish/leitch/rhicii-forward/RHIC_II_Luminosity_Roser.xls

Table 16 - Luminosity estimates for RHIC-II from Thomas Roser.

W. Fischer, T. Roser, I. Ben-Zvi, A. Fedotov, BNL
C-AD, 16-Mar-2005

Classical proton radius [m]	1.53E-18

Maximum Luminosity Estimates for RHIC II

Beams	**unit**	**p**	**p**	**unit**	**Si**	**Cu**	**d**	**p**	**Au**	**unit**	**Au**
Charge number Z	…	1	1	…	14	29	1	1	79	…	79
Mass number A	…	1	1	…	28	63	2	1	197	…	197
Relativistic γ	…	108	271	…	108	108	107	108	107	…	107
Revolution frequency	kHz	78.2	78.2	kHz	78.2	78.2	78.2	78	78.2	kHz	78.2
Normalised emittance, 95%, min	mm mrad	12	12	mm mrad	12	12	12	12	12	mm mrad	10
Ions/bunch, initial	10^9	200	200	10^9	10.7	5.2	150	200	1.0	10^9	1.0
Charges per bunch	10^9e	200	200	10^9e	150	150	150	200	80	10^9e	80
No of bunches	…	110	110	…	110	110	110	110	110	…	110
Average beam current/ring	mA	275	275	mA	206	206	206	275	110	mA	110
Luminosity at one IP	**unit**	**p-p**	**p-p**	**unit**	**Si-Si**	**Cu-Cu**	**d-Au**	**p-Au**	**Au-Au**	**unit**	**Au-Au**
Beam-beam parameter per IP	…	0.0123	0.0123	…	0.0046	0.0043	0.0024 0.0036	0.0048 0.0048		…	0.0024

β*	m	1.0	0.5	m	1.0	1.0	2.0	2.0	m	0.5
Peak luminosity	10^{30} $cm^{-2}s^{-1}$	150	750	10^{28} $cm^{-2}s^{-1}$	42	10	28	37	10^{26} $cm^{-2}s^{-1}$	90
Peak / average luminosity	…	1.5	1.5	…	1.3	1.3	1.5	1.5	…	1.3
Average store luminosity	10^{30} $cm^{-2}s^{-1}$	100	500	10^{28} $cm^{-2}s^{-1}$	32	8	19	25	10^{26} $cm^{-2}s^{-1}$	70
Time in store	%	55	55	%	55	55	55	55	%	60
Luminosity/week	pb^{-1}	33	166	nb^{-1}	108	25	62	83	nb^{-1}	2.5
Luminosity/week, achieved	pb^{-1}	0.9		nb^{-1}		2.4	4.5		nb^{-1}	0.16

and to get an estimate of RHIC-I luminosities we scaled these down according the ratios for average store luminosity given also by T. Roser in a RHIC-II talk,

pp: $1.5x10^{32} / 5x10^{32} = 0.3$
AuAu: $8x10^{26} / 70x10^{26} = 0.114$

For dAu we take the RHIC-I luminosity from the PHENIX Run6 BUP for dAu in Run7 of 2.8 nb^{-1}/wk.

These luminosities per week are:

Table 17 - Summary of luminosities used in these rate calculations for RHIC-II and RHIC-I (2008).

collision	RHIC-II	RHIC-I (2008)
Pp	33 pb^{-1}/wk	9.9 pb^{-1}/wk
dAu	62 nb^{-1}/wk	2.8 nb^{-1}/wk
AuAu	2.5 nb^{-1}/wk	0.327 nb^{-1}/wk

8.3 Reality factors

We use the following reality factors for pp:

- 55% for |Zvtx| < 10 cm
- 60% PHENIX duty factor
- 79% for the min-bias part of the pp trigger
- 90% trigger efficiency
- 90% reconstruction efficiency

For AuAu we use the same factors except:

- 90% for min-bias part of the AuAu trigger
- 70% reconstruction efficiency

8.4 Summary of Changes from old numbers

Changes from older estimates include:

- Explicit calculation of the B → μ X acceptance which is much larger than the D → μ X given the higher momentum muons from the B.
- Use FONNL calculations of the B cross section.
- Use the PHENIX measured D cross section.
- Update the branching ratios from the latest online Particle Data Book (PDB).
- Adding various efficiency and reality factors.
- Using Roser luminosities
- Lowering the single-muon momentum threshold to 2.6 GeV from 2.5 GeV.

Table 18 - Comparison of new and old values for various parameters used in these rate calculations.

	D → μ X		B → μ X		B → J/ψ X → μ μ X	
	new	old	New	old	New	old
σ(pair)	920 μb	325 μb	2 μb	0.73 μb	2 μb	0.73 μb
BR	11.9%	9.6%	10.87%	10.49%	1.094% • 5.9%	1.2% • 5.9%
Acc(1-arm)	2.32%	4.7%	14.5%	2.08%	4.6%	2.83%
eff	84%	1	84%	1	70%	1
p_T> (Gev)	2.5	2.6	2.5	2.6	2.5	2.6
eff_{vtx}	1	n/c	1	n/c	39%	n/c

8.5 Rates

Table 19 - Estimated rates per week for p+p collisions.

pp	ccbar								
	sigma	1-arm		Lumi	Lumi		with	eff	with
process	(ub)	Acc	BR	Type	(pb-1)	counts	reality	dzvtx	dzvtx
D → μ	920	0.0232	0.119	RHIC-II	33	3.4E+08	7.1E+07	1	7.1E+07
	920	0.0232	0.119	2008	9.9	1.0E+08	2.1E+07	1	2.1E+07
B → μ	2	0.145	0.1087	RHIC-II	33	4.2E+06	8.8E+05	1	8.8E+05
	2	0.145	0.1087	2008	9.9	1.2E+06	2.6E+05	1	2.6E+05
B → J/ψ	2	0.046	0.00065	RHIC-II	33	7.9E+03	1.7E+03	0.39	6.5E+02
	2	0.046	0.00065	2008	9.9	2.4E+03	5.0E+02	0.39	2.0E+02

Table 20 – p+p rates vs p_T for same estimates as in Table 19.

pp	0<pT<1	1<pT<2	2<pT<3	3<pT<4	4<pT<5	6<pT<6
D -> mu	4.8E+07	2.2E+07	8.5E+05	5.2E+04	1.0E+04	---
	1.4E+07	6.6E+06	2.5E+05	1.6E+04	3.1E+03	---
B -> mu	1.2E+05	5.0E+05	2.1E+05	4.4E+04	9.1E+03	2.3E+03
	3.5E+04	1.5E+05	6.2E+04	1.3E+04	2.7E+03	6.8E+02

Table 21 - Estimated rates per week for d+Au collisions.

dAu	ccbar								
	Sigma	1-arm		Lumi	Lumi		with	eff	with
process	(ub)	Acc	BR	type	(nb-1)	counts	reality	dzvtx	dzvtx
D → μ	920	0.0232	0.119	RHIC-II	62	2.5E+08	6.0E+07	1	6.0E+07
	920	0.0232	0.119	2008	2.8	1.1E+07	2.7E+06	1	2.7E+06
B→ μ	2	0.145	0.1087	RHIC-II	62	3.1E+06	7.4E+05	1	7.4E+05
	2	0.145	0.1087	2008	2.8	1.4E+05	3.3E+04	1	3.3E+04
B → J/ψ	2	0.046	0.0007	RHIC-II	62	5.8E+03	1.4E+03	0.39	5.5E+02
	2	0.046	0.0007	2008	2.8	2.6E+02	6.3E+01	0.39	2.5E+01

Table 22 – d+Au rates vs p_T for same estimates as in Table 21.

dAu	0<pT<1	1<pT<2	2<pT<3	3<pT<4	4<pT<5	6<pT<6
D → μ	4.1E+07	1.9E+07	7.2E+05	4.4E+04	8.8E+03	
	1.8E+06	8.4E+05	3.2E+04	2.0E+03	4.0E+02	
B → μ	9.7E+04	4.2E+05	1.7E+05	3.7E+04	7.6E+03	1.9E+03
	4.4E+03	1.9E+04	7.8E+03	1.7E+03	3.4E+02	8.6E+01

Table 23 - Estimated rates per week for Au+Au collisions.

AuAu	ccbar								
	Sigma	1-arm		Lumi	Lumi		with	eff	with
process	(ub)	Acc	BR	Type	(nb-1)	counts	reality	dzvtx	dzvtx
D → μ	920	0.0232	0.119	RHIC-II	2.5	9.9E+08	1.8E+08	1	1.8E+08
	920	0.0232	0.119	2008	0.327	1.3E+08	2.4E+07	1	2.4E+07
B → μ	2	0.145	0.1087	RHIC-II	2.5	1.2E+07	2.3E+06	1	2.3E+06
	2	0.145	0.1087	2008	0.327	1.6E+06	3.0E+05	1	3.0E+05
B → J/ψ	2	0.046	0.00065	RHIC-II	2.5	2.3E+04	4.3E+03	0.39	1.7E+03
	2	0.046	0.00065	2008	0.327	3.0E+03	5.7E+02	0.39	2.2E+02

Table 24 –Au+Au rates vs p_T for same estimates as in Table 23.

AuAu	0<pT<1	1<pT<2	2<pT<3	3<pT<4	4<pT<5	6<pT<6
D → μ	2.2E+07	1.0E+07	3.9E+05	2.4E+04	4.8E+03	
	1.6E+07	7.5E+06	2.9E+05	1.8E+04	3.5E+03	
B → μ	3.0E+05	1.3E+06	5.4E+05	1.1E+05	2.4E+04	5.9E+03
	3.9E+04	1.7E+05	7.0E+04	1.5E+04	3.1E+03	7.7E+02

8.6 Rates for prompt vector mesons: J/ψ, ψ' and ϒ

Although the rates for the prompt vector mesons, J/ψ, ψ' and ϒ, have been estimated elsewhere (e.g. in Tony Frawley's RHIC-II studies[lii]); we give estimates here that are consistent with the single heavy-quark rates estimates above. The following inputs are used and the rates for one RHIC-II week are shown in Table 25.

- For the cross sections we use the recently published J/ψ cross section of 2.61 μb from PHENIX[xxvii]. For the ψ' we use the cross section ratio of 14% to the J/ψ from Ref. liii; and for the ϒ we use the preliminary estimate from PHENIX at QM05 of 2.1 nb.
- We take the Branching ratios from the particle data book as 5.9% (J/ψ), 0.76% (ψ') and 2.1% (ϒ); where the latter is an average over the three Upsilon states as calculated in PHENIX Analysis Note AN401.
- For the acceptance we use values from recent PHENIX analysis: 1.08% (J/ψ) and 1.19% (ϒ). And we assume the ψ' acceptance is the same as that for the J/ψ.

Table 25 - Counts for prompt vector mesons per week into both muon arms at RHIC-II luminosity.

Signal	Luminosity/week	J/ψ → μμ	ψ'→ μμ	ϒ → μμ
Au+Au	2.5 nb^{-1}	60k	1.1k	200
d+Au	62 nb^{-1}	20k	360	65
p+p	33 nb^{-1}	23k	420	77

Although not shown in the table, the rates for ϒ's at y=0 from detecting their decay into one muon in each of the two muon arms is approximately equal to the rate into one muon arm shown in Table 25.

8.7 Trigger considerations

8.7.1 Rejection factors

For pp triggers we use Lajoie's estimate from run5 data and simulations oof 478 (1-deep), 23500 (1-deep & 1-shallow) and 133500 (2-deep). An independent check of these numbers was done by looking at the run5 pp triggers for several runs (179809, 170190, 174696, 177185) where one sees about a factor of 500 rejection for 1-deep muons (south arm) and 10^4 rejection for 1d1s dimuons (south arm).

For AuAu we use simulations of the level-1 run on 2004 AuAu raw data files (since the level-1 hardware was not working fully during that run yet). Lajoie gets rejection factors of 5 for 1-deep and 1-deep * 1-shallow triggers and 15.7 for 2-deep triggers.

As shown in Table 26, we will then use the averages over the two arms, with the North arm generally being somewhat worse than the South due to its coverage at smaller angles with its smaller piston.

Table 26 - Level-1 muon trigger rejection factors for pp and AuAu based on previous data and simulations of the level -1 triggers.

Species	Arm	Source	Trigger	Reject. factor
pp	N	Run5	1-deep	580
		"	1-deep & 1-shallow	28700
		"	2-deep	20000
	S	"	1-deep	376
		"	1-deep & 1-shallow	18300
		"	2-deep	67000
	N&S avg	"	1-deep	478
		"	1-deep & 1-shallow	23500
		"	2-deep	133500
AuAu	N	Sim on run4 prdf	1-deep	5.1
		"	1-deep & 1-shallow	5.3
		"	2-deep	15.3
	S	"	1-deep	4.8
		"	1-deep & 1-shallow	5.3
		"	2-deep	16.1
	N&S avg	"	1-deep	5
		"	1-deep & 1-shallow	5
		"	2-deep	15.7

8.7.2 Trigger rates and needed rejection factors

For these estimates we will use a 2-deep (2d) dimuon trigger in AuAu and a 1-deep & 1-shallow (1d1s) trigger in pp.

We use the luminosities quoted above in the discussion of FVTX rates. To calculate the peak luminosity from the average, we will follow Tony's example again and use a factor of 4.48 from the average instantaneous luminosity.

Min-bias rates are calculated from luminosities using the full inelastic cross sections for pp and AuAu of 42 mb and 6847 mb respectively. This assumes that the FVTX itself can provide a min-bias trigger that is very close to 100% of the inelastic cross section. In any case this is an upper limit on the min-bias trigger rate.

We use event sizes of 180 kb and 250 kb for pp and AuAu respectively. These sizes will need to be updated as the additional contributions from the various PHENIX upgrades become clear.

Additional trigger rejections needed from the FVTX (or from combination with other upgrades such as the muon RPC trigger upgrade) will be calculated assuming a 60 Mb/s limit for each muon trigger, which corresponds to 10% of an assumed DAQ limit of 600 Mb/s. I.e. if one uses ½ of the 600 Mb/s for min-bias, and the remaining 300 Mb/s is split between 5 types of triggers, then that leaves 60 Mb/s per trigger (sum over the two arms).

Table 27 – Estimated trigger rates and addition rejection factors needed for p+p and Au+Au collisions in PHENIX.

					MB	evt	1d		1d	1d1s		1d1s
		L/wk	Zvtx	*L* pk	pk rate	size	pk rate	1d	presc.	pk	1d1s	presc.
	era	(pb-1)	<10cm	10^32	Mhz	(kb)	(khz)	Mb/s	needed	(hz)	Mb/s	needed
pp	RHICII	33	0.55	1.34	5.65	180	23.63	4253	71	481	87	1.4
	2008	9.9	0.55	0.40	1.69	180	7.09	1267	21	144	26	0.4
					MB	evt	1d		1d	2d		2d
		L/wk	Zvtx	*L* pk	pk rate	size	pk rate	1d	Presc.	pk rate	2d	presc.
	era	(nb-1)	<10cm	10^26	khz	(kb)	(khz)	Mb/s	needed	(hz)	Mb/s	needed
AuAu	RHICII	2.5	0.55	101.85	69.74	250	27.9	6974	116	8884	2221	37
	2008	0.327	0.55	13.32	9.12	250	3.65	912	15	1162	291	4.8

9 Appendix D – Synergy with other PHENIX upgrades

Although the FVTX detector adds a lot of important physics, as has been discussed at length in the body of the proposal, it also can work together with many of the ongoing or other proposed upgrades to strengthen or add physics capability beyond what any subsystem of PHENIX brings by itself. Here we will discuss briefly some of these strengthened or added capabilities. Since integration with the muon tracker and muon identifier has already been extensively discussed, we will not repeat that discussion here.

9.1 Central Barrel Vertex Detector (VTX) Upgrade

The most obvious coupling of the upgrades is with the VTX detector, which provides similar vertexing capability in the central rapidity region to what this FVTX detector provides. When used together they can provide a very accurate primary vertex which can then be used by both detectors as a origination point for determining detached vertices for the various processes already discussed in this proposal. As shown in Section 3.2, the FVTX can do this quite well by itself even in p+p collisions and can do it at the level-1 trigger level for fast triggers; but the VTX can improve this further. Unfortunately the VTX does not give a fast output and cannot contribute at the fast trigger level.

Together the two detectors, as has been discussed in the body of this proposal, give a quite large range in rapidity, -2.2 to +2.2. However at the boundary between them, some tracks will give hits in both detectors. This should help with internal alignment between the two vertex detectors and will also help make a smooth picture of the physics across the boundary between the VTX and FVTX parts of the vertex detector.

9.2 Muon Trigger Upgrade

The Muon Trigger Upgrade is a NSF funded upgrade with the main goal being to allow selective triggering on very high momentum (> 10 GeV) muons from W decays for measurements of the flavor dependence of spin structure functions. Three Resistive Plate Cathode strip (RPC) detector planes will be added to each muon arm with one in just in front of station-1, one in between station-3 and the front of the muon identifier, and a third plane behind the muon identifier. The RPC's will have 1^0 segmentation in ϕ (the bend direction in the muon magnet's field) and up to 24 segments in the radial direction.

http://www.npl.uiuc.edu/phenix/publish/nsf/muon-mri.pdf

The coarse momentum resolution of the MuTrig can provide a momentum measurement (fast enough to be used for a level-1 trigger) that would help to:

- Allow momentum dependence vertex cuts in the FVTX or prescaling of lower momentum ranges.

- Help eliminate any tracks that do not point to the primary vertex and do not satisfy time-of-flight cuts for tracks originating from the primary vertex.
- Allow track matching at the fast trigger level between roads through the MuTrig RPC's and the muon identifier with the FVTX tracks.
- Help eliminate soft pion tracks in the FVTX that do not match tracks above.
- And also provide a space (x-y) point to help the muon tracker pattern recognition in high occupancy events (central Au+Au collisions) that will reduce incorrect tracks in the muon tracker. This will also benefit the FVTX by providing cleaner muon tracks to match with.
- Is TOF in MuTrig good enough to help with muon vs punch-through – I don't think so??

9.3 Nose Cone Calorimeter (NCC) Upgrade

The NCC upgrade would turn the present copper nosecone absorbers, that lie in front of the muon magnets and behind where the FVTX would go, into an active Silicon-tungsten electromagnetic and partial hadronic calorimeter for detecting various particles including photons and neutral pions. This would extend much of the capability of the PHENIX central arms calorimeters into the forward and backward regions now covered only for muons. Highlights of the physics this upgrade could add include direct photons, extending the study of pion suppression to these rapidities and measurements of the χ_C by its decay into a photon and a photon. The proposal for this upgrade, along with out FVTX proposal, is now being prepared for submission to DOE for funding, although contributions from RIKEN may also help fund the total $7M cost of two NCC endcaps.

https://www.phenix.bnl.gov/WWW/publish/seto/NCC/ncccdr.pdf

A number of physics issues could be addressed with the combination of the NCC and the FVTX, these include:

- Identification of hadron jets in the NCC to help reduce backgrounds for single muons from punch-through hadrons that penetrate deep into the muon identifier and otherwise look like muons. Although the FVTX in combination with the muon tracker can eliminate many of these, the possibility of reducing punch-throughs further could be quite valuable. A detailed study of shower probabilities and characteristics in the 1.5 lamba NCC needs to be made in order to make a quantified estimate of the level to which the NCC can help here.
- Can aid in the study of associated particle production with hard processes such as J/ψ production, especially by adding detection capability for neutral particles such as π^0's and photons. These associated particles, may help understand the production mechanism for J/ψ and could also give information on the interaction with co-moving light quarks in heavy-ion collisions.
- The combination of the FVTX and NCC in the forward and backward rapidity regions would allow detection of charm and beauty decays via their decay to electrons with the electron identification coming from the NCC and the detached vertex from the FVTX. This would give a second measurement of these heavy

quarks, in addition to that with single muons; and might even allow extending these measurements to lower momentum with the electrons compared to the ~2.5 GeV momentum threshold for detection via detached vertices with muons.

- The additional measurements in the NCC might also help in overall definition of the muon track in combination with the FVTX mini-strip hits, muon tracker cathode-strip hits, muon identifier hits and MuTrig RPC hits. (if one NCC plane has smaller pixels, it would help most – need to check NCC proposal about this) It may also be able to help identify kinks in tracks that result from decay-in-flight of hadrons to muons, and thereby reduce the contributions of these decays-in-flight to the final single muon spectra.
- This matching between FVTX and NCC might also help with low energy tracks in the forward direction, by looking for consistency between the multiple scattering of the track in the FVTX and the energy observed for the matching track in the NCC.
- Electrons and muons, both with detached vertices, could be combined into $D\overline{D} \to \mu e$ pairs which would provide a additional way to study the di-lepton continuum under and near the J/ψ peak. Identification of these lepton pairs would also help in isolating the Drell-Yan di-leptons which are otherwise over-whelmed by copious random pairs from heavy quark decays. This could include back-to-back μe pairs where an electron is seen in one endcap and a muon in the other.
- The FVTX can act as a charged particle veto for the NCC, to help solidify the identification of neutral particles, e.g. photons and π^0's.

9.4 Muon Piston Calorimeter (MPC)

The Muon Piston Calorimeter (MPC) is a small electromagnetic calorimeter composed of an array of $PbWO^4$ crystals (240/arm) with photo-diode readout that would be installed inside the muon magnet piston of each muon arm, and would add detection jets in the 3 to 4 rapidity range, providing measurements of jets, pions and eta's for the study of spin asymmetries in the very forward region in p+p collisions and to search for effects of shadowing or the color glass condensate in that region in d+A collisions. The South MPC is presently being installed and should be in operation for the 2006 RHIC run. Like the NCC, it may be useful in sampling particles near those in the FVTX, e.g. in terms of associated particle production for instance. But it has no tracking, only calorimetry – so would likely not be useful in Au+Au collisions.

---

[i] http://p25ext.lanl.gov/phenix/fvtx/
[ii] X-N Wang, M. Gyulassy, Phys. Rev. Lett. **68**, 1480 (1992).
[iii] M. Gyulassy, P. Levai, I. Vitev, Phys. Rev. Lett. **85**, 5535 (2000).
[iv] I. Vitev, Phys. Lett. B **562**, 36 (2003).
[v] PHENIX Collaboration, Nucl. Phys. A 757, 184 (2005).
[vi] Y. Akiba (for the PHENIX collaboration), Focus talk at Quark Matter 2005, nucl-ex/0510008.
[vii] S. Butsyk (PHENIX collaboration), nucl-ex/0510010 and S.S. Adler et al., (PHENIX collaboration) Phys. Rev. C 72, 024901 (2005).

[viii] F. Laue et al. (STAR collaboration), nucl-ex/0411007.
[ix] X. Dong, Quark Matter 2005 talk, nucl-ex/0509038.
[x] Yuri L. Dokshitzer, D.E. Kharzeev Phys. Lett.**B519**:199-206,2001
[xi] M. Djordjevic, M. Gyulassy nucl-th/0305062
[xii] M. Djordjevic, M. Gyulassy, Phys. Lett. **B560**, 37 (2003)
[xiii] B. H. Zhang, E. Wang, X-N. Wang, nucl-th/0309040
[xiv] S. Batsouli, *et al*, Phys. Lett. **B557**, 26 (2003)
[xv] I. Vitev, private communication (heavy-quark fragmentation in the medium).
[xvi] E. Shuryak Phys. Rep **61**, 71 (1980)
[xvii] P. Levai *et al*, Phys. Rev C **51**, 3326 (1995)
[xviii] Z. Lin and M. Gyulassy, Phys. Rev. C **51**, 2177 (1995)
[xix] R. Vogt, FONLL NLO calculation of charm cross section vs rapidity, RHIC-II presentation - http://rhicii-science.bnl.gov/heavy/doc/April05Meeting/ramona-nlo.pdf
[xx] M. Arnedo, Phys. Rep. **240**, 301 (1994), K.J. Eskola et al., hep-ph/9906484.
[xxi] L. McLerran and R. Venugopalan, Phys. Rev. D **49**, 2233 (1994); A.H. Mueller and J.W. Qui, Nucl. Phys. B **268** 427 (1986) and L.V. Bribox, E.M. Levin and M.G. Ryskin, Phys. Rept. **100**, 1 (1983).
[xxii] K.J. Eskola, V.J. Kolhinen, R. Vogt, Nucl. Phys. **A696**, 729 (2001) & hep-ph/0104124.
[xxiii] L. Frankfurt, M. Strikman, Eur. Phys. J **A5**, 293 (99)
[xxiv] B.Z. Kopeliovich, A.V. Tarasov, J. Huefner, Nucl. Phys. **A696**, 669 (2001) or hep-ph/0104256.
[xxv] J.-W. Qui, I. Vitev, Phys. Lett. B632, 507 (2006).
[xxvi] B. Kopeliovich *et al.,*, Phys. Rev. C72, 054606 (2005) & hep-ph-/0501260 (2005).
[xxvii] S. Adcox *et al.* (PHENIX collaboration), Phys. Rev. Lett. **96**, 012304 (2006) & nucl-ex/0507032.
[xxviii] R. Vogt, Phys. Rev. C **61**, 035203 (2000).
[xxix] M.J. Leitch et al., (E866/NuSea), Phys. Rev. Lett. **84**, 3256 (2000).
[xxx] J. Badier *et al.*, (NA3), Z. Phys. **C20**, 101 (1983).
[xxxi] M.C. Abreu *et al* (NA50), Phys. Lett. **B410**, 327 (1997).
[xxxii] B.Z. Kopeliovich, A.V. Tarasov, Nucl. Phys. **A710**, 180 (2002) or hep-ph/0205151 and J. Raufeisen private communication.
[xxxiii] C.Lourenco, "Workshop on Quarkonium Production in Relativistic Nuclear Collisions", Seattle, 11 May 1998, B $\rightarrow$ J/Psi estimates, private communication.
[xxxiv] D. Kharzeev, Nucl. Phys. **A702**, 39 (2002) or hep-ph/0111386.
[xxxv] Talk given by Xiaorong Wang at Hawaii Division of Nuclear Physics meeting, September 18 2005.
[xxxvi] T. Goldman, M.B. Johnson, I. Vitev, J.W. Qui, to be published.
[xxxvii] V. Guzey, M. Strikman and W. Vogelsang, Phys. Lett. **B603**, 173 (2004).
[xxxviii] I. Arsene *et al*., Phys. Rev. Lett. **93**, 242303 (2004).
[xxxix] T. Gehrmann and W. J. Stirling, Z. Phys. C65, 461 (1995).
[xl] C. Aidala *et al*., Research Plan for Spin Physics at RHIC.
[xli] G.L. Kane, J. Pumplin, and W. Repko, Phys. Rev. Lett. **41** (1978) 1689.
[xlii] D.W. Sivers, Phys. Rev. D41 (1990) 83; Phys. Rev. D**43** (1991) 261.
[xliii] J.C. Collins, S.F. Heppelmann, G.A. Ladinsky, Nucl. Phys. **B420** (1994) 565.
[xliv] S.J. Brodsky, D.S. Hwang and I. Schmidt, Phys. Lett. **B530** (2002) 99.
[xlv] M. Burkardt, Phys. Rev. D**69** (2004) 091501.
[xlvi] M. Anselmino et al., Phys. Rev. D**70** (074025) 2004.
[xlvii] E. Norrbin, T. Sjostrand, Eur. Phys. J. C **17**, 137 (2000)
[xlviii] G.C. Nayak, J. Smith, Phys. Rev. D **73**, 014007 (2006) or hep-ph/0509335.
[xlix] S.S. Adler, (PHENIX collaboration) hep-ex/0508034, submitted to Phys. Rev. Lett.
[l] D.M. Jansen, *et al.* (E789) Phys. Rev. Lett. **74**, 3118 (1995).
[li] W. Xie *et al.* (PHENIX), Quark Matter 2005, nucl-ex/0510020.
[lii] http://www.phenix.bnl.gov/WWW/publish/abhay/panic05/frawley.pdf
[liii] R. Gavai, *et al.*, Int. J. Mod. Phys. A**10**, 3043 (1995) & hep-ph/9502270.